

DEVELOPMENT OF A NANOGAP FABRICATION METHOD FOR
APPLICATIONS IN NANOELECTROMECHANICAL SYSTEMS AND
NANOELECTRONICS

by

ANIL GÜNAY DEMİRKOL

Submitted to the Graduate School of Engineering and Natural Sciences

in partial fulfillment of

the requirements for the degree of

Doctor of Philosophy

Sabancı University

January 2013

DEVELOPMENT OF A NANOGAP FABRICATION METHOD FOR
APPLICATIONS IN NANOELECTROMECHANICAL SYSTEMS AND
NANOELECTRONICS

APPROVED BY:

Assoc. Prof. Dr. İsmet İ. Kaya
(Dissertation Supervisor)



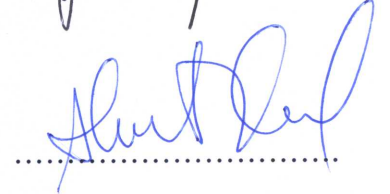
Assoc. Prof. Dr. Zafer Gedik



Assoc. Prof. Dr. Ayhan Bozkurt



Prof. Dr. Ahmet Oral



Assoc. Prof. Dr. Kaan Güven



DATE OF APPROVAL:28.01.2013.....

© Anıl Günay Demirkol 2013
All Rights Reserved

DEVELOPMENT OF A NANOGAP FABRICATION METHOD FOR
APPLICATIONS IN NANOELECTROMECHANICAL SYSTEMS AND
NANOELECTRONICS

Anıl Günay Demirkol

Physics, PhD Thesis, 2013

Thesis Supervisor: Assoc. Prof. Dr. İsmet İ. Kaya

Keywords: Nanogap, Vacuum Tunnel Junction, Controlled Thermal Evaporation, High
Tensile Stress Thin Films, NEMS

ABSTRACT

There is a great need for a well-controlled nanogap fabrication technique compatible with NEMS applications. Theoretically, a displacement sensor based on vacuum tunnel junction or a nanogap can be capable of performing quantum-limited measurements in NEMS applications. Additionally, in the context of nanoelectronics, nanogaps are widely demanded to characterize nanostructures and to incorporate them into nanoscale electronic devices. Here, we have proposed and implemented a fabrication technique based on the controlled shrinkage of a lithographically defined gap between two suspended structures by thermal evaporation. We have consistently produced rigid and stable metallic vacuum tunneling junctions at nanometer or sub-nanometer sizes. The fabricated nanogaps were characterized by I-V measurements and their gap sizes and potential barrier heights were interrogated using the Simmons' model. Throughout this work, high tensile stress silicon nitride thin films were preferred for the fabrication of suspended structures because they have high resonance frequencies with low dissipation, they are mechanically stable, and they are resilient to stiction problem. However, high-stress nitride structures experience a complex shape deformation once they are suspended. The shape deformation is undesired when the precise positioning of the structures is required as in nanogap fabrication. We developed a new method in which the built in stress gradient is utilized to tune the distance between two suspended structures. The technique was simulated by finite element analysis and experimentally implemented to demonstrate a gap tuning capability beyond the lithographic resolution limits.

NANOELEKTROMEKANİK SİSTEMLER VE NANOELEKTRONİK
UYGULAMALARINA YÖNELİK BİR NANOARALIK ÜRETİM YÖNTEMİNİN
GELİŞTİRİLMESİ

Anıl Günay Demirkol

Fizik, Doktora Tezi, 2013

Tez Danışmanı: Doç. Dr. İsmet İ. Kaya

Anahtar Kelimeler: Nanoaralık, Vakum Tünelleme Ekleme, Kontrollü Isıl

Buharlaştırma, Yüksek Çekme Gerilimli İnce Filmler, NEMS

ÖZET

NEMS uygulamaları ile uyumlu, kontrollü bir nanoaralık üretim yönteminin geliştirilmesine büyük ihtiyaç duyulmaktadır. NEMS alanında yapılan teorik çalışmalar, vakum tünelleme eklemi ya da nanoaralık kullanımına dayalı bir yer değiştirme sensörünün, kuantum sınırında ölçümler yapabileceğini göstermektedir. Ayrıca nanoelektronik uygulamalarında, nanoyapıları karakterize etmek ve bu yapıları nano boyutta aygıtlara yerleştirmek için nanoaralıklara gereksinim duyulmaktadır. Bu çalışmada, askıda duran yapılar arasında litografik olarak belirlenmiş bir aralığın ısıl buharlaştırma ile kontrollü olarak daraltılmasına dayalı bir yöntem önerilmiş ve uygulanmıştır. Nanometre ya da nanometre altı boyutlarda sabit ve kararlı nanoaralıklar tutarlı bir şekilde üretilmiştir. Üretilen nanoaralıklar I-V ölçümleri ile karakterize edilmiş ve Simmons' modeli kullanılarak aralığın boyutu ve potansiyel bariyer yüksekliği belirlenmiştir. Yüksek rezonans frekansı ve mekanik kalite faktörüne sahip asılı yapılar elde edebilmek ve üretim esnasında yapışma probleminden etkilenmemek için, çalışma boyunca yüksek çekme gerilimli silikon nitrit ince filmler tercih edilmiştir. Fakat, yüksek stresli nitrit filmler serbest hale getirildikleri zaman şekil deformasyonuna uğramaktadırlar. Nanoaralık üretiminde olduğu gibi, yapıların konumunun muhafaza edilmesi gereken durumlarda şekil deformasyonu sorunlara sebep olmaktadır. Bu çalışmada, içsel stres gradyanı kullanılarak, asılı yapılar arasındaki mesafeyi kontrol edebilen yeni bir yöntem geliştirilmiştir. Geliştirilen teknik, sonlu eleman analizi ile simule edilmiş ve deneysel olarak gerçekleştirilmiştir. Simulasyon ile deney sonuçlarının karşılaştırılması sonucu, geliştirilen tasarımın litografik çözünürlüğün ötesinde bir aralık ayarlama kapasitesine sahip olduğu gösterilmiştir.

aieme
(to my family)

ACKNOWLEDGEMENTS

Foremost, I would like to thank Assoc. Prof. Dr. İsmet İ. Kaya who has been my advisor for all these years since I was an inexperienced and unskilled undergraduate student. This work would have not been possible without his support, encouragement and guidance. I am much indebted to him for passionately sharing his scientific vision, technical expertise and broad knowledge with me.

I wish to express my sincere gratitude to all members of physics department at Sabancı University for establishing such a fruitful academic environment. I especially acknowledge Assoc. Prof. Dr. Zafer Gedik for his theoretical contributions and Prof. Dr. Ahmet Oral and his group for their technical support as well as being on my thesis committee. I would also like to thank Assoc. Prof. Dr. Ayhan Bozkurt and Assoc. Prof. Dr. Kaan Güven for being on my thesis committee. I am also grateful to Assoc. Prof. Dr. Serhat Yesilyurt for his valuable discussions on COMSOL simulations.

I would like to thank Dr. Münir Dede for his support when I needed to use Bilkent University Advanced Research Laboratory's clean room. I acknowledge Dr. Eva Weig from LMU Munich for her valuable discussions on device fabrication. I also thank Sina Zeytinoğlu for his technical assistance during his stay at Sabancı University.

I owe special thanks to my friends and lab members. I especially thank Selda Sonuşen for her constant support and friendship. I definitely thank Cenk Yanık for making the most fun of long hours in the lab with his admirable sense of humor. I also thank Dr. Cem Çelebi for his valuable discussions on science and academic life.

I am indebted to my parents, Safiye and Fethi Günay, my little sister Ezgi Günay for their endless love and support. Finally, my most special thanks go to my husband Ahmet Şamil Demirkol for his persistent and unconditional love and support. He has always been the source of peace and joy in my life.

This work was supported by Turkish Scientific and Technological Council under Grant No. 108T492.

TABLE OF CONTENTS

1	INTRODUCTION	1
1.1	Context and Motivation	1
1.2	Structure of the Thesis	3
2	QUANTUM MEASUREMENT AND NANOMECHANICS	5
2.1	Quantum Measurement in Mesoscopic Systems	5
2.1.1	Quantum-Classical Transition.....	5
2.1.2	Heisenberg Uncertainty Principle and Standard Quantum Limit.....	7
2.2	Nano-electro-mechanical systems (NEMS).....	10
2.2.1	Introduction to NEMS.....	10
2.2.2	Nanoresonators.....	11
2.2.3	Actuation of Nanomechanical Oscillators.....	14
2.2.4	Motion Detection with NEMS	15
3	VACUUM TUNNEL JUNCTIONS (VTJ) / NANOGAPS	20
3.1	Introduction.....	20
3.2	Fabrication of VTJ / Nanogaps	22
3.2.1	Electromigration.....	22
3.2.2	Mechanically Controllable Break Junctions	24
3.2.3	Other Methods (and Conclusion).....	25
3.3	Characterization of VTJ / Nanogaps: Simmons' Model.....	28
3.4	VTJ as a Displacement Sensor.....	30
3.4.1	Theoretical Aspects	31
3.4.2	Experimental Aspects.....	32
4	NANOFABRICATION	35
4.1	Introduction.....	35
4.2	Fabrication Methods	36
4.2.1	Wafer Preparation and Standard Cleaning.....	36
4.2.2	Electron Beam Lithography (EBL).....	36
4.2.2.1	Introduction to EBL.....	36

4.2.2.2 EBL at Sabancı University	38
4.2.3 Photolithography	44
4.2.4 Metallization and Lift-off.....	47
4.2.5 Dry Etching (ICP-RIE).....	47
4.2.6 Wet Etching.....	52
4.2.7 Wafer Dicing	52
4.2.8 Wire Bonding	53
4.3 Device Fabrication Process Flow.....	53
4.3.1 Tunnel Junction/Nanogap Fabrication	53
4.3.2 Tunnel Junction-Nanobeam Embedded System Fabrication	61
5 CONTROLLED FABRICATION OF VACUUM TUNNEL JUNCTIONS	65
5.1 Introduction.....	65
5.2 Experimental Setup.....	66
5.2.1 Sample Preparation	66
5.2.2 Controlled Thermal Evaporation.....	67
5.3 Results of the Experiments and Characterization of Nanogaps.....	71
5.4 Discussions and Conclusion.....	92
6 TUNING OF NANOGAP SIZE IN HIGH TENSILE STRESS THIN FILMS	95
6.1 Introduction.....	95
6.2 High-Stress Thin Films and Nanomechanics.....	96
6.3 Device Fabrication	97
6.4 Results and Discussion.....	99
6.5 Conclusion	112
7 CONCLUSION AND FUTURE WORK	113
8 BIBLIOGRAPHY.....	115

LIST OF FIGURES

Figure 2.1:	The thermal occupation number versus the resonant frequency is plotted for temperatures 1 mK, 10 mK, 100 mK, 4 K and 300 K.....	7
Figure 2.2:	The basic operation principle of NEMS is illustrated ¹¹	10
Figure 2.3:	The illustration of a doubly clamped beam is given. L, t and w are the length, thickness and width of the beam, respectively.....	12
Figure 2.4:	The schematic on the left illustrates the working principle of magnetomotive actuation ⁶² . The colored-SEM image on the right shows the dielectric force actuation where the beam is polarized and excited by the four nearby gold electrodes (yellow) ⁶⁵	14
Figure 2.5:	The schematic and the colored-SEM image of an SET are given ¹⁶	15
Figure 2.6:	The working principle of reflectometry method developed for radio-frequency SET is illustrated ¹⁴	16
Figure 2.7:	The illustrations which show operation principle of the optical interferometry (a) and the diffraction limit (b) are given ¹³	17
Figure 2.8:	A colored SEM image of the atom point contact displacement detector and the schematic that illustrates its working principle are shown ¹⁸	18
Figure 2.9:	The SEM image of the “quantum-drum” with 6 GHz resonance frequency and the illustration of detection technique using quantum qubit are given ²⁰	19
Figure 3.1:	The illustration shows the basic operation principle of scanning tunneling microscope, STM ⁸³	21
Figure 3.2:	The SEM image of an electromigrated nanogap and the conductance of the circuit with respect to applied bias during fabrication are given ⁹³ ...	23
Figure 3.3:	The working principle of mechanically controllable break junction using three-point bending mechanism is illustrated ³⁸	24
Figure 3.4:	The schematic illustrated the working principle of chemical electrodeposition technique used for the fabrication of nanogaps ¹⁰⁷	26
Figure 3.5:	The schematic view and the SEM image of a nanogap fabricated by atomic layer deposition are shown ¹¹⁸	26
Figure 3.6:	The fabrication steps of nanogap formation using thermal evaporation are illustrated ¹²⁰	27

Figure 3.7:	The illustrations of a rectangular barrier between two metal electrodes are given for low, intermediate and high voltage ranges ⁴⁷	28
Figure 3.8:	The schematic illustrates the working principle of VTJ displacement detector ²⁷	30
Figure 3.9:	The schematic illustrates the reflectometry technique used to increase the operation bandwidth of a tunnel junction ⁷⁷	34
Figure 4.1:	The illustration shows the EBL process using monolayer PMMA.....	41
Figure 4.2:	The SEM images of metal tips fabricated with monolayer process and the alignment accuracy of the EBL system are given. These images show that a sub-10 nm gap between two metal tips can be patterned using monolayer process and the alignment accuracy of the system is on the order of sub- μm	42
Figure 4.3:	The illustration shows the EBL process using bilayer PMMA.....	43
Figure 4.4:	SEM images of the structures fabricated using MIBK:IPA (left) and IPA:deionized water (right) development are given. Ultrasonic IPA:deionized water development is preferred for more complicated structures with small openings as shown on the right SEM image.....	44
Figure 4.5:	The illustration shows both negative and positive photolithography processes.....	46
Figure 4.6:	The optical microscope image which shows the resolution of the photolithography process developed during this thesis is given.....	46
Figure 4.7:	The SEM images and EDX analysis that show the results of SF ₆ etching using DSE system are given. The SEM image on top left exhibits the isotropic nature of the etching and the image on top right shows the contamination which shunts the active device and the wafer surface. The EDX analysis at bottom proves that the contaminant is made of gold and it comes from the sputtering of the gold mask during dry etch.	49
Figure 4.8:	The SEM image shows the result of CHF ₃ /O ₂ etching in DSE system. This gas composition can etch the nitride layer anisotropically without damaging the gold mask.....	50
Figure 4.9:	The SEM images show the result of SF ₆ etching in Oxford system. This recipe provides high etch rates (400nm/min) with vertical sidewalls for LPCVD silicon nitride.....	51
Figure 4.10:	The SEM image of the device after isotropic etching of oxide layer using BOE is given.	52

Figure 4.11:	The schematic illustrates the side view and top view (inset) of the tunnel junction/nanogap device used in controlled thermal evaporation experiments.	54
Figure 4.12:	DesignCAD drawing and the pictures of the optical mask used in the first developed process flow are given.	54
Figure 4.13:	The optical microscope (a) and SEM (b) images of the devices fabricated using “Process Flow 1” are given.	56
Figure 4.14:	The short-circuit problem which shows up when the evaporation mask is coated with gold atoms during controlled thermal evaporation is described on the SEM image.....	57
Figure 4.15:	The tilted and top view SEM images of one of the devices fabricated using “Process Flow 2” are given.	58
Figure 4.16:	When the image in the middle (O ₂ plasma after development) is compared to the image on the left (no O ₂ plasma after development), it is observed that the quality of the metal film is better and the edges are cleaner. On the other hand, the image on the right shows that O ₂ plasma does not solve the contamination problem.....	59
Figure 4.17:	The SEM images show that an originally 21 nm gap width is increased to 207 nm after wet etch.	59
Figure 4.18:	The SEM images of the devices fabricated using “Process Flow 3” are given. The top images show the increase in the gap width from 27 nm after EBL (left) to 52 nm after wet etch (right). The bottom image reveals that CHF ₃ /O ₂ plasma etches the nitride layer vertically without contaminating the sample.....	61
Figure 4.19:	The schematic illustrates the isometric view of tunnel junction-nanobeam embedded system.	61
Figure 4.20:	The top view SEM image of a metal tip-nanobeam embedded device is given. The length, width and thickness of the nanobeam are 5 μm, 500 nm and 100 nm respectively (top). The side view SEM images of another device are given from different angles (bottom).....	63
Figure 4.21:	The top view SEM images show the increase in the gap width from 13 nm after EBL (left) to 108 nm after wet etch (right). The side view of the same device after wet etch is given at the bottom.....	64

Figure 5.1:	The fabrication steps of the device: (a) Top view of the device fabricated. The dashed line shows the position of the cut for the crosssectional views shown in (b) to (e). (b) PMMA coated on top of LPCVD nitride thin film, then exposed and developed, (c) a thin layer of Cr/Au coated and lifted-off, (d) the pattern is transferred to nitride layer using ICP-RIE, (e) the sacrificial oxide layer etched using BOE to form an undercut under the metal electrodes.....	66
Figure 5.2:	The figure illustrates the working principle of the controlled thermal evaporation.....	68
Figure 5.3:	The figure illustrates the “home-made” thermal evaporation system.....	69
Figure 5.4:	The pictures of the outside (top) and inside (bottom-left) of home-made thermal evaporator and the sample holder (bottom-right) are given.....	71
Figure 5.5:	The top-view (left) and tilted (right) SEM images of Sample 1 before controlled thermal evaporation are given. The initial gap size of the device is 22 nm.....	73
Figure 5.6:	The SEM images taken at different magnifications and from different viewpoints are given. The gap size cannot be measured directly using SEM because of over 3 nm resolution of the microscope and three dimensional nature of the sample.....	74
Figure 5.7:	The time-current graphs of Sample 1 during (top) and just after (bottom) thermal evaporation are given. The sample was under constant bias of 100 mV for both graphs.	76
Figure 5.8:	Tunneling resistance versus time graphs are given for 1 hour (top) and 16 hours (bottom) after nanogap formation. The applied bias was 1 V for both cases and the tunneling resistance was calculated by dividing the applied bias by the measured tunneling current.....	77
Figure 5.9:	The I-V curve of Sample 1 for $V \ll \phi/e$ is given. The device exhibits ohmic behavior for extremely low biases as the Simmons’ model suggests.	78
Figure 5.10:	The experimental data (blue dots) and the curve obtained from fitting to the Simmons’ model (red line) are given for intermediate voltages ($V < \phi/e$). The measurement is taken at room temperature, in air.....	80
Figure 5.11:	The voltage sweep measurement of Sample 1 for both negative and positive polarities is presented.	81
Figure 5.12:	The top-view SEM images of Sample 2 at different magnifications are presented. Sample 2 is a tunnel junction-nanobeam embedded system (left) and the initial gap size is 27 nm (right).....	82

Figure 5.13:	The SEM images of Sample 2 taken after controlled thermal evaporation are shown for different magnifications and viewpoints.....	83
Figure 5.14:	The time-current graphs of Sample 2 during (top) and just after (bottom) thermal evaporation are given.....	84
Figure 5.15:	The experimental data (blue dots) and the fitting curves (red line) are given for intermediate voltages ($V < \varphi/e$). The measurements were performed at room temperature for pressures, $P = 3 \times 10^{-1} \text{ mBar}$ (top) and $P = 3 \times 10^{-6} \text{ mBar}$ (top).....	86
Figure 5.16:	The potential barrier heights (top) and the gap sizes (bottom) with corresponding error values were obtained for nine measurements taken at different times in a 50 hour-period.....	87
Figure 5.17:	The gap separation with corresponding error values over 50 hours time is calculated by taking potential barrier height, φ , as a free parameter (black squares) and as a fixed parameter of 3.89 eV (red circles).....	88
Figure 5.18:	The top-view (left) and tilted (right) SEM images of Sample 3 before controlled thermal evaporation are given. The initial gap size of the device is 35 nm.....	89
Figure 5.19:	The SEM images of Sample 3 after controlled thermal evaporation are presented for various magnifications, from different viewing angles.....	90
Figure 5.20:	The graph shows the progress of the current flow between the electrodes before and after controlled thermal evaporation.....	91
Figure 5.21:	Red dots represent the measured current versus voltage characteristics of Sample 3 and the black line is the fitted curve to Simmons' model. The measurements were performed at room temperature, in atmospheric pressure.....	92
Figure 5.22:	The variation of the calculated gap separation, s , over 55 hours time is given. The potential barrier height, φ , is taken as 0.77 eV.....	92
Figure 6.1:	The fabrication steps of the device: (a) Bilayer PMMA covered on top of LPCVD nitride thin film, then exposed and developed, (b) a thin layer of Cr/Au coated and lifted-off, (c) the pattern is transferred to nitride layer using fluorine plasma, (d) the sacrificial oxide layer etched using buffered HF to suspend the nitride structures.....	100
Figure 6.2:	The first model developed for the compensation of gap widening and its basic operation principle are illustrated.....	102
Figure 6.3:	The lift-off results of bilayer EBL using MIBK:IPA (top) and ultrasonically-assisted water:IPA (bottom) development are given.	102

Figure 6.4:	The SEM images of the gap before (left) and after (right) wet etch are given for two separate devices. The gap width increases approximately 75 nm after release for both devices.....	103
Figure 6.5:	The top view (left) and side view (right) SEM images of the earliest design show that the intrinsic high tensile stress causes complex shape deformation by contracting, buckling and bending the structure.....	104
Figure 6.6:	The SEM image (top) and the FEA simulation (bottom) of the uncompensated structure. The color-code represents the displacement in the y-direction in nanometers and the surface deformation is the total displacement of the material.	105
Figure 6.7:	The FEA simulations of the new models are given. The color-code represents the displacement in the y-direction in μm and the surface deformation is the total displacement of the material (x10).	106
Figure 6.8:	FEA results for the gap size change with respect to the length of the compensation arm for the structures shown in Figure 6.7 are given. ...	107
Figure 6.9:	The SEM images of the fabricated three new structures are shown.	108
Figure 6.10:	The SEM images of Model 1, $L=2.1 \mu\text{m}$ after lift-off (top-left) and after wet etch (top-right) are given. The graph compares the calculations (SIM) and the experimental data (EXP) for different models and arm lengths.	109
Figure 6.11:	The SEM images of a device with $L = 2.9 \mu\text{m}$ before (top-left) and after (top-right) wet etch are given. The original gap width is preserved after release for this particular device. The side-view SEM image (bottom) shows that the bright shadows seen in SEM image before wet etch are oxide.....	110
Figure 6.12:	The experimental versus calculated gap width change, Δd for Model 1 is given. Symbols represent different compensation arm lengths, L . The dashed line shows the best fit with a slope of 1 with the standart error of 2.4 nm. Experimental results are -18 nm offset with respect to the simulation results.	111
Figure 6.13:	FEA results of Model 1 are given for arm lengths of a) $L = 1.6$, b) $L = 2.1$ and c) $L = 2.9 \mu\text{m}$. The color scale shows the displacement along the y-direction in nanometers. d) The graph shows the FEA results for the gap size change, Δd with respect to the arm length, L for the same structure.....	113

LIST OF TABLES

Table 2.1:	The fundamental resonance frequency of a doubly clamped beam with dimensions $L=2\ \mu\text{m}$ and $w=100\ \text{nm}$ are calculated for four different materials.	13
Table 5.1:	Summary of the important process parameters and resulting junction parameters from controlled fabrication of three different samples are given.	92

LIST OF ABBREVIATIONS

ACE	Acetone
Au	Gold
CHF ₃	Trifluoromethane
Cr	Chromium
EBL	Electron Beam Lithography
EDX	Energy Dispersive X-ray Spectroscopy
EHT	Extra High Tension
FEA	Finite Element Analysis
HF, BOE	Hydrofluoric acid, Buffered Oxide Etcher
ICP-RIE	Inductively Coupled Plasma-Reactive Ion Etching
IPA	Iso-Propyl Alcohol
LPCVD	Low-Pressure Chemical Vapor Deposition
MCBJ	Mechanically Controllable Break Junctions
MIBK	Methyl Isobutyl Ketone
NEMS	Nano-Electro-Mechanical Systems
PMMA	Poly(methyl methacrylate)
SEM	Scanning Electron Microscope
SET	Single Electron Transistor
SF ₆	Sulfur Hexafluoride
Si ₃ N ₄	Silicon Nitride
SiO ₂	Silicon Dioxide
SQL	Standard Quantum Limit
STM	Scanning Tunneling Microscope
VTJ	Vacuum Tunnel Junctions

CHAPTER 1

INTRODUCTION

1.1 Context and Motivation

Quantum mechanics predicts unexpected behaviors that are not complied with the common sense of human beings. However, the validity of the theory has been proved experimentally over and over, especially for single particles like electrons and phonons. On the other hand, quantum mechanical behaviors are not observed in the macroscopic world that we live in. Since the foundation of quantum mechanics, there has been a great interest to understand the interface between the quantum mechanical microscopic world and the classical, Newtonian, deterministic macroscopic world by answering the questions of: Can we observe the quantum mechanical properties of a macroscopic system? What conditions have to be satisfied? Theoretical and experimental studies have been carried on extensively to comprehend the extent of quantum mechanics in macroscopic world¹⁻⁴. It has found that a macroscopic system has to be cooled-down to its ground state to reveal its quantum mechanical properties⁵. Thus, the system itself and its environment must satisfy extreme conditions like sub-mK temperature and ultrahigh resonance frequency⁴⁻⁷. Additionally, the measurement device coupled to the macroscopic structure should be a quantum mechanically ideal detector because not only the observed but also the observer affects the results of the measurement in quantum mechanics⁸⁻¹⁰.

Nano-electro-mechanical systems, NEMS are promising candidates for the direct study of the quantum mechanics in macroscopic world because they have kHz-GHz resonant frequencies, high mechanical quality factors and small masses¹¹⁻¹². As a result

of their diminished size, they can be cooled down to extremely low temperatures using cryostats. Different detection schemes have been proposed, theoretically analyzed and experimentally implemented to perform measurements on nanomechanical resonators at the quantum limit^{3, 11-21}. One of the most promising ideas is to unify the sensitivity of an electron tunnel junction with the extraordinary mechanical properties of a nanoresonator. Following the invention of scanning tunneling microscope, STM²², the idea of using tunnel junctions as a motion detector was first proposed by gravitational wave community to detect very weak forces²³⁻²⁷. The theoretical calculations of that time suggested that vacuum tunneling transducers can reach quantum limit in the position measurements of a macroscopic structure²⁸⁻³⁰. Parallel with the advancements in nanotechnology, quantum-limited displacement detection based on tunnel junctions have regained a substantial theoretical interest³¹⁻³⁷. On the other hand, the experimental realization of a tunnel junction-nanomechanical resonator embedded system is nontrivial from the engineering point of view¹⁸. A metal tip has to be coupled to a suspended nanomechanical structure with a nanometer or sub-nanometer gap in between. However, the existing nanogap fabrication methods are not entirely compatible with the realization of such a system³⁸⁻⁴⁰.

The underlying motivation of this thesis is to establish a novel method for the fabrication of vacuum tunnel junctions compatible with NEMS applications. We have proposed and implemented a fabrication technique based on the controlled shrinkage of a lithographically defined gap between two metal tips or a metal tip and a nanoresonator by thermal evaporation⁴¹. In the experimental implementations a high stress silicon nitride thin film is used for the fabrication of free mechanical devices^{41, 42}. High tensile stress suspended structures are demanded in NEMS applications because they have high resonance frequencies with low dissipation, they are mechanically stable, and they are resilient to stiction problem⁴³⁻⁴⁶. However, during this study we figured out that the high-stress nitride structures experience a complex shape deformation once they are released from the layers underneath. The shape deformation becomes problematic when the precise positioning of the structures is required such as tunnel junction-nanobeam embedded systems. Consequently, the motivation of finding a solution to this problem has led to the second important outcome of this study. We proposed and implemented a new design where the distance between two suspended structures after wet etch can easily be tuned beyond the lithographic resolution limits⁴².

1.2 Structure of the Thesis

Chapter 2 presents the basic definitions, theoretical concepts and experimental aspects of quantum measurement on mesoscopic systems and nano-electro-mechanical systems, NEMS. The chapter initially addresses the question of why we cannot observe quantum mechanics in our classical, macroscopic world. This is followed by the discussion on the criteria that a mesoscopic system and its environment must satisfy to reveal the quantum mechanical features of the system. Then, the role of Heisenberg Uncertainty Principle on quantum measurements is explained and the Standard Quantum Limit of a simple harmonic oscillator is calculated. In the second part of the chapter, NEMS and their basic operating principles are introduced. After that, the most essential components of NEMS, nanoresonators and their physical properties such as resonant frequency and mechanical quality factor are explained. Finally, different actuation and detection methods from literature are presented.

In Chapter 3, the theoretical and experimental aspects of the vacuum tunnel junctions, VTJ or nanogaps are provided. These two terms are used interchangeably throughout the thesis. First of all, the physics of electron tunneling and its applications are discussed. Then, different nanogap fabrication methods from literature like electromigration, mechanically controllable break junction, electrodeposition, etc. are presented with an emphasis on their weaknesses and strengths. After that, Simmons' Model, a theoretical model of tunnel junctions, is discussed in detail⁴⁷. This model is widely used in literature for the characterization of fabricated nanogaps by fitting the experimental data to the Simmons' equation. Same model is also utilized in Chapter 5 for the characterization of nanogaps fabricated during this work. In the last part, the idea of using VTJ as a displacement detector is introduced. The theoretical calculations show that VTJ detectors are promising candidates for motion detection at quantum limit. However, there are technical challenges for the experimental realization of a nanoresonator-tunnel junction embedded system.

Chapter 4 explains the device fabrication techniques and methods developed and implemented during this work. The recipes and process parameters of each fabrication step are provided in detail. Two process flows for metal tip-metal tip and suspended doubly clamped beam-metal tip systems are formulated.

Chapter 5 describes a new nanogap fabrication method that we have successfully developed and implemented during this work. The method is based on the controlled shrinkage of lithographically defined gaps using in-situ controlled thermal evaporation. High stability gaps with sub nanometer dimensions have been produced with this method. First of all, the sample preparation procedure and the details of the home-made in-situ controlled thermal evaporation system are provided. Then, the experimental results of three successfully fabricated nanogaps are presented using high-magnification SEM images and electrical measurements. The characteristics of nanogaps such as gap size and potential barrier height are interrogated by fitting the current-voltage measurements of the device to the Simmons' equation. The chapter ends with a discussion on the experimental outcomes and future directions.

In Chapter 6, we proposed and implemented a new design which utilizes the high tensile stress in Si_3N_4 thin films to control the gap size between two suspended structures. During device fabrication, we realized that the lithographically defined gap widens once the high stress Si_3N_4 structures are released from the oxide layer. The nanogap fabrication is impaired seriously by this widening of the gap problem and hence, a novel solution to this problem is sought and found. The chapter starts with the problem statement and continues with the literature review on the use of high-tensile stress thin films in nanomechanics. It is followed by a discussion on the new device geometries that we designed and implemented. The change in the gap width of real devices is compared with the finite element analysis results. The chapter finishes by addressing the capability of this new design to control the gap width between two suspended structures made of high tensile stress thin film.

Chapter 7 concludes the main body of the thesis and provides future directions.

CHAPTER 2

QUANTUM MEASUREMENT AND NANOMECHANICS

2.1 Quantum Measurement in Mesoscopic Systems

The validity of quantum theory has been proved in tiny objects like electrons, phonons and single molecules. It is observed that they obey the extraordinary rules of quantum mechanics. On the other hand, macroscopic objects are ordinarily governed by classical Newtonian mechanics. One of the fundamental inquiries of physics is to discover the extent to which the quantum mechanics can be applied in macroscopic world. It is believed that the quantum features of a macroscopic system can be unveiled under extreme conditions. Theoretical and experimental studies have been carried out to comprehend these conditions and satisfy them in real world. In quantum mechanics both the observed and the observer affect the result of the measurement. Here, first the basic criterion that a system itself must satisfy to enter the quantum regime, low thermal occupation number, is discussed. Then, the fundamental constraints and uncertainties specific to the measurement process itself are presented. Throughout these theoretical calculations the macroscopic object is assumed to behave like a simple harmonic oscillator.

2.1.1 Quantum-Classical Transition

Theoretically it is possible to unveil the quantum mechanical features of an ordinarily classical object when the thermal fluctuation energy ($k_B T$) does not obscure the mechanical quanta energy ($\hbar\omega$)^{6, 9, 48-50}.

$$\hbar\omega \geq k_B T. \quad (2.1)$$

Here \hbar is the Planck's constant, $\omega/2\pi$ is the oscillator's resonance frequency, k_B is the Boltzmann constant and T is the equilibrium temperature of the oscillator and its environment. This condition necessitates a harmonic oscillator which has GHz-range resonance frequency and operates at sub-K temperature. A quantity called "thermal occupation number, n_{th} " is introduced to more elaborately define the quantum-classical transition criteria for a harmonic oscillator⁴⁸:

$$\langle n_{th} \rangle = \frac{1}{2} + (e^{\hbar\omega/k_B T} - 1)^{-1}. \quad (2.2)$$

Thermal occupation number can be interpreted as the average number of phonons in the oscillator for a given state. If the energy of each phonon is given by $\varepsilon = \hbar\omega$, the total energy of the oscillator becomes $E = \langle n_{th} \rangle \varepsilon$ ⁵⁰. Accordingly, the 1/2 term in Equation 2.2 corresponds to the ground state energy of the harmonic oscillator. It has already mentioned that the basic criterion to enter the quantum realm is to eliminate the classical fluctuations which demands very high $\hbar\omega/k_B T$ ratio. In other words, low thermal occupation number is desired for quantum measurements. In the extreme case when the temperature goes to absolute zero, thermal occupation number approaches to 1/2, which means cooling the oscillator to its ground state. In Figure 2.1, the thermal occupation number versus oscillator's resonance frequency is plotted for five different temperatures between 1 mK and 300 K. The highest mechanical resonance frequencies that are experimentally realized are on the order of GHz for nanoresonators^{20, 51}. Therefore, the temperature has to be smaller than 100 mK to approach the ground state of the nanoresonator. In today's technology, temperatures below 10 mK can be achieved in cryogen free dilution refrigerators using ³He/⁴He mixture.

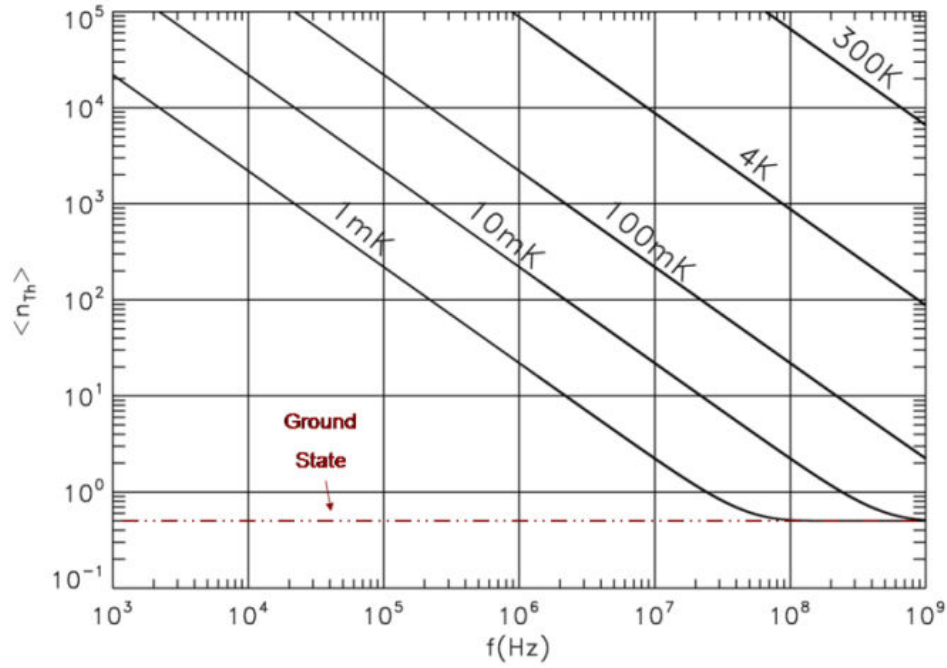


Figure 2.1: The thermal occupation number versus the resonant frequency is plotted for temperatures 1 mK, 10 mK, 100 mK, 4 K and 300 K.

2.1.2 Heisenberg Uncertainty Principle and Standard Quantum Limit

In quantum mechanics, cooling the oscillator down to its ground state is not sufficient to observe the quantum behavior of the system. Quantum mechanics also enforce some constraints on the sensitivity of the measurement process. The physical ultimate limit of the measurement accuracy is determined by the Heisenberg Uncertainty Principle⁵²:

$$\Delta x \Delta p \geq \hbar/2 . \quad (2.3)$$

In this equation, Δx and Δp represent the root-mean-square deviations of oscillator's position and momentum from their mean values, respectively. The uncertainty principle implies that an object cannot have precisely defined values of position and momentum simultaneously. Despite the fact that the uncertainty relation is a fundamental property of a quantum object's physical state, it can also be interpreted as the uncertainty in the measurement of observables such as position and momentum⁵⁰:

$$\Delta x_{\text{measurement}} \Delta p_{\text{perturbation}} \geq \hbar/2 . \quad (2.4)$$

In this interpretation, $\Delta x_{\text{measurement}}$ is the error in the measurement of the position of the oscillator and $\Delta p_{\text{perturbation}}$ is the perturbation on the oscillator caused by the measurement process⁵⁰. The position can be measured with arbitrary accuracy for one single instant measurement. On the other hand, the accuracy is limited for continuous measurements as a result of the back action of the momentum uncertainty on the succeeding position measurement and vice versa. The minimum uncertainty in position for two consecutive measurements is called as the “standard quantum limit”⁵⁰.

The standard quantum limit of a simple harmonic oscillator in its ground state can be calculated using Heisenberg representation. In this representation, the equations of motion for the position and momentum of an oscillator are given by⁵³:

$$x(t) = x(0) \cos(\omega t) + (p(0)/m\omega) \sin(\omega t), \quad (2.5)$$

$$p(t) = -m\omega x(0) \sin(\omega t) + p(0) \cos(\omega t). \quad (2.6)$$

The corresponding variances of position and momentum are calculated as⁶:

$$\Delta x(t) = \sqrt{(\Delta x(0) \cos(\omega t))^2 + ((\Delta p(0)/m\omega) \sin(\omega t))^2}, \quad (2.7)$$

$$\Delta p(t) = \sqrt{(-m\omega \Delta x(0) \sin(\omega t))^2 + (\Delta p(0) \cos(\omega t))^2}. \quad (2.8)$$

In these equations, $\Delta x(0)$ is the initial error in the position and $\Delta p(0)$ is the momentum perturbation coming from the first measurement and their relation is given by the uncertainty principle: $\Delta p(0) \geq \hbar/2\Delta x(0)$. When this inequality is inserted into Equation 2.7, the variance of position can be written as a function of the initial error in position only:

$$\Delta x(t) \geq \sqrt{(\Delta x(0) \cos(\omega t))^2 + ((\hbar/2m\omega \Delta x(0)) \sin(\omega t))^2}. \quad (2.9)$$

When Equation 2.9 is differentiated with respect to $\Delta x(0)$ and equalized to zero, the initial error in position which minimizes the time dependent variance of position can be found:

$$\Delta x(0)_{min} = \sqrt{\hbar/2m\omega} \equiv \Delta x_{SQL} . \quad (2.10)$$

The standard quantum limit, SQL is the ultimate limit to the accuracy of a simple harmonic oscillator's position measurement. In other words, SQL is theoretically the best sensitivity a displacement sensor can achieve. In real world, the sensitivity of the measurement is further deteriorated due to the back-action force that the detector exerts on the oscillator and the unavoidable noises added by the electronic equipment like amplifiers. Mechanical oscillators with higher SQL are demanded in quantum measurements because the sensitivity of the motion detector should approach the SQL of the oscillator. Equation 2.10 shows that SQL is inversely proportional with term $m\omega$. As a result of their low masses, this term is much smaller for the nanoresonator than for the bulk structures. For instance, a typical nanoresonator with a mass of 10^{-16} kg and resonance frequency of 100 MHz will result in a SQL of 3×10^{-14} m. On the other hand, a daily-life bulk structure with a mass of 10 kg and resonance frequency of 1 kHz will have a SQL of 3×10^{-20} m. The SQL of nanoresonator is six orders of magnitude larger than the SQL of a bulk structure. Therefore, theoretically, nanoresonators should reveal their quantum mechanical properties at a much larger length scale.

In summary, most basically, two criteria must be satisfied to perform quantum measurements on macroscopic bodies. First of all, the mechanical oscillator should resonate at GHz frequencies and operate at sub-100 mK temperatures to cool down to its quantum ground state. Secondly, the displacement detector's sensitivity should approximate the SQL of the oscillator which is more viable for nanoresonators. In this context, nanomechanical devices are favored as a result of their diminished size, low mass and high resonance frequency.

2.2 Nano-electro-mechanical systems (NEMS)

2.2.1 Introduction to NEMS

A typical NEMS consists of a mechanical resonator coupled to a detector of comparable size. At least one of resonator's dimensions should be in nanometer range. The basic working principle of NEMS is similar to conventional electromechanical systems and is illustrated in Figure 2.2. In NEMS, transducers are employed to convert electrical signal to mechanical stimuli or vice versa. The input transducer, in other words the actuator, converts the electrical signal to physical stimuli to drive the mechanical element. This process is called as "actuation". On the other hand, the output transducer, a sensor or a detector, measures one of the physical properties of the mechanical element and converts it to an electrical signal. The process is called as "detection". The geometry and the size of the mechanical element vary from system to system and there are many different actuation and detection techniques.

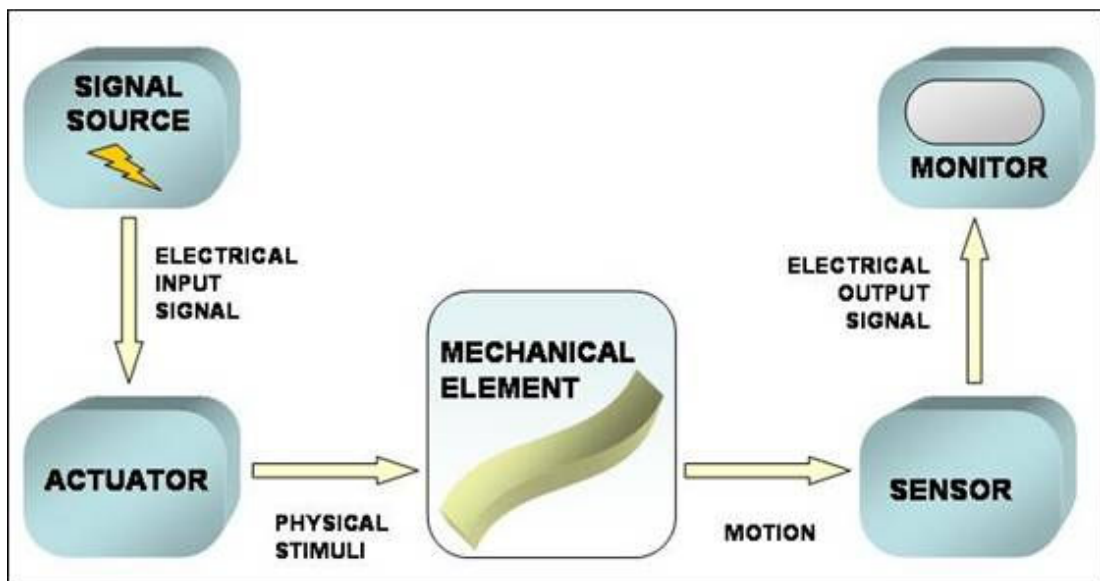


Figure 2.2: The basic operation principle of NEMS is illustrated.

Ultrafast and ultrasensitive mass ⁵⁴, displacement ⁵⁵, and strain ⁵⁶ measurements can be performed using NEMS. As a result of their diminished size, nanomechanical resonators have extraordinary mechanical properties such as small inertial mass and very high resonance frequency ¹³. Therefore, besides metrology, NEMS also serve the fundamental research on the interesting internal dynamics of a nanoresonator such as energy dissipation and mechanical quality factor issues ⁴³⁻⁴⁵. Last but not least, NEMS are promising systems for the detection of quantum mechanical behavior in macroscopic objects. Despite their diminished size, nanoresonators are still macroscopic structures which consist of billions of atoms and have many degrees of freedom. Therefore, their properties and behavior under ordinary conditions are explained by classical, Newtonian mechanics. Nonetheless, when the extreme conditions of GHz mechanical resonance frequency, sub-100 mK operating temperature and ultra-small effective mass are satisfied, quantum mechanical behavior of the mechanical structure can be revealed. In the previous section, it has been shown that these extreme conditions can be fulfilled using nanomechanical structures. A quantum mechanically ideal position detector which has femtometer-range sensitivity and can keep up with the GHz speed of the resonator is demanded for this kind of measurements. In the following sections, first the mechanical properties of a nanoresonator will be discussed and then, the most prominent actuation and displacement detection techniques from literature will be presented.

2.2.2 Nanoresonators

One of the fundamental elements of the NEMS devices is the nanomechanical resonator. Nanomechanical resonators are suspended structures with minimum one clamp point. They are confined to nanometer scale in at least one degree of freedom (width, thickness or length). Different geometries are utilized for the fabrication of nanoresonators such as doubly-clamped beam ^{16-19, 43-46, 51}, cantilever ⁵⁷⁻⁵⁹ and paddle ^{20, 60}. In this work, we prefer to study and use doubly clamped flexural nanobeam which is also the most extensively employed geometry in literature. Therefore, the resonant frequency of fundamental modes and the mechanical quality factor are explained only for this particular geometry.

A doubly clamped beam as illustrated in Figure 2.3 can be modeled using the continuum theory. The resonance frequencies for the fundamental flexural modes are calculated by the classical Euler-Bernoulli Beam equation under the assumptions of⁶¹:

1. The beam is a prismatic, untwisted and straight structure composed of an isotropic, linear elastic material.
2. The length of the beam is much larger than the width and thickness of the beam.
3. Displacements from the equilibrium are very small compared to the length of the beam.

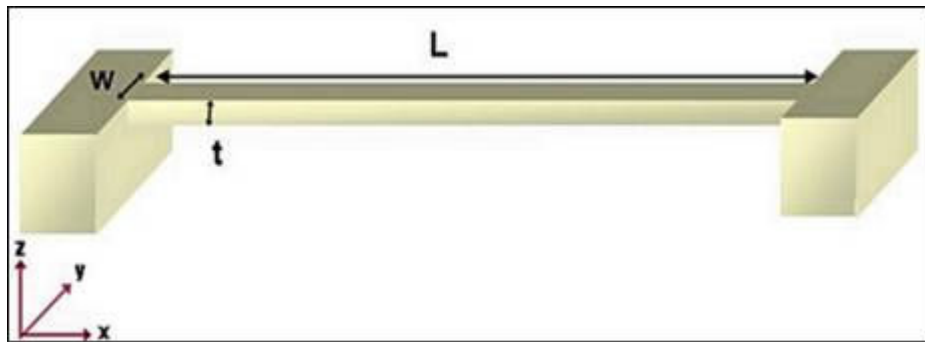


Figure 2.3: The illustration of a doubly clamped beam is given. L , t and w are the length, thickness and width of the beam, respectively.

The resonance frequency of the fundamental modes of a doubly-clamped beam is given by the equation⁶²:

$$f_n = C_n \sqrt{E/\rho} (w/L^2) . \quad (2.11)$$

In this equation, E is the Young's modulus, ρ is the density, L is the beam length and w is the width of the resonator in the direction of the motion. C_n is a constant which depends on the mode number, n and can be calculated numerically. For instance, the first normal mode which is the fundamental mode has a resonance frequency of⁶³:

$$f_0 = 1.027 \sqrt{E/\rho} (w/L^2) . \quad (2.12)$$

According to this formula, the natural resonance frequency of a nanoresonator depends not only on the dimensions of the structure but also on the properties of the material used. The width of an in-plane flexural nanobeam is equal to the thickness of the thin film used for the fabrication which is typically on the order of 100 nm. In Table 2.1, the fundamental resonance frequencies of a doubly clamped beam with $L = 2 \mu\text{m}$ and $w = 100 \text{ nm}$ are calculated for different materials using Equation 2.12. These calculations show that stiffer materials with high elastic modulus such as silicon nitride or silicon carbide produce higher resonance frequencies. Experimentally, one of the highest resonance frequencies reported for a doubly clamped beam is over 1 GHz for SiC⁵¹. Recently, a much higher resonance frequency over 6 GHz is reported using a multilayer (Al-AlN-Al) paddle geometry²⁰.

Table 2.1. The fundamental resonance frequency of a doubly clamped beam with dimensions $L = 2 \mu\text{m}$ and $w = 100 \text{ nm}$ are calculated for four different materials.

	Young's Modulus, E (GPa) ⁶⁴	Density, ρ (kg/m ³) ⁶⁴	Fundamental Resonance Frequency, f_0 (Hz)
Si	129-187	2330	215 MHz
Silicon Dioxide, SiO ₂	73	2200	154 MHz
Silicon Nitride, Si ₃ N ₄	304	3300	256 MHz
Silicon Carbide, SiC	430	3300	305 MHz

The other important parameter of a nanoresonator is the mechanical quality factor. It is a measure of the damping for a resonator and is affected by various dissipation sources such as the metal layers on the structure⁶⁵ and the viscosity of the environment (vacuum, air or fluid)^{66,67}. High mechanical quality factors are demanded for improved sensitivities. Unfortunately, experimental results show that the mechanical quality factor decreases as the dimensions of the nanoresonator diminish¹³. Nonetheless, quality factors over one million has been reported for nanoresonators using high tensile stress materials⁴⁶.

2.2.3 Actuation of Nanomechanical Oscillators

The actuation is performed to drive a nanoresonator to one of its resonance modes. The resonance frequency and the quality factor of the nanoresonator can be experimentally determined as a result of actuation. There are various high frequency actuation techniques such as magnetomotive^{18, 51, 62, 63, 68}, capacitive⁶⁹, thermal⁵⁶, dielectric force⁶⁵, piezoelectric⁷⁰, and ultrasonic⁶⁰ actuation. Each technique has its own advantages or disadvantages and the preference depends on the application. For instance, in magnetomotive actuation, a Lorentz force is applied to the resonator by passing an alternating current through the beam in the presence of a strong magnetic field. The nanobeam has to be metallized in magnetomotive actuation to pass the current. This is the most widely used actuation technique in NEMS since most of the nanoresonators are already metallized for fabrication or detection purposes and strong magnetic field is generally available in sub-K cryostats. On the other hand, the metal coating reduces the quality factor of the nanoresonator. Therefore, in some applications alternative techniques that do not demand metallization of the nanobeam such as piezoelectric and dielectric force actuation are preferred to obtain higher mechanical quality factors. The pictures of two different actuation scheme, magnetomotive and dielectric force, are presented in Figure 2.4.

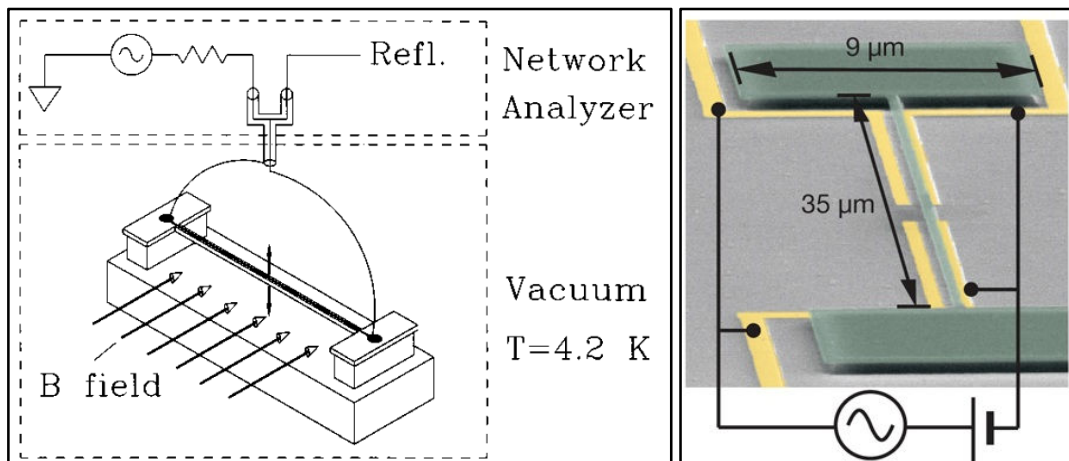


Figure 2.4: The schematic on the left illustrates the working principle of magnetomotive actuation⁶². The colored-SEM image on the right shows the dielectric force actuation where the beam is polarized and excited by the four nearby gold electrodes (yellow)⁶⁵.

2.2.4 Motion Detection with NEMS

The position measurement of a nanomechanical resonator can be performed by several different techniques such as single electron transistor^{14, 16, 71-73}, optical interferometry^{69, 74-76}, and atomic point contact¹⁸ to name a few. As mentioned before, a position detector should have a sensitivity of femtometer range and operate at GHz frequencies to be able to perform displacement measurements at quantum limit. In most cases, the sensitivity of the detector is limited by the back-action force which is the perturbation that the detector applies on the nanoresonator during the measurement¹¹. Therefore, the back-action noise should be quantum-limited for a quantum mechanically ideal detector.

One of the most widely implemented and studied displacement detector in NEMS community is the single electron transistor, SET. It is a capacitive transducer based on an intrinsically quantum mechanical phenomenon, coulomb-blockade⁷³. It consists of a metal island between two metal junctions and a gate electrode that is capacitively coupled to the island and the nanoresonator as shown in Figure 2.5¹⁶. The gate capacitance changes as the nanoresonator oscillates which in turn modulates the potential of the metal island. The change in island potential is reflected to the drain-source current. Briefly, one can deduce the nanoresonator's motion by monitoring the drain-source current.

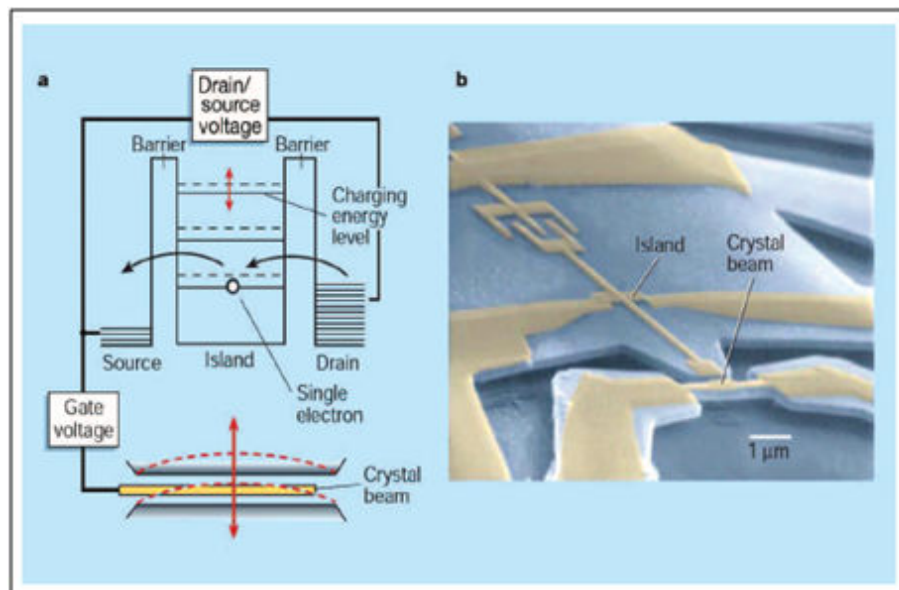


Figure 2.5: The schematic and the colored-SEM image of an SET are given¹⁶.

A conventional SET cannot operate at high frequencies because the high impedance of the device and the parasitic capacitances from the wiring limits the operation bandwidth by $1/RC$. Schoelkopf *et. al.* developed a new method called as “reflectometry” to increase the speed of SET from kHz frequencies to MHz range ¹⁴. This method has also been employed to increase the increase the speed of other high impedance applications such as atomic point contact ¹⁸, scanning tunneling microscope ⁷⁷. As shown in Figure 2.6, the high impedance of the SET is matched down to the impedance of the coaxial cables using an LC transformer. A high frequency read-out circuit system follows the LC transformer to amplify and transmit the signal coming from SET. One of the best sensitivity achieved using radio-frequency SET is 4.3 times the quantum limit for a 19.7 MHz nanobeam at 56 mK ¹⁷. This measurement could not reveal any quantum signatures because the thermal occupation number of the nanobeam was high ($n_{th} = 58$). Despite the fact that many state-of-art experiments have been carried out using radio-frequency SET, none of them could observe quantum mechanical behavior of a nanoresonator. Recent theoretical studies showed that the displacement sensitivity of the SET cannot reach the quantum limit because of the excessive back-action force that the SET applied on the nanobeam. It is theoretically calculated that the back-action noise is larger than the maximum allowed by quantum mechanics and SET is not an ideal amplifier for quantum measurements ^{10, 73, 77}.

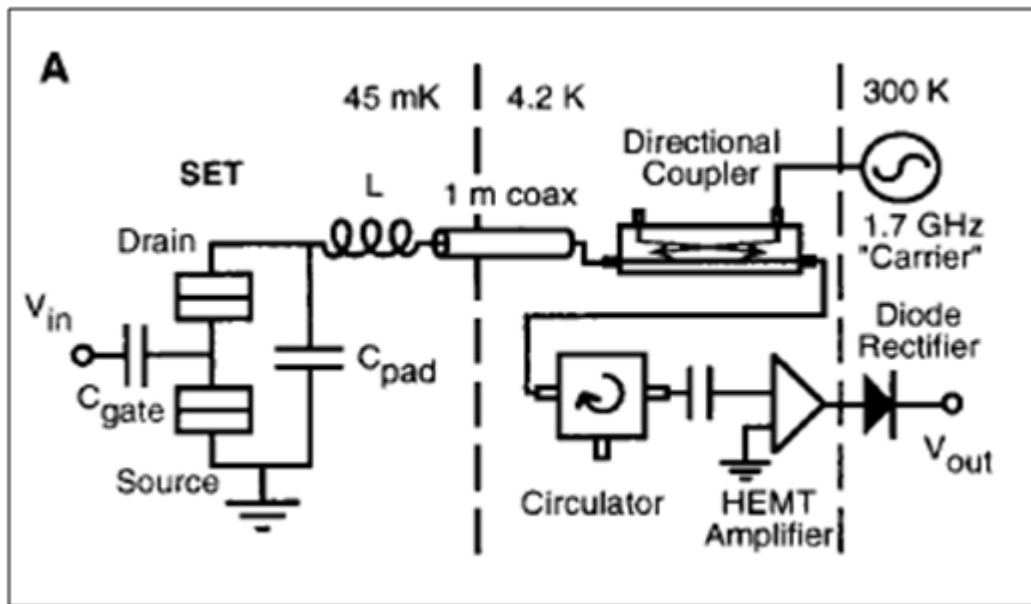


Figure 2.6: The working principle of reflectometry method developed for radio-frequency SET is illustrated ¹⁴.

The other popular motion detection method in NEMS is the optical interferometry⁷⁴. In this method, a laser beam is aligned to the midpoint of the nanoresonator. The amount of the reflected light changes as a result of the nanoresonator's motion and a photo-detector determines the modulations in the reflected light to interpret the displacement of the nanoresonator. Optical detectors can operate at high-frequencies, they are non-destructive and the back-action noise is quantum-limited. They are especially preferred in application where the metallization of the nanoresonator is avoided to increase the mechanical quality factor. Despite these advantages, optical interferometry is ultimately limited by a physical phenomenon called diffraction^{74, 79}. The diffraction phenomenon limits the resolution of the optical sensor when the width of the nanoresonator becomes smaller than the wavelength of the light which is the case for NEMS applications¹³.

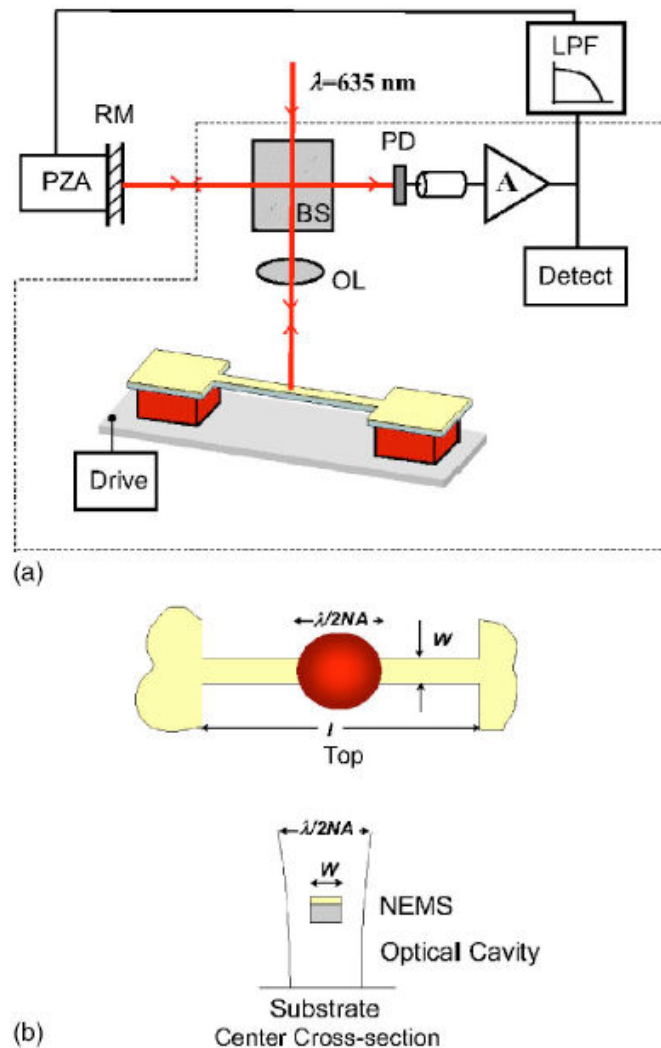


Figure 2.7: The illustrations which show operation principle of the optical interferometry (a) and the diffraction limit (b) are given¹³.

In addition to these two common techniques, atomic point contact displacement detection is noteworthy because it shares parallel motivation with this thesis¹⁸. In this method, a gold doubly-clamped beam is coupled to a gold metal tip through an atomic point contact formed by electromigration. The nanobeam is actuated by magnetomotive force and the speed of the detection is increased by using reflectometry method. The displacement of the nanobeam is deduced from the modulation in the tunneling current across the atomic point contact as shown in Figure 2.8¹⁸.

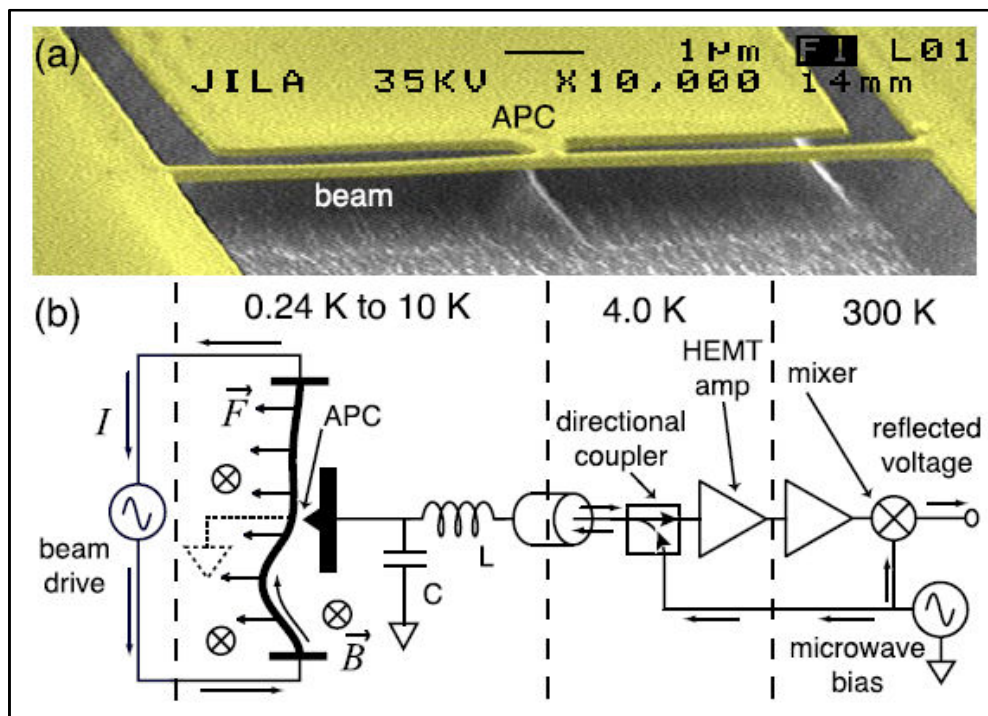


Figure 2.8: A colored SEM image of the atom point contact displacement detector and the schematic that illustrates its working principle are shown¹⁸.

Even though the electron tunneling is intrinsically a quantum mechanical phenomenon, they reported that the sensitivity of the detector is 42 times the standard quantum limit. The sensitivity is diverged from the quantum limit due to the excessive back action force created by the momentum transfer of the tunneling electrons¹⁸. There are two drawbacks of this method:

1. The suspended structures are made entirely out of gold and hence the resonance frequency and the quality factor of the nanobeam are not high enough to enter the quantum regime. The use of metal for the entire structure is an unavoidable result of the fabrication method employed to form the atomic point contact.

2. The coupling strength between the nanoresonator and the metal tip has to be fine tuned to obtain a quantum ideal detector ^{2, 10, 32, 33}. Experimentally, the coupling strength corresponds to the distance between the resonator and the metal tip and it is different for a tunnel junction and a point contact ⁸⁰. Therefore, it must be ensured that the device is fabricated and operated at tunneling regime.

Numerous other alternative NEMS devices are proposed and implemented with the motivation of approaching the quantum limit. Recently, a prominent study has been reported by Cleland and his group ²⁰. They managed to cool down a macroscopic resonator to its quantum ground state. In this study, a multilayer drum-shape resonator with a 6 GHz dilatational resonance frequency is coupled to a quantum-bit as shown in Figure 2.9. Such high resonance frequency is achieved as a result of the extraordinary geometry and multilayerness of the resonator. They managed to create single quantum excitations in the resonator which is the first sign of quantum control over a macroscopic mechanical system

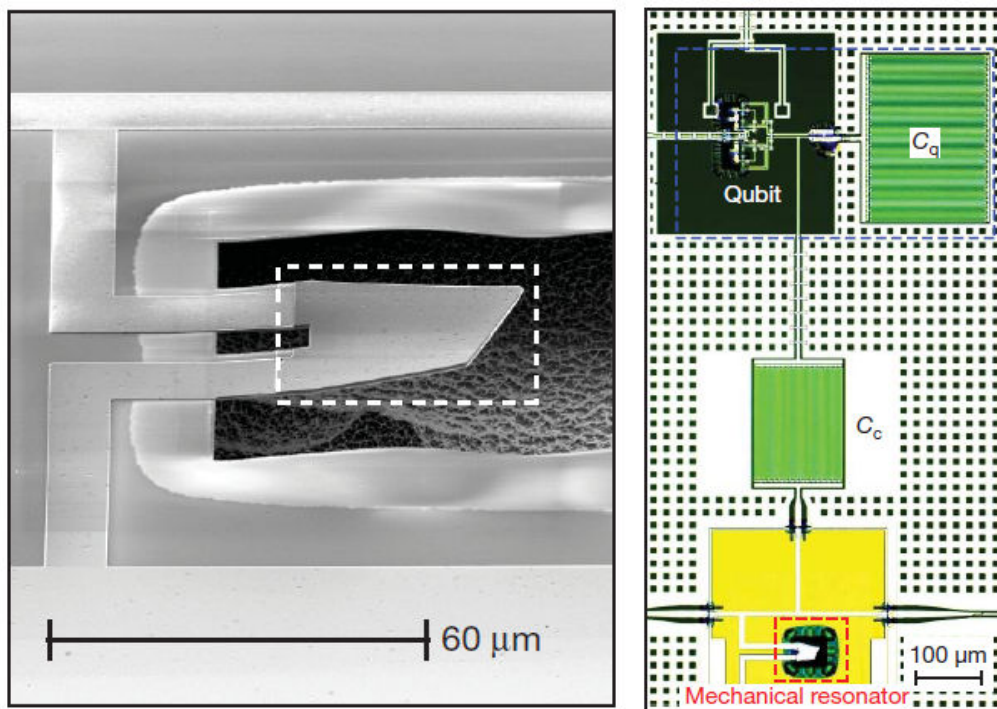


Figure 2.9: The SEM image of the “quantum-drum” with 6 GHz resonance frequency and the illustration of detection technique using quantum qubit are given ²⁰.

CHAPTER 3

VACUUM TUNNEL JUNCTIONS (VTJ) / NANOGAPS

3.1 Introduction

In classical mechanics a particle cannot overcome a potential barrier that is higher than its total energy. On the other hand, in quantum mechanics there is a probability that the particle will pass across the potential barrier. This phenomenon is known as “quantum tunneling”^{80, 81}. When numerous number of electrons are incident to a potential barrier, a tunneling current can be detected as a result of this probabilistic nature. The tunneling current density is given by the equation⁸¹:

$$j = (e^2V/4\pi^2L\delta\hbar)\exp(-2L/\delta) . \quad (3.1)$$

In this equation e is the charge of the electron, V is the bias voltage, L is the thickness of the barrier, and \hbar is the Planck’s constant. δ is the characteristic scale of length for tunneling and it is calculated by:

$$\delta = \hbar/\sqrt{2m_e(U - E)} . \quad (3.2)$$

Here, m_e is the mass of the electron, U is the height of the potential barrier and E is the kinetic energy of the electron. If the tunneling occurs through a vacuum between two metal electrodes, $(U-E)$ term corresponds to the work function of the metal. The exponential term in Equation 3.1 implies that the tunneling current density dramatically depends on the distance between the metal electrodes, L . For the typical values of metals’ work functions (4-5 eV), the characteristic scale of length, δ is approximately

1 Å. Hence, Equation 3.1 suggests that a 1 Å variation in the L corresponds to an order of magnitude change in the tunneling current. This sensitivity of the tunneling current to L forms the basis of a well known application: scanning tunneling microscope, STM²². In STM, a tunnel junction/nanogap is formed between an atomically sharp metal tip and a metal surface and the tunneling current is monitored as the tip scans the surface (Figure 3.1). The tunneling current modulates as the height of the surface features changes. STM can measure the surface topography with a sensitivity of 0.01 Å⁸².

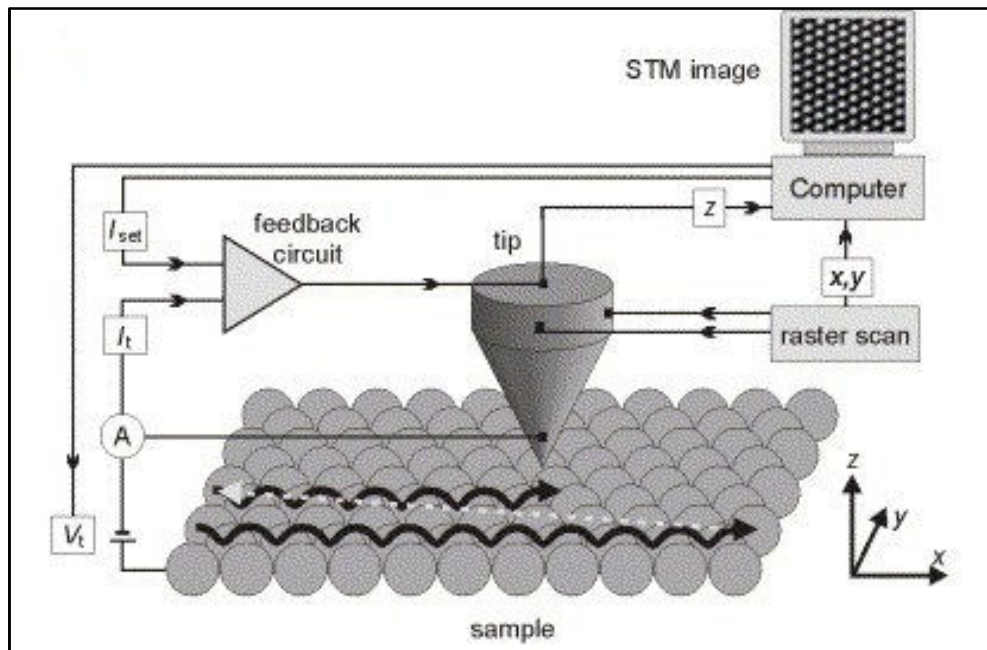


Figure 3.1: The illustration shows the basic operation principle of scanning tunneling microscope, STM⁸³.

Beyond the microscopy, tunnel junctions or nanogaps embedded in nano-scale devices are highly demanded in nanotechnology. In STM, a bulk system consisting of complicated electronics and piezo materials is used to approach the metal tip to the sample surface in a controlled manner. On the other hand, the realization of a nanogap in small-sized devices such as NEMS necessitates special fabrication techniques. In this chapter, first the importance of nanogaps in today's technology will be underlined and the existing fabrication techniques in literature will be presented. Secondly, Simmons' Model, which is a widely used theoretical model for the characterization of nanogaps, will be introduced. Finally, a displacement detector based on tunneling current will be discussed from theoretical and experimental points of view.

3.2 Fabrication of VTJ / Nanogaps

A vacuum tunnel junction, VTJ or a nanogap is composed of two metal tips with a nanometer or sub-nanometer gap. In this work, VTJ and nanogap terms are used interchangeably and both correspond to devices that operate in the tunneling regime. Nanogaps can be used to electrically probe nanostructures such as single molecules^{40, 84}, nanocrystals⁸⁵, and biomolecules^{86, 87}. Conventional silicon technology has almost reached its limit and nanostructures are intended to be used as the active building blocks of next generation integrated circuits⁸⁸⁻⁹⁰. Nanogaps are needed to study the electrical properties of nanostructures and to integrate them into the electronic devices. Nanogaps can also be used in the context of displacement detection of nanoresonators as mentioned in section 2.2.4^{18, 26}.

Even the resolution of the state of the art micro/nano fabrication techniques such as electron or ion beam lithography is not enough for the direct patterning of vacuum tunneling junctions which require sub-nanometer resolution. Therefore, alternative efficacious fabrication techniques are required for the realization of nanogaps. A diverse range of nanogap fabrication techniques can be found in literature. Most of them are based on either the breaking or etching of metallic constrictions or the reduction of originally wide gaps using various deposition techniques. The two most common methods, nanogap formation by electromigration^{39, 91-99} and mechanically controllable break junctions^{86, 100-106}, and the other noteworthy techniques¹⁰⁷⁻¹²⁰ will be discussed in the following subsections.

3.2.1 Electromigration

Electromigration has been known for a long time as a failure mechanism in microelectronic circuits¹²¹. It is first utilized for the fabrication of a nanogap by Park *et. al.*³⁹. When a current is passed through a metal, the moving electrons transfer some of their momentum to the ion cores by inelastic scattering. If the current density and hence the momentum transfer are large enough, the ion cores can start to move gradually which results in the actual displacement of the material³⁸. For the fabrication of a nanogap, a large current density is passed through a thin metallic nanowire or a metal constriction until a break occurs as result of the movement of the metal atoms.

There are two important parameters in electromigration: current density and temperature⁹⁶. The current density determines the number of moving electrons and the amount of momentum transfer to the ion cores. The temperature affects the mobility of the ion cores and the conductivity of the metal which in turn changes the current density under constant bias. Control over these two parameters during processing is very crucial for the successful formation of nanogaps using electromigration. Therefore, electromigration is generally performed at cryogenic temperatures to avoid over-heating⁹⁵ and the applied power is controlled with a feedback mechanism throughout the processing⁹⁶.

Nanogaps below 5 nm have been reported many times using electromigration⁹¹⁻⁹⁹. On the other hand the main problem with electromigration is that it is a self-terminating process and the exact position and size of the nanogap cannot be predetermined. Even though it is possible to apply this method in ambient environment⁹⁷, special conditions such as low temperature and high vacuum are required for the fabrication of smaller and cleaner nanogaps. Last but not least, another drawback of this method is the metal debris remained inside the gap after fabrication which degenerates the electrical behavior of the junction³⁸.

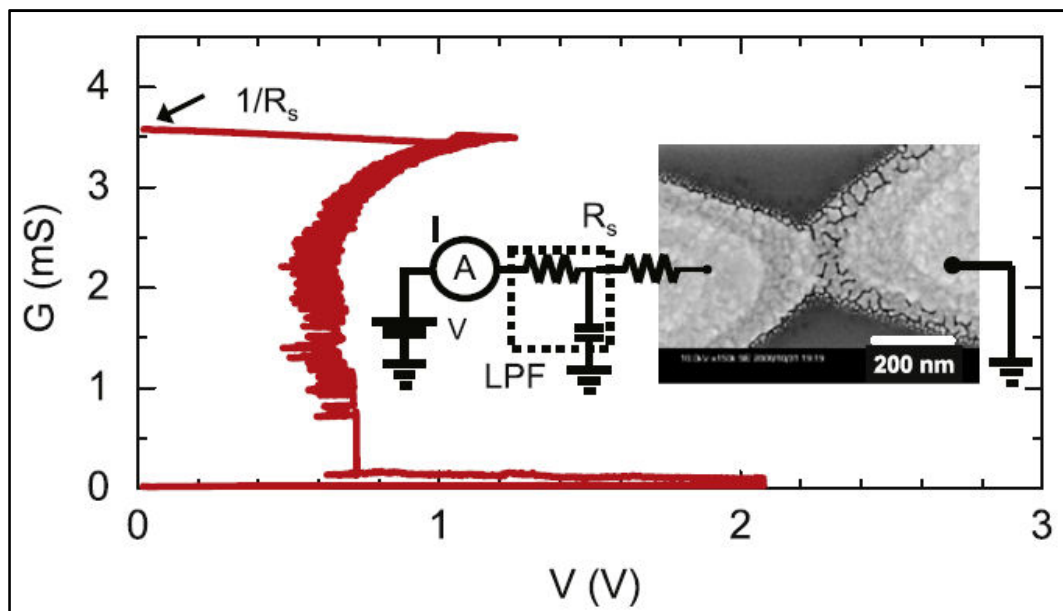


Figure 3.2: The SEM image of an electromigrated nanogap and the conductance of the circuit with respect to applied bias during fabrication are given⁹³.

3.2.2 Mechanically Controllable Break Junctions

Mechanically controllable break junctions, MCBJ was first invented by Moreland and Ekin in 1985¹²². In this technique, a three-point bending mechanism is used to break a metal wire as shown in Figure 3.3³⁸. A notched metal wire is glued on a flexible substrate and the two ends of the substrate are fixed using counter supports. An upward force is applied to the middle of the substrate where the notch is placed. The amount of the force is finely adjusted using piezo materials to be able to bend the substrate in a controlled manner until the wire is fractured⁴⁰. Once the nanogap is formed, it is possible to fine tune the gap size using the delicate piezoelectric system. The fabrication is generally performed in low temperature and high vacuum to obtain cleaner nanogaps. The main advantages of this technique are; the gap size can be adjusted continuously and the fabricated nanogaps are very stable (0.2 pm/h)¹⁰⁰. Nanogaps with different sizes, from point contact to tunneling regime can be realized and the discrete universal conductance steps can be observed using MCBJ technique

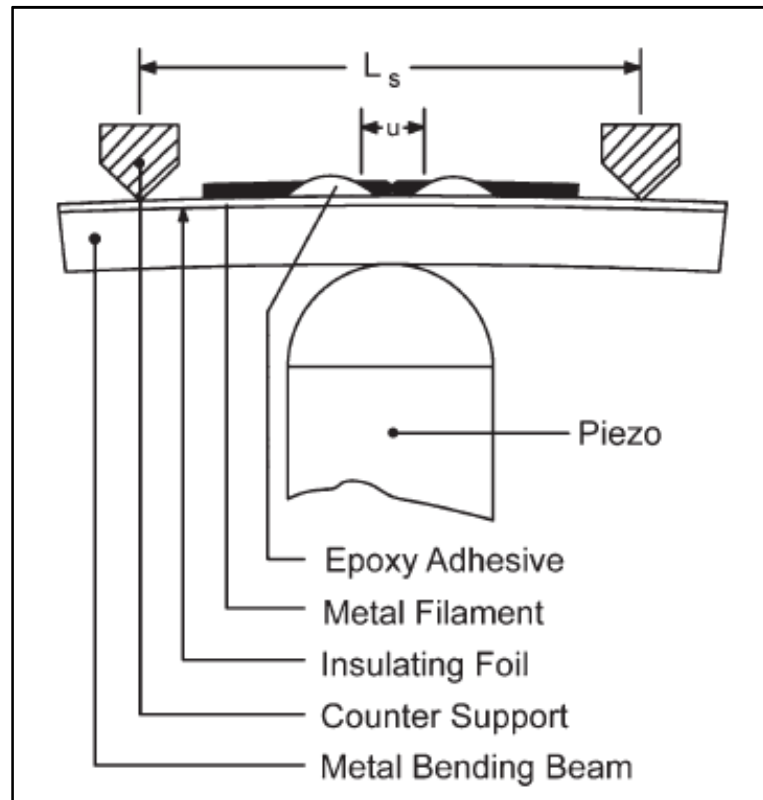


Figure 3.3: The working principle of mechanically controllable break junction using three-point bending mechanism is illustrated³⁸.

MCBJ method is very useful for studying the electronic behavior of nanostructures and exploring the characteristic of atomic point contact and tunnel junctions such as quantum conductance and tunneling current. However, this method is not compatible with integrated micro/nano devices because of the bulky bending mechanism made of delicate piezo materials.

3.2.3 Other Methods and Conclusion

Electromigration and MCBJ are based on the breaking of a metal constriction. On the other hand, nanogaps can also be formed by filling wider gaps using a deposition technique such as chemical electrodeposition¹⁰⁷⁻¹¹¹, e-beam deposition¹¹², electroplating^{113,114}, focused ion beam deposition¹¹⁶, atomic layer deposition¹¹⁸⁻¹¹⁹ and thermal evaporation¹²⁰. As mentioned before, even the advanced lithography techniques like e-beam and focused ion beam lithography can consistently define gap widths around 10 nm at best. In order to obtain nanogaps, these lithographically defined wider gaps must be narrowed down by further depositing material to the very ends of the tips. The crucial point is to control gap width during deposition and to be able to cease the deposition as soon as the gap size is reduced to a desired value. However, such a control mechanism is not available in all of the mentioned deposition methods. Some of them are combined with another technique such as electromigration or MCBJ to sustain the control over the fabrication process^{110,113} while some other are contended with statistical results and low yield¹²⁰.

Chemical electrodeposition/dissolution technique is performed in a solution and the size of the nanogap can be reversibly narrowed or widened by either depositing atoms to the electrodes or etching atoms from the junction. Meanwhile the gap size can be in-situ monitored and controlled with a feedback mechanism as shown in Figure 3.4¹⁰⁷. The main disadvantage of this technique is that the device has to be immersed in a conducting solution which may not be desired in many applications. Another interesting method is developed by Gupta and Willis using atomic layer deposition, ALD and in-situ control mechanism^{118, 119}. This technique utilizes the prominent features of ALD such as slow, controllable deposition and formation of smooth, clean surfaces. However, this technique requires a dedicated ALD system and only nanogaps made of copper are demonstrated which are oxidized when they are exposed to air.

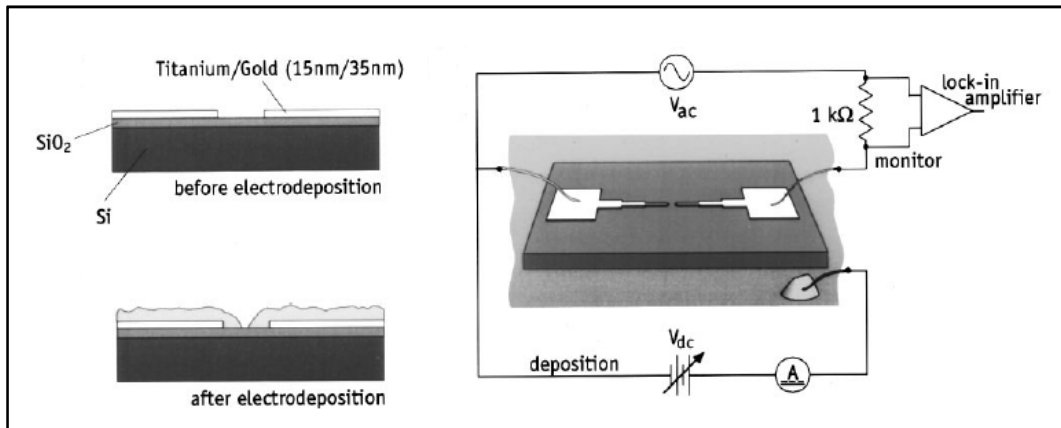


Figure 3.4: The schematic illustrated the working principle of chemical electrodeposition technique used for the fabrication of nanogaps¹⁰⁷.

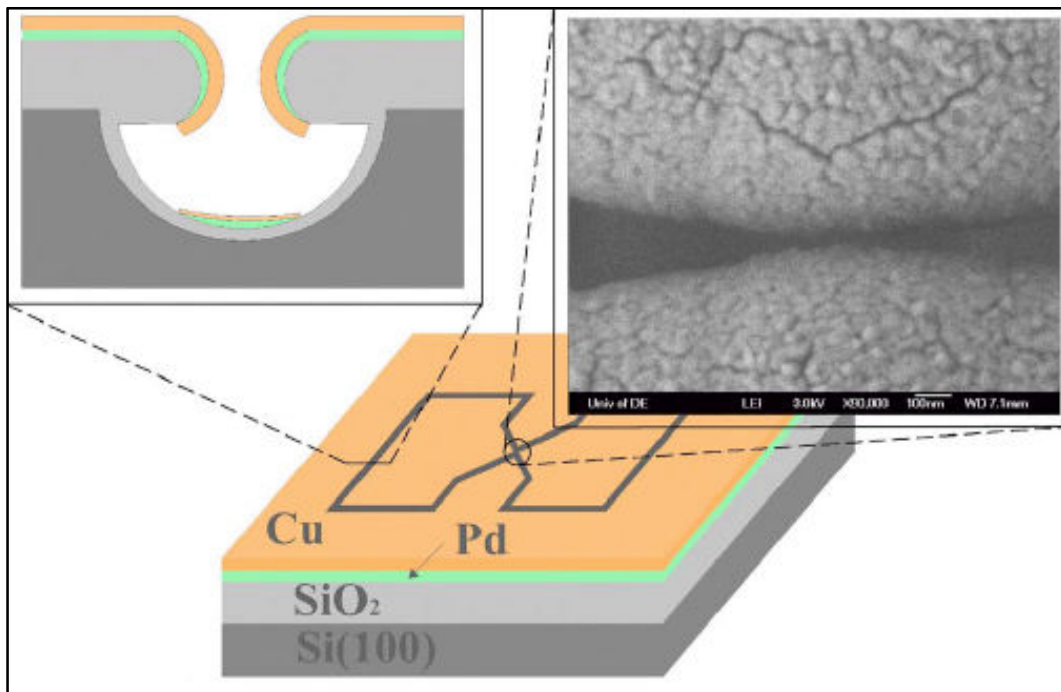


Figure 3.5: The schematic view and the SEM image of a nanogap fabricated by atomic layer deposition are shown¹¹⁸.

When the context of this thesis is taken into account, the most remarkable study from literature is the nanogap fabrication using thermal evaporation¹²⁰. In this work, a batch of metal electrodes with an undercut are defined on a silicon oxide substrate using e-beam lithography and isotropic etching. A second thermal coating is performed for a predetermined thickness to shrink the originally wide gaps. The distance between the metal electrodes are inspected using SEM after deposition. The gap sizes around one nanometer are chosen for electrical characterization. The method is demonstrated only for gold but there is no material constraint as long as it can be thermally evaporated. On

the other hand, the fabrication yield is very low for this technique since there is no in-situ monitoring or a feedback mechanism during thermal evaporation. It is reported that 4 out of 10 devices are short-circuited after deposition and the other 6 devices have gap sizes ranging from sub-nm to 5 nm¹²⁰. Consequently, this method embraces a statistical approach with random results rather than presenting a well-controlled fabrication process.

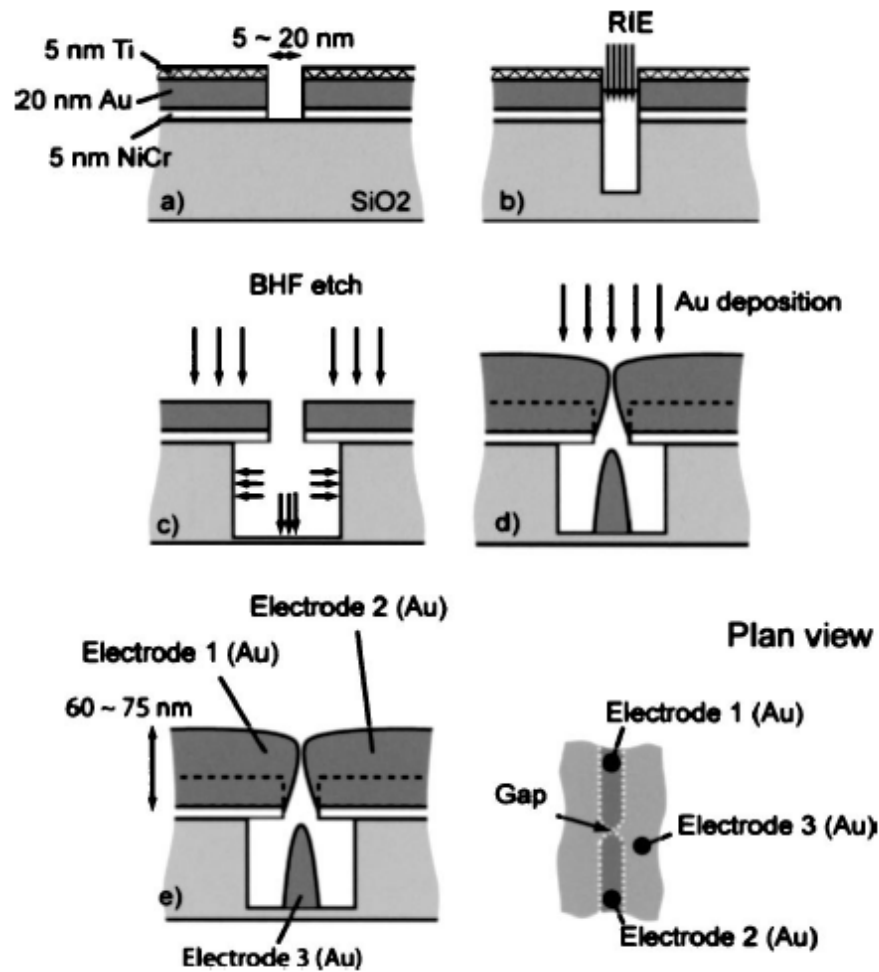


Figure 3.6: The fabrication steps of nanogap formation using thermal evaporation are illustrated¹²⁰.

In summary, although all of these methods successfully produce nanogaps, they either suffer from low yield or material constraints or have fabrication setups that are not compatible with NEMS applications. Therefore, there is still a great need for a well-controlled fabrication technique for the realization of clean nanogaps at a predetermined size.

3.3 Characterization of VTJ / Nanogaps: Simmons' Model

The resolution of the conventional imaging techniques such as SEM is not enough for the direct measurement of gap sizes smaller than few nanometers. Some advanced imaging techniques with higher resolution such as atomic force and transmission electron microscope have been used to measure the nanogaps in a very limited number of applications^{99, 117}. The most common method used to characterize the nanogaps is the electrical measurements. The size of a nanogap can be determined by fitting the current-voltage characteristics of the device to a theoretical model. The most well-known theoretical model in literature was formulated by Simmons in 1963⁴⁷. This model has also been used for the characterization of nanogaps fabricated for this thesis.

The Simmons' model derives formulae for the current flow through a rectangular potential barrier. The current density-voltage relations are formulated for three ranges: low voltage, intermediate voltage and high voltage (Figure 3.7). In this figure, μ_L and μ_R are the chemical potentials for the left and right electrodes, s (\AA) and ϕ (eV) are the thickness and height of the potential barrier and V is the applied bias. The formulae are presented in practical units for each voltage range and they can easily be applied to real life experimental results.

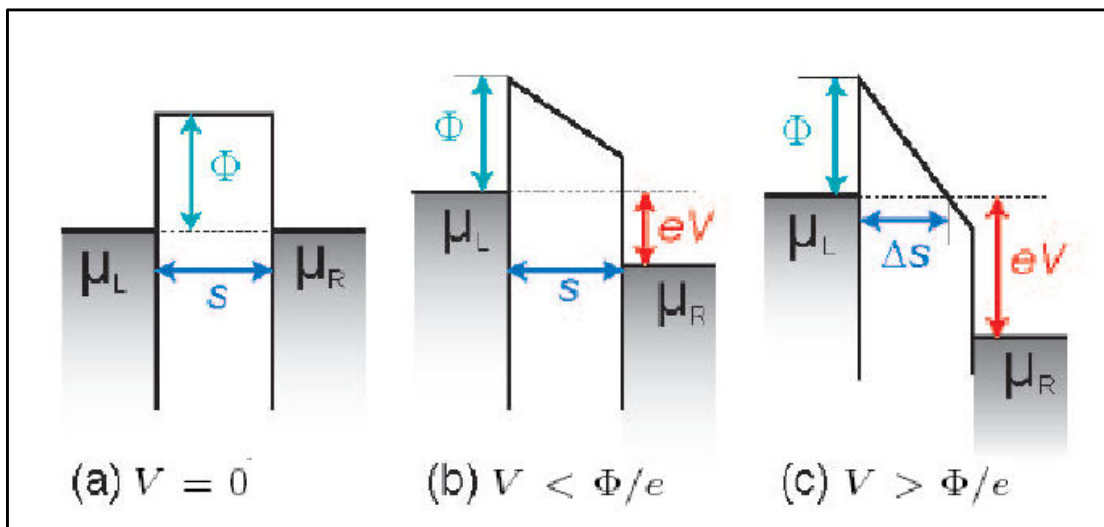


Figure 3.7: The illustrations of a rectangular barrier between two metal electrodes are given for low, intermediate and high voltage ranges⁴⁷.

1. Low-voltage range ($V \approx 0$) : When the applied bias is closed to zero, the current density, J (Ampere/cm²) changes linearly with voltage, V (Volts).

$$J = \left\{ 4.73 \times 10^{10} \left(\frac{\sqrt{\phi}}{s} \right) \exp(-1.024s\sqrt{\phi}) \right\} \times V . \quad (3.3)$$

2. Intermediate-voltage range ($V < \phi/e$) : For the applied biases smaller than the potential barrier height, there is a complex nonlinear relationship between the current density and voltage as given in Equation 3.4. The first term in the curly bracket corresponds to the electron tunneling from left electrode to the right electrode and the other way around for the second term. This region corresponds to the tunneling regime and the fabricated tunnel junctions are generally operated and measured in this region.

$$J = \left(\frac{6.16 \times 10^{10}}{s^2} \right) \times \left\{ \begin{array}{l} \left(\phi - \frac{eV}{2} \right) \exp\left(-1.024s\sqrt{\phi - \frac{eV}{2}}\right) \\ - \left(\phi + \frac{eV}{2} \right) \exp\left(-1.024s\sqrt{\phi + \frac{eV}{2}}\right) \end{array} \right\} . \quad (3.4)$$

3. High-voltage range ($V > \phi/e$) : The tunnel junction enters field emission regime for applied biases higher than the height of the potential barrier. Such high voltages are avoided during the characterization of tunnel junctions because the atomic arrangement is modified at the very end of the metal electrodes under large electric field.

The tunneling current can be calculated by multiplying the current density with the tunneling area. There are three parameters to be interrogated; area A (cm²), potential barrier height ϕ (eV) and gap width s (Å), when the measured current-voltage data of the device is fitted to the Simmons' equation for intermediate range. On the other hand in real applications the area is fixed to the cross section of a single atom to avoid large errors in fitting^{41, 120}. The details on the application of Simmons' model to experimental results will be further discussed in Chapter 5.

3.4 VTJ as a Displacement Sensor

The tunneling current exponentially depends on the barrier thickness, in other words the distance between the metal electrodes, as given in Equation 3.1. When one of the metal tips is placed on a mechanical resonator, the tunneling current between the fixed metal tip and the resonator changes dramatically as the resonator oscillates. In theory, the displacement of the resonator can be deduced by measuring the tunneling current. The idea of using a VTJ as a displacement sensor was first proposed by the gravitational wave-antenna community for the detection of very weak gravitational forces that act upon a gravitational wave-antenna^{23-30, 123}. Here, the antenna is the mechanical resonator and a VTJ is formed by placing a metal tip within one nanometer proximity of resonator's mid-point (Figure 3.8). When a bias of V_0 is applied between the metal tip and the resonator that are separated by distance d , a tunneling current of I_0 flows across the tunnel junction. In this representation, I_0 is the nominal value which equals to the tunneling current when the resonator is not moving and the width of the tunnel junction is fixed to d .

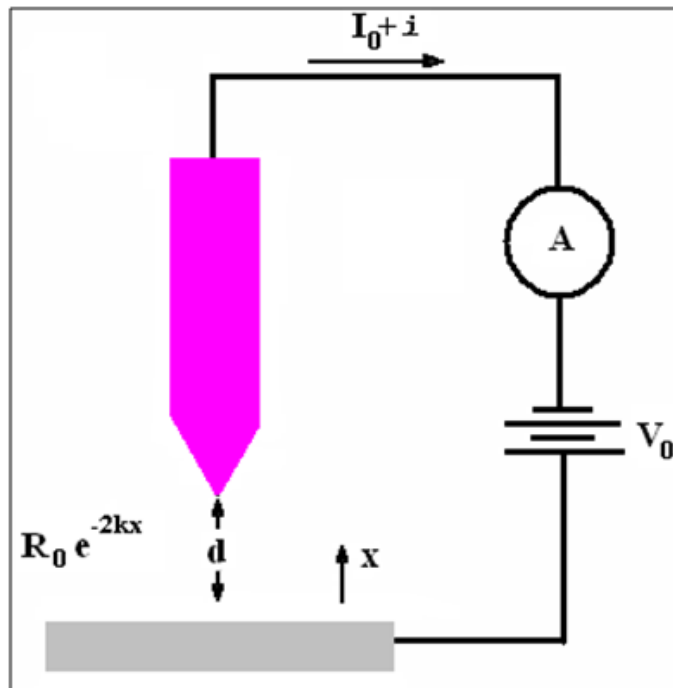


Figure 3.8: The schematic illustrates the working principle of VTJ displacement detector²⁷.

When the resonator moves, the gap width and hence the tunneling current change accordingly. The relation between the tunneling current and the displacement of the resonator, x is given by:

$$I = I_0 \exp(2\kappa x) , \quad (3.5)$$

where $\kappa = \sqrt{2m_e\phi/\hbar}$. Here m_e is mass of the electron, ϕ is the work function of the metal assuming that the gap is absolute vacuum and \hbar is the Planck's constant. The VTJ can be modeled as a resonator under a bias of V_0 :

$$R = (V_0/I) = R_0 \exp(-2kx) . \quad (3.6)$$

Here, $R_0=V_0/I_0$ represents the nominal resistance of the VTJ. The typical values for the nominal current and nominal resistance are on the order of nano-Amperes and hundreds of mega- to giga-Ohms for $d=1$ nm²⁵⁻²⁷.

3.4.1 Theoretical Aspects

The theoretical calculations performed by gravitational wave community suggest that the displacement imprecision of a tunnel junction detector is determined by two factors: shot noise and back-action^{23-30, 123}. The shot noise is the intrinsic current fluctuations as a result of the discrete nature of electron charges. Shot noise is intrinsically a quantum mechanical phenomenon and for quantum-ideal position detection it should not be overcome by other types of noises such as the noise from the following amplifiers^{25, 26}. The back-action is the force that the detector exerts on the resonator and it is caused by the momentum kicks of tunneling electrons²⁸ and it has been shown that, the main advantage of the tunnel junction detectors over capacitive detectors is the reduced back-action force^{25, 26}. The theoretical calculations for both factors are shown to be quantum-ideal by these early studies^{23-30, 123}. Even though the calculations are carried out in the context of bulk antennas, it is concluded that the maximum sensitivity is obtained for small mechanical oscillator masses²⁶. The recent technical advances in NEMS have promoted the theoretical interest in vacuum tunnel

junctions in the context of quantum-limited displacement detection in mesoscopic structures^{8, 10, 31-37, 124}. These calculations also suggest that tunnel junction displacement detector can be capable of reaching the quantum limit of a nanomechanical resonator.

3.4.2 Experimental Aspects

The theoretical studies confirm that the noise of a tunnel junction displacement detector is quantum-limited and it is possible to perform quantum measurements on mesoscopic systems using this detector. Nonetheless, there are serious technical and engineering problems with the realization of such a system. First of all, the fabrication of a tunnel junction-nanoresonator embedded device is a challenging task. We already know that the distance between the metal tip and the resonator should be on the order of one nanometer to be able to operate in the tunneling regime with the optimum coupling constant. In STM, the metal tip is approached to the sample surface until a tunnel junction is formed by using a bulk, slow and delicate mechanism. However, such an approaching mechanism cannot be used in NEMS applications where the measurements are fast and the dimensions are small. Therefore, the metal tip and the nanoresonator must be in-situ fabricated and have a minimal mechanical loop to form a stable tunnel junction in between.

As mentioned before, there are many different techniques for the fabrication of nanogaps but they either suffer from material constraints or use bulk mechanism or fail to control the final gap size. Recently an atomic point contact displacement detector has been implemented by Flowers-Jacobs *et. al.*¹⁸. In this experiment, the atomic point contact is fabricated using electromigration. As a result of the requirements of the fabrication method the beam and the metal tip are made entirely out of gold which results in the deterioration of the resonance frequency and quality factor. The resistance of atomic point contact (33 k Ω) is very low compared to typical tunnel junctions formed by STM¹⁸. The resistance of the tunnel junction determines the coupling strength of the detector which must be optimized and well-controlled for maximum sensitivity. However, electromigration is a self-terminating process and the control over final gap size is limited. Last but not least, even though it is performed in cryogenic temperatures and ultrahigh vacuum, the cleanness and chemical purity of the gap is not guaranteed in

electromigration. The author comments that the experimental results might have been significantly affected by the contaminants in the gap. Therefore, a fabrication method that can produce clean tunnel junctions at a predetermined size must be developed and employed. The method should be capable of using stiff materials like silicon nitride or silicon carbide to obtain higher resonance frequencies. Finally, it should not contain any bulk or delicate approaching mechanisms that are not compatible with NEMS applications.

The other technical problem with the realization of tunnel junction detector is the operating speed. In fact the tunneling process is inherently fast since it is a quantum mechanical phenomenon. The fundamental limit on the speed of a tunneling measurement is given by the number of tunneling electrons per unit time, I/e . This limit entails an operation bandwidth of 1 GHz for a tunneling current of 1 nA due to shot noise⁷⁷. However, this intrinsic high speed of quantum tunneling is dropped off dramatically in real life applications. The typical impedance values of tunnel junctions are very high ranging from mega- to giga-Ohms and there are unavoidable parasitic capacitances on the order of pico-Farad originating from bonding pads and following microscopic wiring and electronic components. The parasitic capacitance parallel to the high impedance reduces the operation bandwidth to $1/2\pi RC \approx 1-10$ kHz. The experimental bandwidth of a tunnel junction detector can be increased by using the reflectometry technique which is originally developed to increase the speed of a single electron transistor¹⁴.

Kemiktarak *et. al.* managed to increase the bandwidth of an STM to 10 MHz which allows a 100 times faster surface topography imaging compared to a conventional STM⁷⁷. Using this radio-frequency STM, they also performed displacement measurement on a micromechanical membrane with a sensitivity of ~ 15 fm Hz^{-1/2}⁷⁷. In another experimental work, Flowers-Jacobs *et. al.* achieved to characterize a nanobeam with a resonance frequency of 60 MHz using reflectometry technique¹⁸. In this technique, the high impedance of the tunnel junction (M Ω -G Ω) is matched down to the characteristic impedance of coaxial cables (50 Ω or 75 Ω) using an LC transformer. In Figure 3.9, R_t represents the impedance of the tunnel junction. The inductance and capacitance values of the following L-shape matching circuit are chosen such that the output impedance of the R_t LC circuit is equal to the characteristic

impedance of the coaxial cable. When a microwave signal (carrying signal) is sent to the tunnel junction, there will be no reflection if the impedances of the coaxial cable and the R_tLC circuit are perfectly matched. However, the resistance of the tunnel junction changes as the nanobeam oscillates and hence, a mismatch occurs in the resonant circuit. Consequently, some of the incident wave will be reflected depending on the amount of mismatch. The resonance frequency and the quality factor of the nanobeam and the noise properties of the tunnel junction detector can be determined by measuring the reflected wave. The frequency of the carrying signal also depends on the choice of L and C values used in the tank circuit.

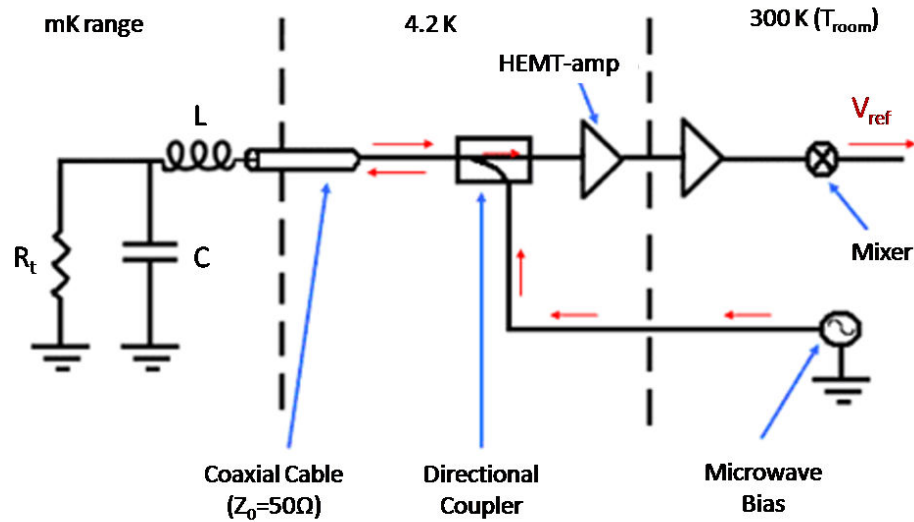


Figure 3.9: The schematic illustrates the reflectometry technique used to increase the operation bandwidth of a tunnel junction⁷⁷.

All in all, experiments show that the operation bandwidth of a tunnel junction detector can be increased using reflectometry technique. However, the main obstacle for the realization of tunnel junction-nanobeam embedded system is the absence of a high-yield, well-controlled fabrication method which satisfy the requirements of NEMS applications. In this thesis, we proposed and implemented a nanogap fabrication method which will hopefully fulfill this need.

CHAPTER 4

NANOFABRICATION

4.1 Introduction

Fabrication of extremely small devices from a wafer requires high technology facilities and equipments. This kind of technology is mainly developed for the fabrication of integrated circuits but it also forms the basis for more state-of-art applications like electromechanical devices. The devices fabricated during this thesis are at nanometer scale and hence, in addition to the micron-scale technologies of integrated circuits, more advanced techniques like electron beam lithography (EBL) is required. Formation of tunnel junction/nanogap is not possible even with EBL and special, unique and novel methods beyond the standard micro/nano fabrication techniques have to be developed for this purpose. This technique will be discussed in the next chapter.

This chapter explains the nanofabrication methods employed, the recipes formulated, and the process flows developed during this thesis. The process flow for device fabrication has been modified and improved many times in accordance with the problems faced and the solutions found for those problems. The device fabrication is mainly performed in faculty clean room and scanning electron microscope facilities and Nanotechnology Research and Application Center located at Sabancı University. The devices are patterned using various nano/micro fabrication techniques like electron beam lithography, photolithography, dry etch, wet etch, thermal metal coating etc.

4.2 Fabrication Methods

4.2.1 Wafer Preparation and Standard Cleaning

The wafer used in this work is 4-inch Si (100) at the bottom, 1 μm thermally grown SiO_2 in the middle and 100 nm LPCVD grown Si_3N_4 at the top (NOVA Electronic Materials). The tensile stress of the Si_3N_4 layer is 800 MPa. The wafers are cut into 2x2 cm squares with a diamond scribe. The standard cleaning starts with 5 minute ultrasonic ACE and then the samples are rinsed consecutively in three ACE and three IPA beakers for 30 seconds. The samples are flashed with either ACE or IPA during the transfer from one beaker to the other. When the samples are removed from the last IPA beaker, they are blow-dried using N_2 gun and baked on hotplate at 120° C for 5 minutes for dehydration.

4.2.2 Electron Beam Lithography (EBL)

4.2.2.1 Introduction to EBL

EBL is a widely used fabrication technique where sub-micrometer resolution is desired. In this method, the sample is uniformly covered with a thin layer of chemical called “resist”. The chemical structure of the resist changes when it is exposed to electrons. If it is a positive resist, the region that is exposed to electrons becomes soluble in a special solution called as “developer”. If it is a negative resist, the unexposed regions are soluble and the exposed regions become insoluble in the developer. After development, the patterned resist can serve as an etch mask or can be used for lift-off processes.

The primary resist used in this thesis is Polymethyl-methacrylate (PMMA). PMMA is a positive resist and commercially available in different solvents, at different concentrations and molecular weights. The molecular weight determines the sensitivity and resolution of the process. Higher molecular weight means smaller molecular chain scissions during lithography. PMMA with higher molecular weight is less sensitive to the electrons which mean the development rate is slower and the resolution is better compared to the low molecular weight PMMA. On the other hand, for coarse

applications low molecular weight PMMA is preferred since the required exposure dose is less and hence the exposure time is shorter for sensitive resists. PMMA can be dissolved in different solvents like anisole, chlorobenzene, and Methyl isobutyl ketone (MIBK). The viscosity of the resist changes with concentration. The thickness of the coated-resist depends on the concentration and the spin-speed. Thickness versus spin-speed curves for different concentrations and different solvents are generally provided by the manufacturer. Most of the solvent evaporated during spinning but still the coated sample should be baked either on hot-plate or in oven at a certain temperature to get rid of the remaining solvent and to cure the resist before exposure.

After resist coating and baking, the next step in EBL is to expose the resist using a focused electron beam. For this purpose either a dedicated system or a modified conventional scanning electron microscope (SEM) can be used. In SEM, the electrons extracted from the source (gun), are accelerated and focused through a column using electrical and magnetic coils. The amount of the current, the energy of the electrons and the size of the beam that reaches the sample surface can be controlled by changing the SEM parameters like aperture size, accelerating voltage, working distance. The ultimate resolution of the lithography depends on the beam spot size. Therefore the image resolution should be optimized carefully before the pattern writing, by performing focusing, stigmation, and gun and aperture alignment. Once the beam is optimized, a hardware controller directly writes the designed pattern on the sample by deflecting the scan coils which controls the position of the beam. This step is called as “exposure”. During exposure, the electrons that are incident on the sample interact with resist and sample through elastic and inelastic scatterings. The interaction volume, shape, and depth depend on the chemical composition and surface topography of the resist and sample, and the energy of the incident electrons. The interaction volume refers to the regions that are exposed by electrons and these regions will be removed after development. The pear-shaped interaction volume naturally leads to a negative profile after development which is beneficial for lift-off processes.

Following the exposure, the samples are put in a solution called “developer”. For positive resists like PMMA, the developer dissolves the exposed regions. Therefore, only unexposed resist regions remain on the wafer after the development. MIBK is the most widely used developer of PMMA. The development rate of pure MIBK is very

fast and it is hard to control the development time. Therefore, for better control and higher resolution, mixtures of MIBK and IPA are used. Some other development methods have been introduced in literature like cold development with MIBK¹²⁵ and water-IPA ultrasonic development^{126, 127}. These methods claim higher resolution for certain applications compared to standard room temperature MIBK/IPA mixture.

4.2.2.2 EBL at Sabanci University

The SEM at Sabancı University is a Zeiss Leo Supra 35VP field emission microscope. It is equipped with Gemini Column technology and the electron source is a Schottky field emission gun. SEM is a tool designed to provide ultra high resolution imaging by raster scanning a highly focused electron beam across the sample. On the other hand, the movement of the electron beam has to be directly controlled for patterning. For this purpose, Nabity Pattern Generation System (NPGS) has been purchased and installed on the existing SEM to be able to use it as a patterning tool as well. NPGS is an external computer and it allows the user to control the movement of the electron beam through a digital to analog converter (DAC). The software also allows the user to control the SEM parameters that are crucial for EBL like aperture size, magnification, beam step size, and beam dwell time. The system can also transmit necessary parameters from the SEM to the control computer through an analog to digital converter (ADC) like beam current, working distance, stage coordinates.

The basic operation steps of the NPGS system can be given as:

1. Gold plated sample holders are specifically designed and machined for EBL applications by our research group. To collect and measure the beam current, there is a Faraday cup on the sample holder which is a 1 mm diameter and 2 mm deep hole painted with carbon. Before placing the sample in the SEM, four corners are scratched with a diamond scribe. These scratches will be used for plane correction of the sample before exposure. Then the sample placed on the holder with a single. A single, soft clamp is preferred other than two to avoid bending of the sample. The sample holder is placed on the SEM holder and the chamber is evacuated.

2. The SEM stage is lifted up until the distance between the sample and the gun (working distance) is approximately 5-6 mm. When the vacuum is ready, the gun is energized. The aperture size and the extra high tension (EHT) voltage are adjusted in the beginning of the process before any SEM adjustments. The aperture size determines the amount of the beam current and hence affects the minimum spot size of the beam. For high resolution applications on small writing fields (<100 μm) small aperture sizes, i.e. low beam currents, are preferred. Our SEM has six different aperture sizes: 7.5-10-20-30-60-120 μm . While the standard imaging aperture is 30 μm , 10 μm -aperture is mostly used for fine patterning EBL applications. EHT voltage determines the penetration depth of the electron beam into the substrate which ultimately affects the shape of the interaction volume and hence the sidewall profile of the resist. The choice of EHT voltage depends on the process type and resists thickness.
3. Once the aperture size and EHT voltage are set, the SEM parameters like working distance (focus), aperture alignment and stigmation should be adjusted. The adjustments should be repeated until a high resolution image at high magnifications like x500k is obtained.
4. When all the SEM adjustments are done, the beam current is measured by pointing the beam into the faraday cup on the sample holder. The typical beam current for 10 μm aperture ranges between 10-30 pA depending on the EHT voltage and the condition and age of the electron source.
5. Since the surface of the sample is usually not perfectly flat, the optimum working distance changes over the sample surface. A 4-point plane correction is performed to automatically adjust the working distance during pattern writing. For this purpose, the focus adjustment is done on four corners and the NPGS software records the position and working distance of each corner. Using these data, it performs a plane correction and it automatically corrects the working distance when the stage moves to a new position.

6. When SEM adjustments are completed, the pattern should be prepared. NPGS uses a drawing program called DesignCAD. The user can design the alignment and writing patterns using this program. When the pattern is ready, the writing conditions should be specified using “run file editor” of NPGS. In this run file editor, the user uploads the alignment and writing CAD files and enters the magnification, step size, beam current, aperture size, and exposure dose. Once the run file editor is ready the exposure will be performed automatically by NPGS. When the writing is completed, the gun is turned off and the SEM is vented to take off the sample.

EBL process is completed when the samples are developed after the exposure. The installation and calibration of the NPGS system and process optimization for different EBL applications are performed by our research group. Mainly two processes, monolayer and bilayer, are developed during this thesis using PMMA and both of them are for lift-off applications.

MONOLAYER PROCESS:

1. PMMA COATING: The sample is spin-coated in the clean room with high resolution 950K MW PMMA-C2. PMMA is dripped on the sample using a glass pipette, and then the sample is spun at 500 rpm for 3 seconds and at 6000 rpm for 45 seconds. The uniformity of the resist thickness is critical to be able to obtain the same resolution everywhere on the sample. Therefore the surface of the sample should be free of dirt and dust before coating. Additionally, for better adhesion of the resist to the sample surface, dehydration bake should be performed before spin coating. The thickness of the 950K MW PMMA-C2 at 6000 rpm is approximately 100 nm.
2. PREBAKE: The sample should be baked on hotplate at 180° C for 1 hour.
3. EBL: In monolayer process, lower EHT voltages are preferred so that, in addition to the primary beam, the back-scattered electrons can also dose the lower parts of the resist. In this case, the interaction volume gets wider from the surface of the resist towards the resist-sample interface and leads to a negative

profile after development. The EHT voltage, working distance, and aperture size for monolayer process are 15 kV, 5-6 mm, and 10 μm , respectively. The exposure dose depends on the pattern size and pattern density. Therefore, before the fabrication of real samples, the optimum dose is determined by performing a dose array for each different pattern.

4. DEVELOPMENT: 1:3 MIBK:IPA solution is used for the development of PMMA. The development time depends on the resist thickness and exposure dose. For 100 nm thick PMMA, the development time is 40 seconds for the optimum exposure dose. The development is generally followed by a dip or rinse in pure IPA and then N_2 blow dry. On the other hand some recent studies suggest that if the samples are directly N_2 blow dried without any IPA dip/rinse, the line edge roughness will be reduced ¹²⁸. We also compared two methods and observe that after metallization, the edges of the samples without IPA rinse are smoother. As a result, we have abandoned the IPA dip/rinse step during development. Figure 4.1 illustrates the monolayer EBL process and Figure 4.2 shows the SEM images of metal tips fabricated with monolayer process and the alignment accuracy of the EBL system. It is possible to fabricate two metals tips with a sub-10 nm gap in between and the alignment accuracy of the system is sub- μm .

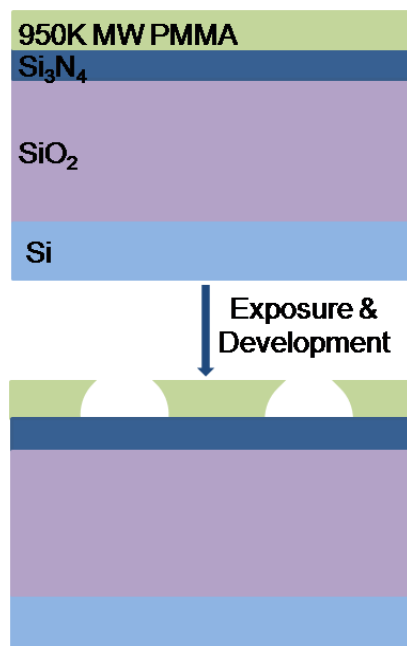


Figure 4.1: The illustration shows the EBL process using monolayer PMMA.

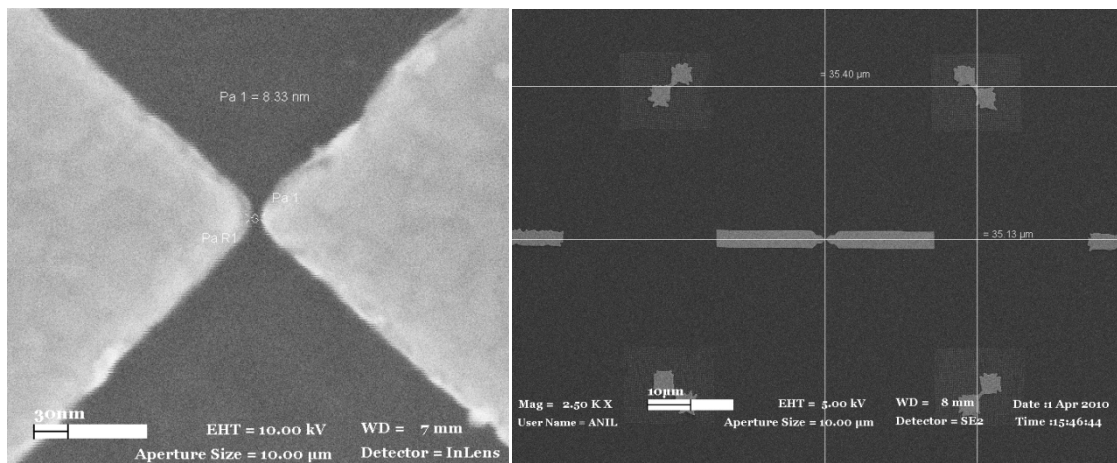


Figure 4.2: The SEM images of metal tips fabricated with monolayer process and the alignment accuracy of the EBL system are given. These images show that a sub-10 nm gap between two metal tips can be patterned using monolayer process and the alignment accuracy of the system is on the order of sub- μm .

BILAYER PROCESS:

Even though monolayer process yield good results most of the time, for densely packed, close and small structures it may fail due to proximity effect. For this kind of patterns, lift-off applications using bilayer process are more successful. There are two advantages of bilayer process. First, the proximity effect is reduced by decreasing the number of backscattered electrons by using high EHT voltage. Second, the undercut is more pronounced since a more sensitive resist is used as bottom layer. The process flow for bilayer process is given as:

1. **PMMA COATING and PREBAKE:** The sample is first spin-coated with high sensitivity 495K MW PMMA-C2 (500 rpm for 3 seconds and at 6000 rpm for 45 seconds). The sample is baked on hotplate at 180° C for 1 hour. For the top layer, 950K MW PMMA-A2 is used. In order to avoid the intermixing of two layers, the sample is spun at 100 rpm while dripping the second layer and then at 6000 rpm for 45 seconds. The sample is once again baked on hotplate at 180° C for 1 hour after coating of the second layer. The thicknesses of the 495K MW PMMA-C2 and 950K MW PMMA-A2 at 6000 rpm are approximately 130 nm and 60 nm respectively.

2. EBL: As stated before, to reduce the proximity effect, high EHT voltages are preferred. The interaction volume is fairly straight through the resist layers but there is an undercut after development because of the difference in the sensitivity of the resists. The EHT voltage, working distance, and aperture size for monolayer process are 30 kV, 5-6 mm, and 10 μm respectively. The exposure dose depends on the pattern size and pattern density.
3. DEVELOPMENT: The samples are developed in 1:3 MIBK:IPA solution for 40 seconds and directly N_2 blow dried without any IPA dip/rinse. In a number of patterns that include small openings inside the structures, there have been serious lift-off problems with standard development using MIBK/IPA. For those specific patterns, development is performed in ultrasonic bath of 7:3 IPA:deionized water for 10 seconds. Figure 4.3 illustrates the bilayer EBL process and Figure 4.4 shows the SEM images of the structures fabricated using MIBK:IPA and IPA:deionized water development.

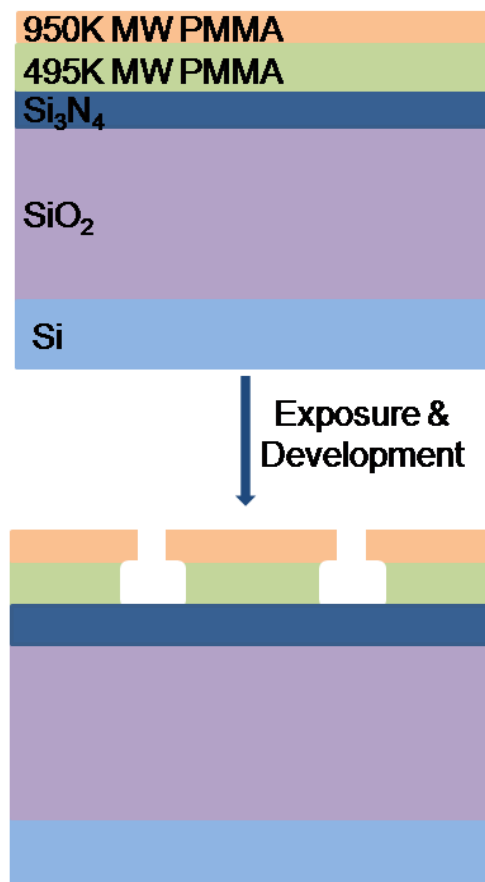


Figure 4.3: The illustration shows the EBL process using bilayer PMMA.

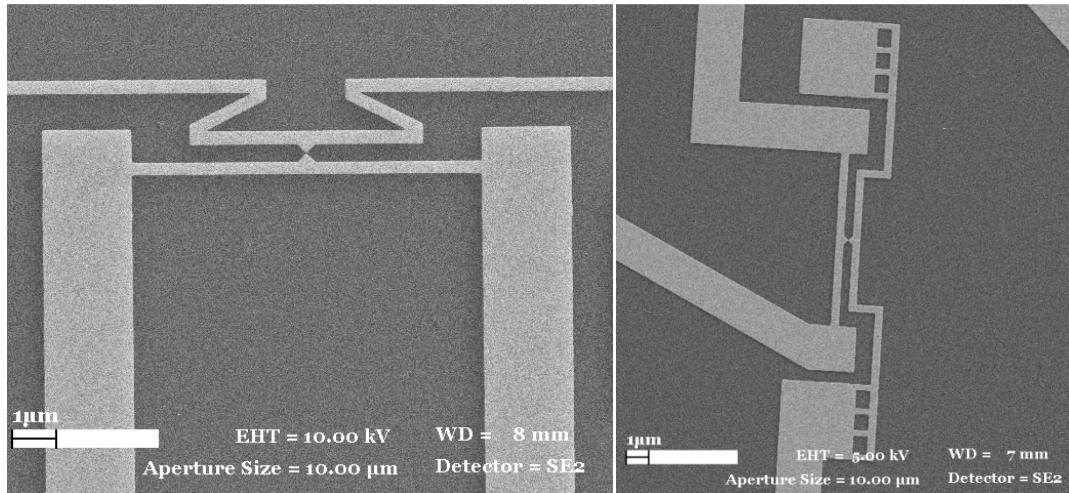


Figure 4.4: SEM images of the structures fabricated using MIBK:IPA (left) and IPA:deionized water (right) development are given. Ultrasonic IPA:deionized water development is preferred for more complicated structures with small openings as shown on the right SEM image.

4.2.3 Photolithography

Photolithography is a widely used method for the fabrication of micron size structures. The resolution of EBL is almost two orders of magnitude better than the resolution of the photolithography. On the other hand, EBL is a time consuming process compared to photolithography because it is based on the direct writing of the pattern. Therefore, EBL is preferred only for the critical structures that require sub-micron resolution while photolithography is preferred for less critical, large area, micron size structures. In photolithography, the sample is spin-coated with a special polymer called “photoresist” which is sensitive to ultraviolet light. Then the sample is illuminated through a pre-patterned mask which has opaque and transparent parts on it. The light goes through the transparent parts of the mask and exposes the photoresist while the regions under opaque parts stay unilluminated. If a positive photoresist is used, the illuminated parts become dissolvable in the developer and the unilluminated parts remain on the sample and if it is a negative photoresist, vice versa.

The photolithography processes are carried at Sabancı University clean room using Karl-Süss MA6 Mask Aligner. The power of the ultraviolet light is 1.8 mW/cm^2 . The chrome on quartz masks are designed using AutoCAD and produced by ML&C GmbH. An image reversal photoresist AZ5214E and its developer AZ726MIF are used for both negative and positive lithography applications (Microchemicals GmbH).

Positive lithography is mainly used for wet and chemical etch mask applications and negative lithography is used for lift-off applications.

The most critical point while performing photolithography is that the sample and the mask should be in contact without any gap during exposure. Otherwise, the light diffracts from the edges of the chrome and deteriorates the resolution. For this purpose the sample and the mask holders of the aligner are calibrated to maintain a full contact. Also the resist residues on the mask are cleaned in every use and the edge beads of the coated samples are scratched before exposure for the same purpose. The process recipes developed by our research group have yielded a resolution of 3-5 μm .

POSITIVE PROCESS:

1. SPIN-COATING: The sample is first spin-coated with AZ5214E (1000 rpm for 2 seconds and at 6000 rpm for 45 seconds).
2. PREBAKE: The sample is baked on hotplate at 100° C for 2 minutes. The thickness of the resist is 1.4 μm .
3. MASK EXPOSURE: The sample is illuminated through mask for 120 seconds.
4. DEVELOPMENT: The sample is developed in AZ726MIF for 30 seconds and then rinsed in DI-water and N₂ blow-dried.

NEGATIVE PROCESS:

1. SPIN-COATING: The sample is first spin-coated with AZ5214E (1000 rpm for 2 seconds and at 6000 rpm for 45 seconds).
2. PREBAKE: The sample is baked on hotplate at 90° C for 2 minutes. The thickness of the resist is 1.4 μm .
3. MASK EXPOSURE: The sample is illuminated through mask for 20 seconds.
4. POSTBAKE: The sample is baked on hotplate at 115° C for 2 minutes.
5. FLOOD EXPOSURE: The sample is illuminated without any mask for 180 seconds.
6. DEVELOPMENT: The sample is developed in AZ726MIF for 90 seconds and then rinsed in DI-water and N₂ blow-dried.

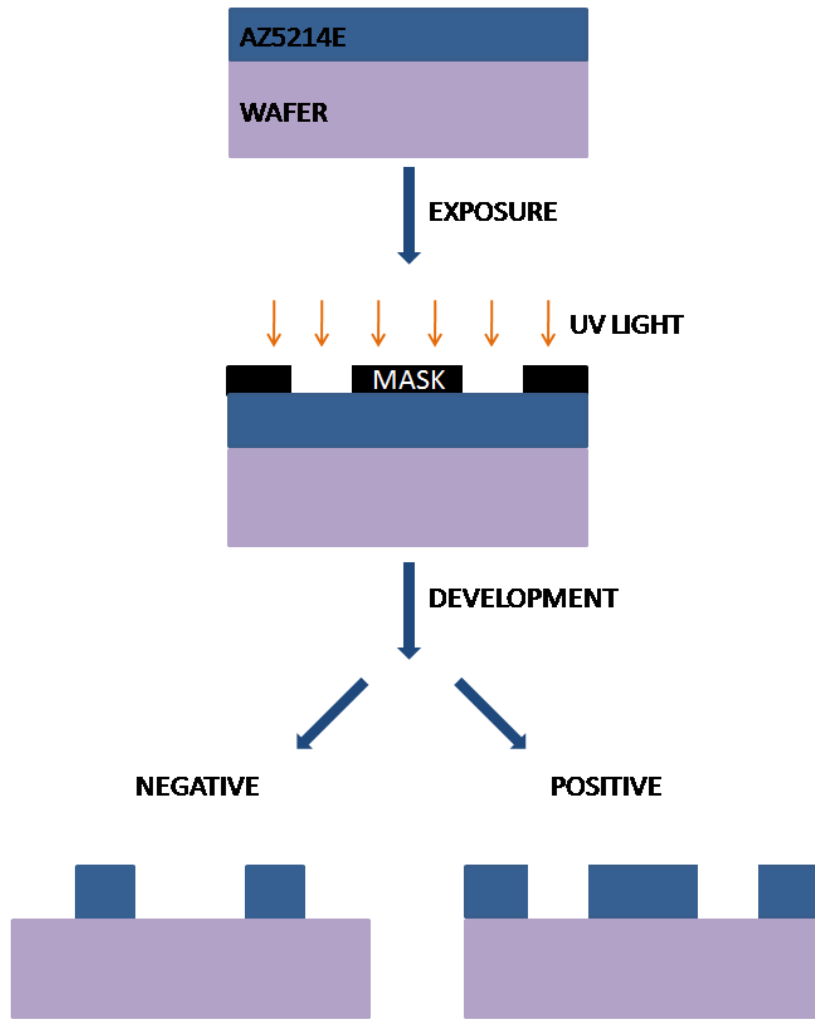


Figure 4.5: The illustration shows both negative and positive photolithography processes.

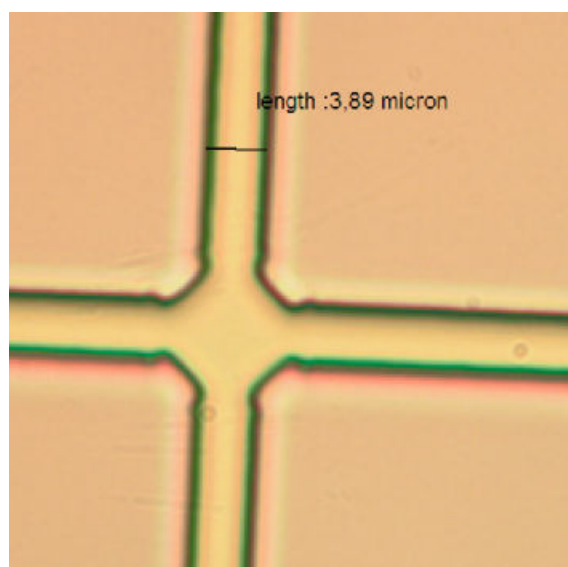


Figure 4.6: The optical microscope image which shows the resolution of the photolithography process developed during this thesis is given.

4.2.4 Metallization and Lift-off

After EBL or photolithography the designed patterned can be transferred to the sample by metal coating. Metal coating is mainly performed by electroplating, electron beam evaporation, or thermal evaporation. A box coater (Nanovak) is used for the thermal coating of metals like chromium, nickel, titanium and gold at Sabanci University. The metal atoms are adhered on wafer surface where the resist is removed after development. When the sample is placed in ACE after evaporation, the resist and the metal on top of it go away but the metal adhered on the wafer remains. This process is called as “lift-off”.

The sidewall profile of the resist is important for successful lift-off results. The sidewalls of the resist should have a negative profile in other words a pronounced undercut. Otherwise the resist sidewalls will also be covered with metal which makes the subsequent lift-off worse or even impossible. Additionally, temperature control during thermal evaporation is crucial. The overheating of the sample effects the lift-off in two ways: First, the profile of the resist sidewall is ruined and second, the resist goes through glass-transition and becomes insoluble in ACE. Therefore, the evaporation is performed in steps by letting the sample to cool down to room temperature in between. The overheating problem is much more critical for PMMA than photoresist.

4.2.5 Dry Etching (ICP-RIE)

In dry etching process, the material is basically removed by ion/atom bombardments. The ions/atoms are formed and accelerated towards the sample in a plasma chamber. The nature of the etching can be physical, chemical or both. The etch rate and the etch profile depends on the ion density in the chamber, momentum of the ions when they hit the sample surface and the chemical composition of the reactive gases and the etched material. These parameters are tuned by controlling the pressure, gas flow, DC bias, forward RF-power and ICP-power of the RIE system. In these experiments dry etching is applied for two purposes: First, for the stripping of the resist residues (ashing) after lithography and second, for the anisotropic etching of the insulating layers like Si_3N_4 and SiO_2 . Almost all of the dry etch processes are carried on DSE PM2000 ICP-RIE system located in the faculty clean room and only a couple of last samples are etched using Oxford PlasmaLab System 100 ICP 300 Deep RIE located

at Sabancı University Nanotechnology Research and Application Center (SUNUM). The recipes used in DSE system have been developed by our research group and the recipe used in Oxford system has been provided by manufacturer.

OXYGEN PLASMA:

Oxygen plasma etching is a chemical process and it successfully etches organic materials like resist residues, from the surface of the sample. After lithography, a very thin layer of resist still remains on the surface in the developed areas. This thin layer of resist residue obstructs the adhesion of the metal film to the wafer. It is observed that, the metal structures easily peel-off during subsequent wet etch or wire bonding steps because of poor adhesion. Therefore, it is important to get rid of the PMMA or photoresist residues before metal coating. Even though there are some chemicals used for stripping, they still leave sub-nanometer or nanometer thick residue on the surface. On the other hand, that oxygen plasma is shown to be able to remove all unexposed residue¹²⁹. The etch time is critical because over-etch can spoil the resist sidewall profile. In addition to resist stripping, oxygen plasma is also used for cleaning of the plasma chamber since etch byproducts stick on chamber walls and affects the subsequent etchings. The oxygen plasma parameters used in this work are 30 sccm O₂ flow, 0.07 mBar pressure, and 100W forward RF-power. The etch time is 5 seconds for PMMA after EBL and 15 seconds for AZ5214E after photolithography. The chamber cleaning process is generally done at least for 5 minutes.

CHF₃ /O₂ PLASMA:

The dry etching recipe using CHF₃/O₂ gas mixture is developed for the anisotropic etching of Si₃N₄. The nanomechanical doubly-clamped beam fabricated in this work is made of Si₃N₄. Therefore, 100 nm thick nitride layer has to be etched vertically using a thin, gold etch mask. The only fluoride based gas at Sabancı University clean room was sulfur hexafluoride (SF₆) but the processes using this gas or its mixture with oxygen etched the nitride layer isotropically and sputtered the gold mask which resulted in unwanted short-circuits on the device. The results of SF₆ etching using DSE system is given in Figure 4.7.

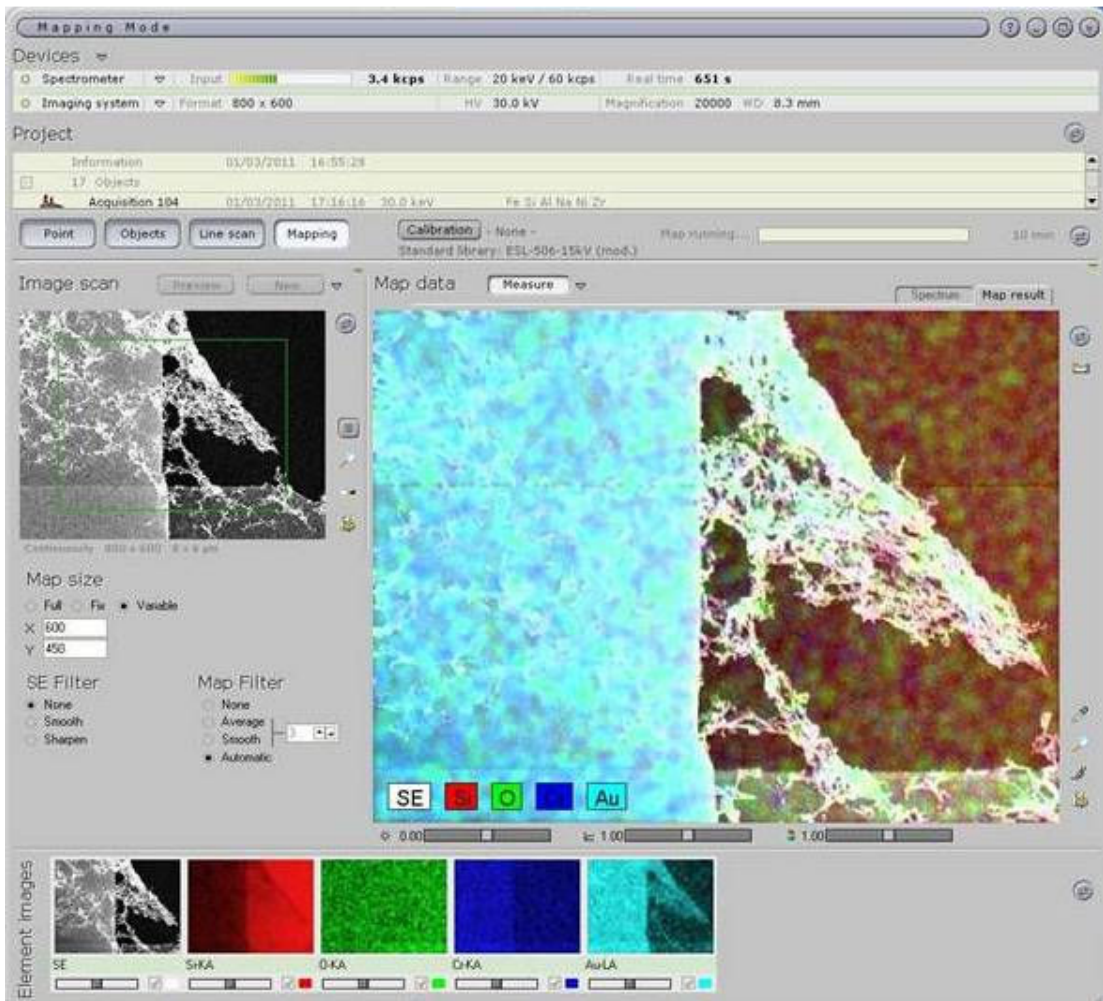
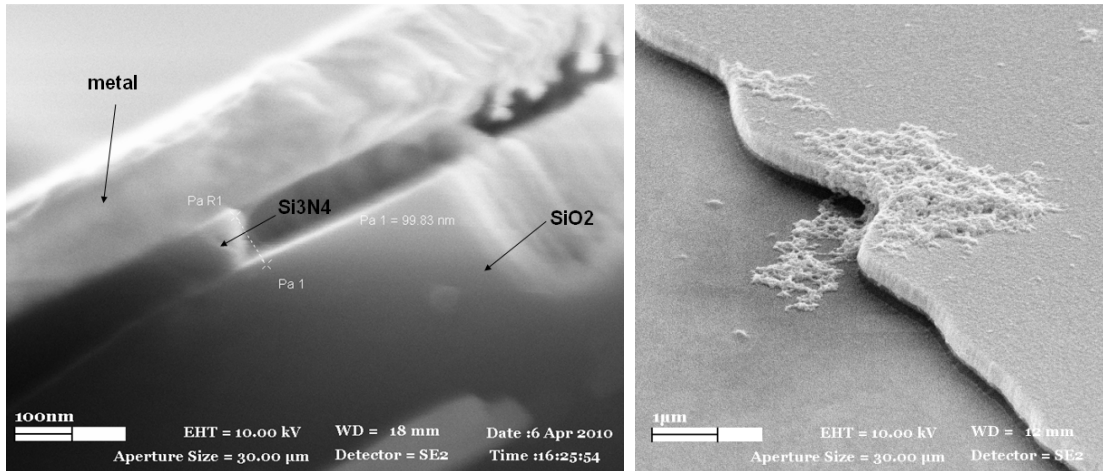


Figure 4.7: The SEM images and EDX analysis that show the results of SF₆ etching using DSE system are given. The SEM image on top left exhibits the isotropic nature of the etching and the image on top right shows the contamination which shunts the active device and the wafer surface. The EDX analysis at bottom proves that the contaminant is made of gold and it comes from the sputtering of the gold mask during dry etch.

Because of the problems with SF_6 , another fluoride-based gas, trifluoromethane (CHF_3) is decided to be used. For this purpose, a new line parallel to existing SF_6 line has been designed and built by our research group. A new recipe is developed for the anisotropic etching of the nitride layer using CHF_3/O_2 gas mixture. The new process is optimized such that a vertical profile at a reasonable etch rate is achieved without damaging the metal mask so there is no metal contamination on the device after dry etching. The process parameters are 50 sccm CHF_3 , 5 sccm O_2 , 60W RIE Power, 600W ICP Power, and 0.15 mBar pressure. The use of ICP power allows us to control the number density of the ions without changing the momentum of the ions. The etch rate using this recipe is approximately 40-45 nm/minute for LPCVD nitride. In order to etch 100 nm nitride layer, 3 minute etch is performed. When fluorocarbon-based plasmas are used for etching of insulating layers, an organic residue is formed on the surface of the sample^{130,131}. Oxygen plasma for 3 minutes is performed after each dry etch, before the subsequent wet etch to remove the organic residue from the sample surface. The SEM images of etched samples are given in Figure 4.8. The sidewall of the oxide layer is not totally vertical but it is not crucial since this layer will be removed in the subsequent wet etch step. The DSE system was suffering from turbo pump problems which caused serious variations in the etch rate and etch profile from sample to sample even though the exact same recipe was used. Because of this problem, the recipe has been fine-tuned for many times. We switched to a newly arrived system when the old system has completely broken down.

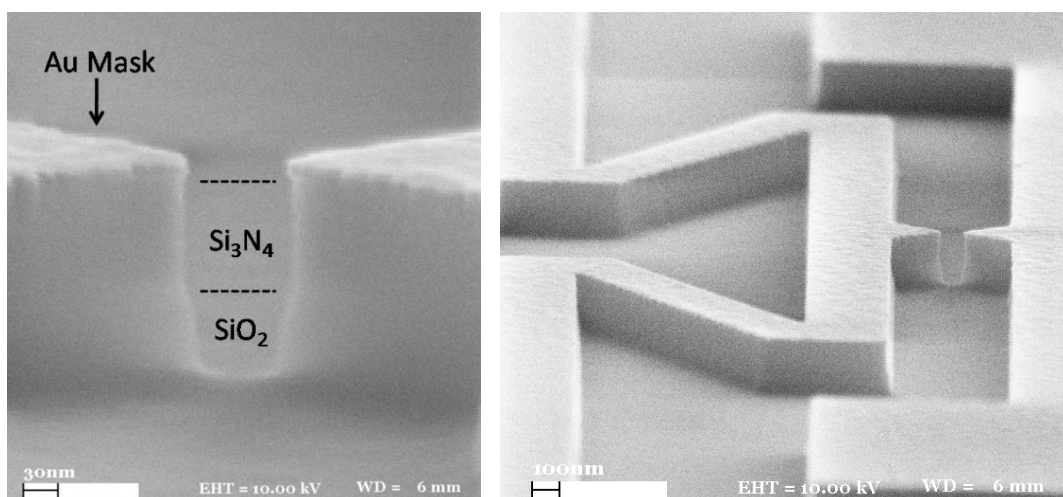


Figure 4.8: The SEM image shows the result of CHF_3/O_2 etching in DSE system. This gas composition can etch the nitride layer anisotropically without damaging the gold mask.

SF₆ PLASMA:

The last samples fabricated during this work are etched using pure SF₆ Plasma in Oxford PlasmaLab System. The recipe is provided by the manufacturer and the parameters are 45 sccm SF₆, 50W RIE Power, 2000W ICP Power, and 10 mTorr pressure. During etching the stage temperature is kept at 5°C and He back-cooling is 5 sccm. The etch rate for LPCVD nitride is 400nm/min and the etch profile is anisotropic. A 3-minute oxygen plasma is performed after nitride etch to get rid of the organic residues formed during SF₆ Plasma. The process has yielded repeatable results in terms of both etch rate and etch profile. The etch rate and profile is homogenous throughout the sample and the process leaves a smooth, residue free surface after etching as shown in Figure 4.9. The metal surface is not damaged during etching. This recipe etches both the nitride and the oxide layers vertically.

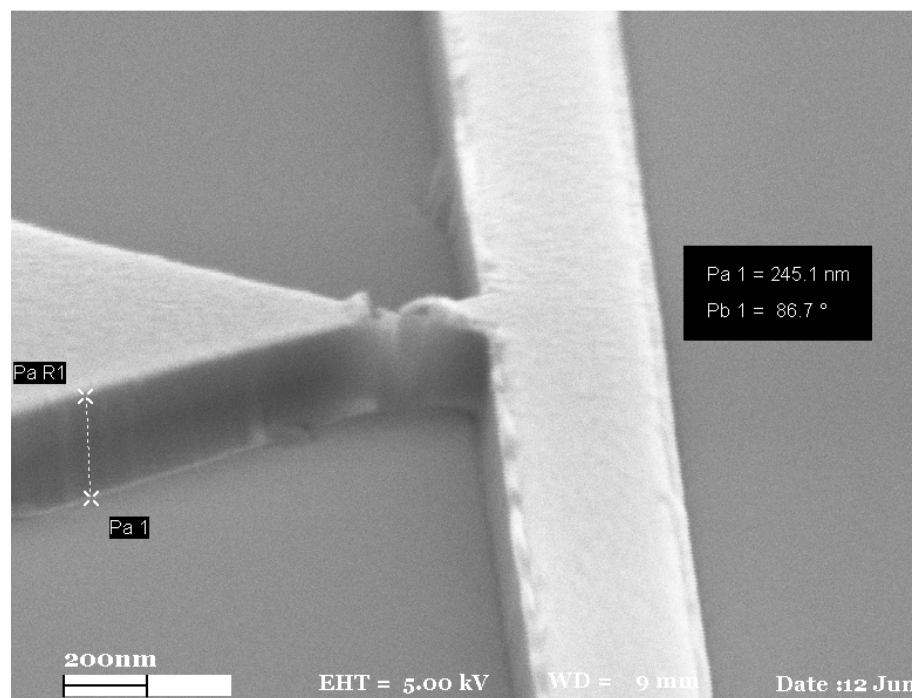


Figure 4.9: The SEM images show the result of SF₆ etching in Oxford system. This recipe provides high etch rates (400nm/min) with vertical sidewalls for LPCVD silicon nitride.

4.2.6 Wet Etching

Wet etching is a pure chemical process and it results in isotropic profile in most cases. In this work, the sacrificial layer of SiO_2 is etched using hydrofluoric acid (HF). HF is preferred since it only etches SiO_2 without damaging the metals (Cr/Au) and the nitride layer. In the beginning, the etching is performed by diluting HF (38-40%) with de-ionized water. Unfortunately, the etch rate of diluted HF is not stable since the number of fluoride ions in the solution decreases in time as the etching progress. Later, in order to keep the etch rate stable, commercially available buffered oxide etcher, BOE (a mixture of HF and ammonium fluoride) is used. The etch profile of the oxide after wet etch is given in Figure 4.10.

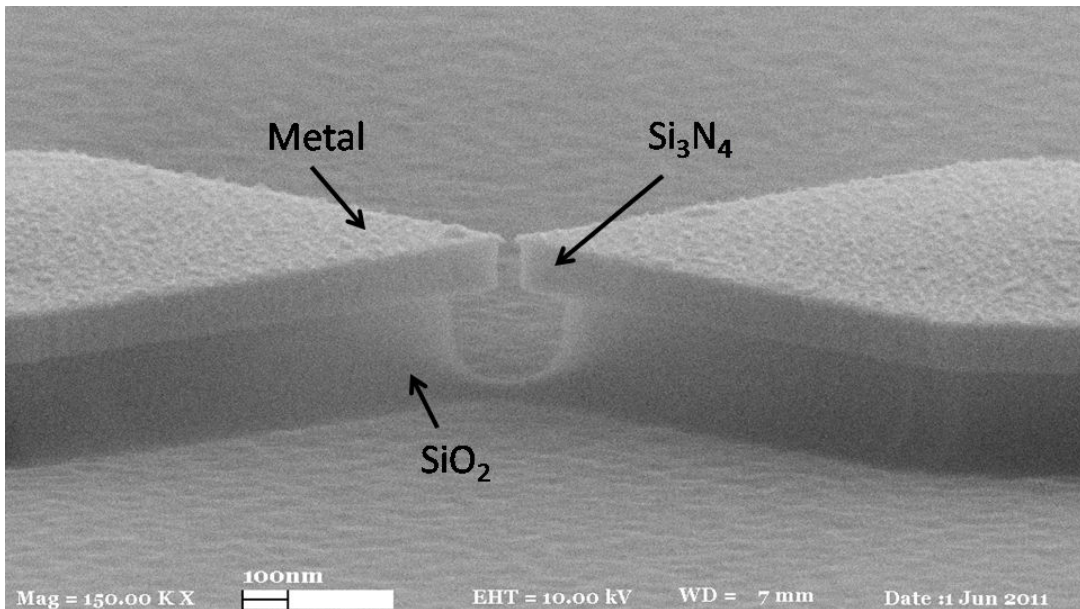


Figure 4.10: The SEM image of the device after isotropic etching of oxide layer using BOE is given.

4.2.7 Wafer Dicing

The samples are fabricated as a 4x4 array of 1.4 mmx1.4 mm squares. The array is fractured at the end of the process flow. Earlier, the cutting is performed manually by diamond scribe and unfortunately an important number of samples are ruined during this manual cutting. In the final phase of this work, a newly arrived dicer (DISCO DAD 320 Automatic Dicing Saw) has been used to precisely cut the samples. The samples are covered with a protective layer of photoresist and diced before the etching steps since the dicing process will ruin the suspended structures.

4.2.8 Wire Bonding

Once the fabrication of the devices is completed, each device is glued on a chip carrier using an adhesive like epoxy or silicon. Then the wire connections from the contact pads on the device to the leads of the chip carrier are performed. For this purpose a wire bonder (Kulicke and Soffa) is used. In this method, a thin gold wire (diameter of 18.5 μm) is bonded both to the contact pad and to the chip-carrier contact lead by applying ultrasonic vibration and vertical force. For successful bonding, the contact pads should be thick (200 nm) and wide (min 100 μm) enough and the adhesion between the contact pad metal and the wafer should be strong. The adhesion is promoted by getting rid of any organic residue on the wafer before metal coating using oxygen plasma and by coating a 10 nm chromium layer before gold evaporation. Chromium is especially preferred as the adhesion layer since it is not affected from the subsequent HF wet etching. For instance, another widely used adhesion metal, titanium cannot be used in this work since it is etched by HF.

4.3 Device Fabrication Process Flow

4.3.1 Tunnel Junction/Nanogap Fabrication

Vacuum tunnel junction or nanogap device consists of two metal tips suspended in the air with nm or sub-nm gap in between. The resolution of the standard nanofabrication methods is not enough for the direct fabrication of nm or sub-nm gaps. In this work, a wider gap is further shrunk using controlled thermal evaporation which will be discussed in detail in the next chapter. The original gaps of width 10-30 nm are fabricated with EBL and made suspended in the air with dry and wet etching to avoid short-contact during subsequent controlled thermal evaporation. The schematic which shows the final form of the device before controlled thermal evaporation is given in Figure 4.11. The process flow has been modified and optimized many times due to unpredictable technical and methodological problems faced during fabrication. The developed recipes and their problems are summarized along with the final successful one.

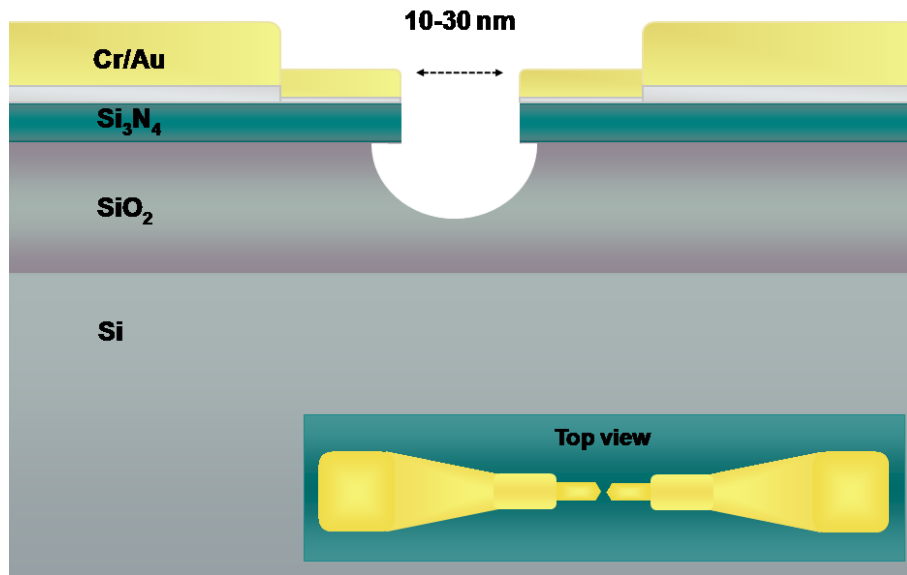


Figure 4.11: The schematic illustrates the side view and top view (inset) of the tunnel junction/nanogap device used in controlled thermal evaporation experiments.

PROCESS FLOW 1:

The DesignCAD drawing and the pictures of the optical mask used in the first developed process flow are given in Figure 4.12.

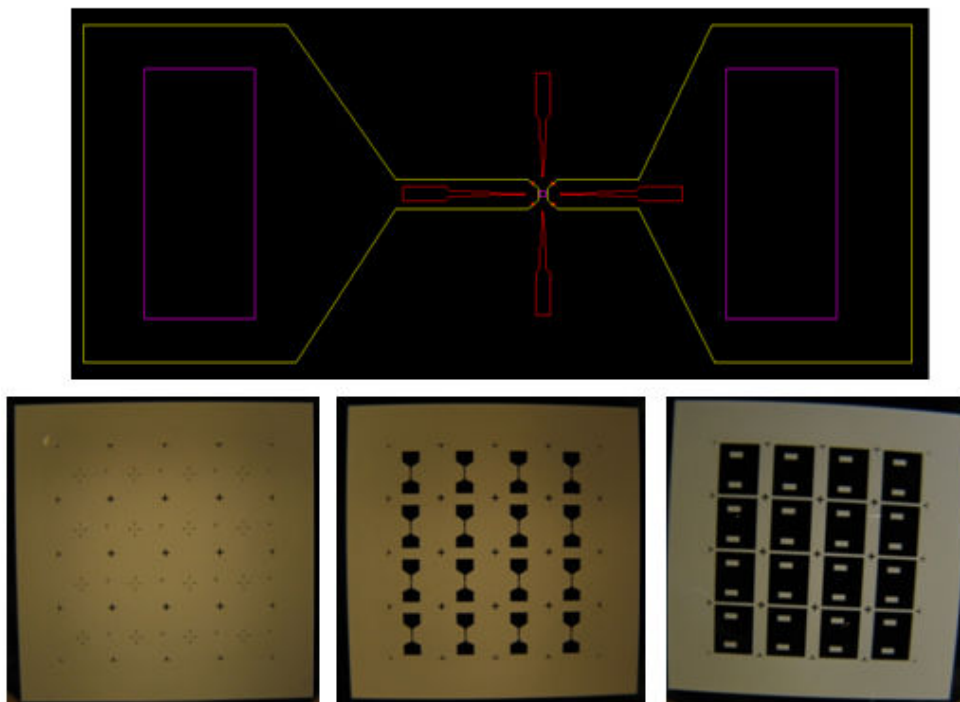
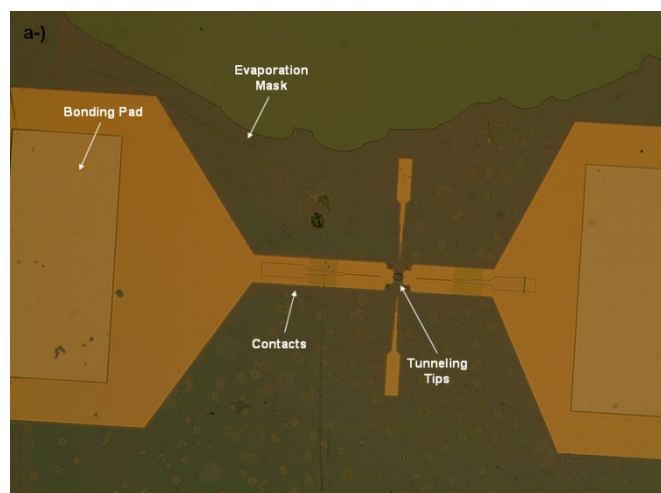


Figure 4.12: DesignCAD drawing and the pictures of the optical mask used in the first developed process flow are given.

1. The alignment markers shown with red are transferred to the sample with negative photolithography and metal evaporation (5nm Cr/50 nm Au).
2. Two metal tips that are separated by 10-30 nm are patterned with monolayer EBL and transferred to the sample using metal coating (5nm Cr/30 nm Au). The position of the metal tips is determined using alignment markers.
3. The contact pads shown with yellow are fabricated using negative photolithography and metal evaporation (10nm Cr/200 nm Au). These contact pads partly overlap with EBL metal tips and form the bonding areas for wire bonding.
4. The evaporation mask shown in purple is fabricated using positive photolithography in order to protect the areas other than active region, from the subsequent etching and thermal evaporation steps.
5. The nitride layer is isotropically etched with old DSE system using SF_6/O_2 plasma. Vertical sidewall profile could not be achieved in this system with SF_6/O_2 gas configuration. The oxide layer is etched isotropically using HF:de-ionized water.
6. The samples are cut with diamond scribe, pasted on chip carrier using PMMA and wire bonded. The optical microscope and SEM images of the first fabricated devices are given in Figure 4.13.



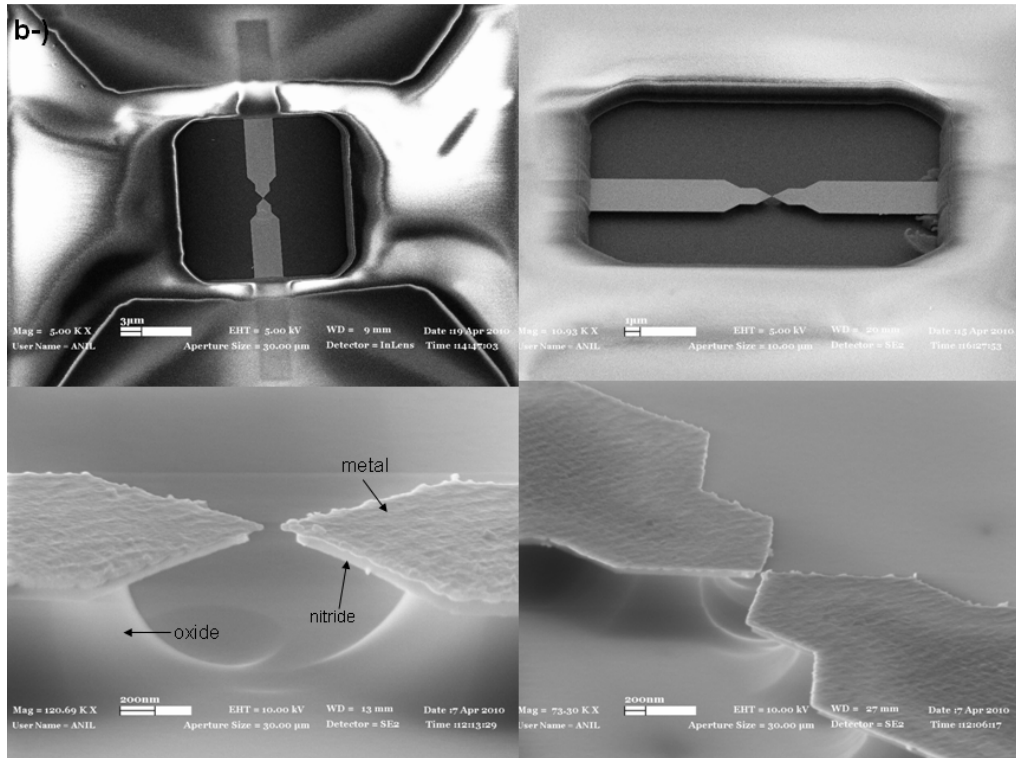


Figure 4.13: The optical microscope (a) and SEM (b) images of the devices fabricated using “Process Flow 1” are given.

Two problems arose from this process flow:

1. Wire Bonding Problem: Gold contact pads were ruptured and peeled off from the sample surface during wire bonding even though very weak ultrasonic powers and vertical forces were used. This problem pointed towards the poor adhesion between the contact pad and wafer. The first thought was that long wet etching using high concentration HF might cause the problem. However, a series of controlled experiments showed that, PMMA residues remained on the surface after EBL induced the adhesion problem. The simplest solution was to change the order of contact pad and metal tip fabrication in the process flow. In this way, first the contact pads were formed when there was no PMMA residue on the surface and then the metal tips were placed using EBL. This method has solved the wire bonding problem.
2. Evaporation Mask and Short Circuit Problem: The evaporation mask that was initially used to protect the inactive regions resulted in short-circuit problems during controlled thermal evaporation. When the surface and sidewalls of the

evaporation mask were coated with a few nm gold, short-circuitry between metal tips was formed as shown in Figure 4.14. Since the controlled thermal evaporation method is based on the in-situ monitoring of the conductance between the metal tips, the short-circuit problem completely ruins the sample. Therefore, the use of evaporation mask has abandoned and removed from the process flow.

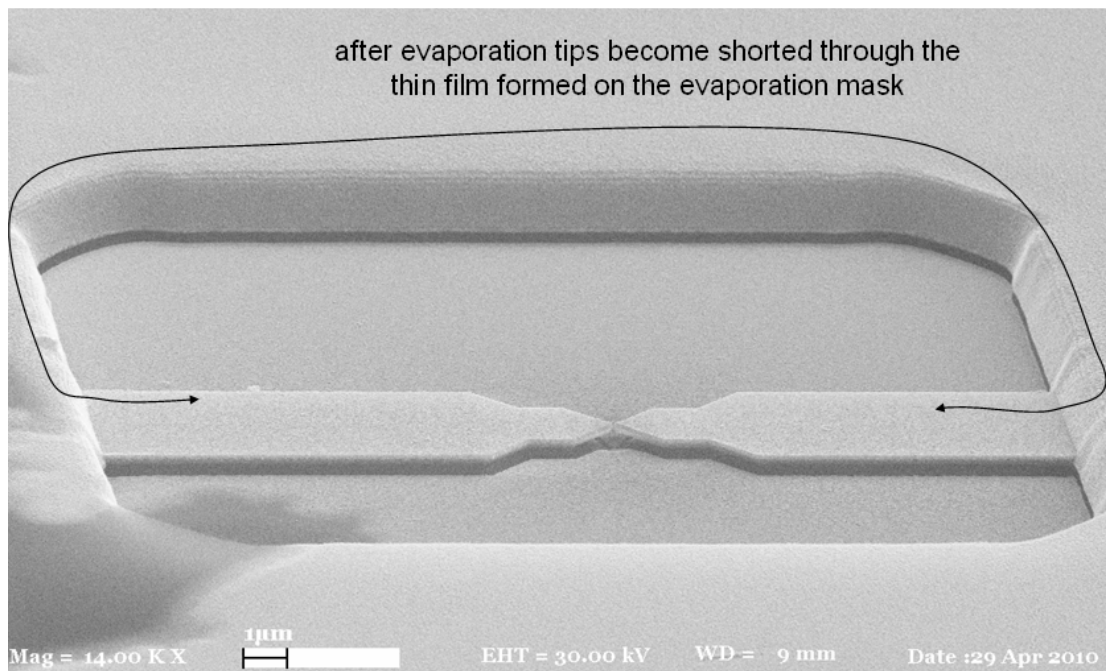


Figure 4.14: The short-circuit problem which shows up when the evaporation mask is coated with gold atoms during controlled thermal evaporation is described on the SEM image.

PROCESS FLOW 2:

A new process flow has been developed by finding solutions to the problems arose in “Process Flow 1”:

1. Contact pads are formed using negative photolithography and metal evaporation (10nm Cr/200 nm Au).
2. Metal tips are formed using EBL and metal evaporation (5nm Cr/30 nm Au).
3. Si₃N₄ layer is etched isotropically using SF₆/O₂ plasma.

4. The oxide layer is etched isotropically using HF:de-ionized water.
5. Samples are cut, pasted on chip-carrier and wire bonded.

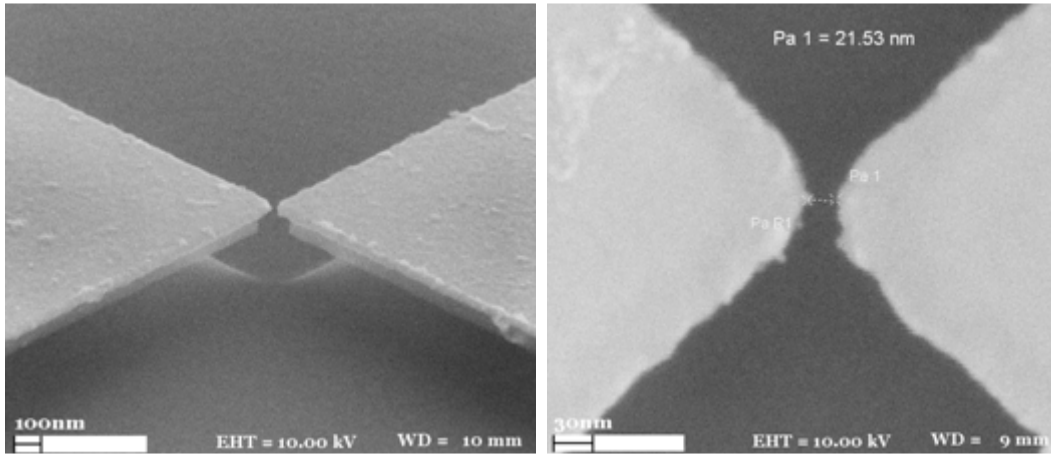


Figure 4.15: The tilted and top view SEM images of one of the devices fabricated using “Process Flow 2” are given.

The first samples produced with this process flow were quite successful and used in control thermal evaporation experiments. However, the same process flow has failed in the latter samples. It was observed that some shiny materials like dirt contaminated the devices after etching steps. Some of these dirt-like structures were touching both the metal parts and wafer surface and resulted in short-circuitry during controlled thermal evaporation. As discussed earlier in Part 4.2.5, the EDX analysis showed that these dirt-like structures were made of gold and they were sputtered from the sample surface and reattached during dry etching. Firstly, it was thought that covering the gold surface with a more durable material like titanium would prevent the sputtering during dry etch and the titanium layer would be removed later during wet etch. Unfortunately, titanium layer did not solve the contamination problem. Secondly, the PMMA residue remained on the developed areas were thought to spoil the adhesion of the thin Cr/Au film and hence the metals were ruptured from the surface of the wafer during dry etch. At this point the oxygen plasma recipe was developed to remove the PMMA residue after development and before metal coating. Oxygen plasma has definitely improved the film quality of the metal structures and yielded cleaner lift-off results but it did not solve the metal contamination problem as seen in Figure 4.16. As the final solution, the dry etch gas configuration has been changed from SF_6/O_2 to CHF_3/O_2 and a totally new dry etch recipe has been developed.

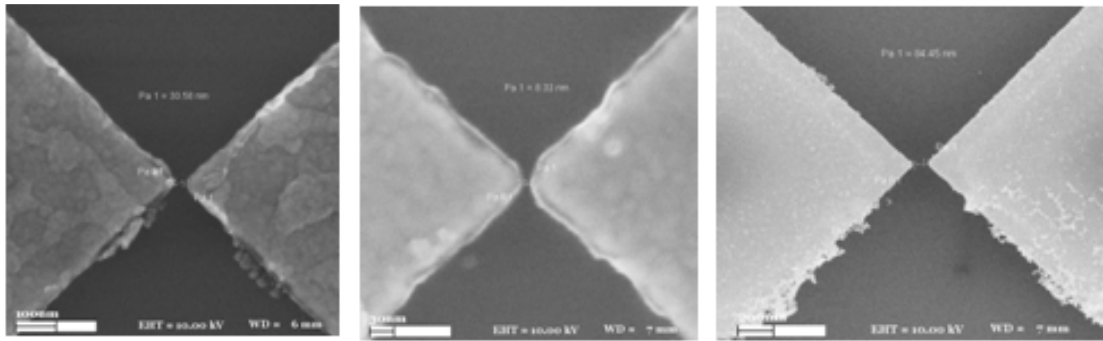


Figure 4.16: When the image in the middle (O_2 plasma after development) is compared to the image on the left (no O_2 plasma after development), it is observed that the quality of the metal film is better and the edges are cleaner. On the other hand, the image on the right shows that O_2 plasma does not solve the contamination problem.

The other problem was that, the separation between the metal tips significantly increased after wet etching as shown in Figure 4.17. Literature search and controlled experiments have revealed that the metals tips move away from each other because of the contraction and buckling of the high tensile stress nitride thin film once the oxide layer beneath it is removed after wet etch. The problem and the solution are discussed in detail in Chapter 6.

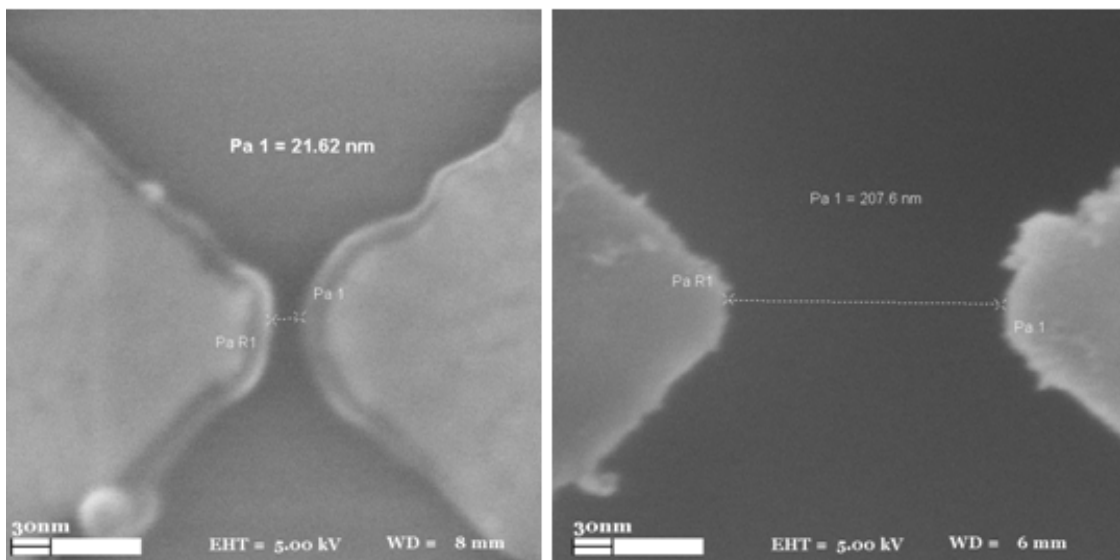
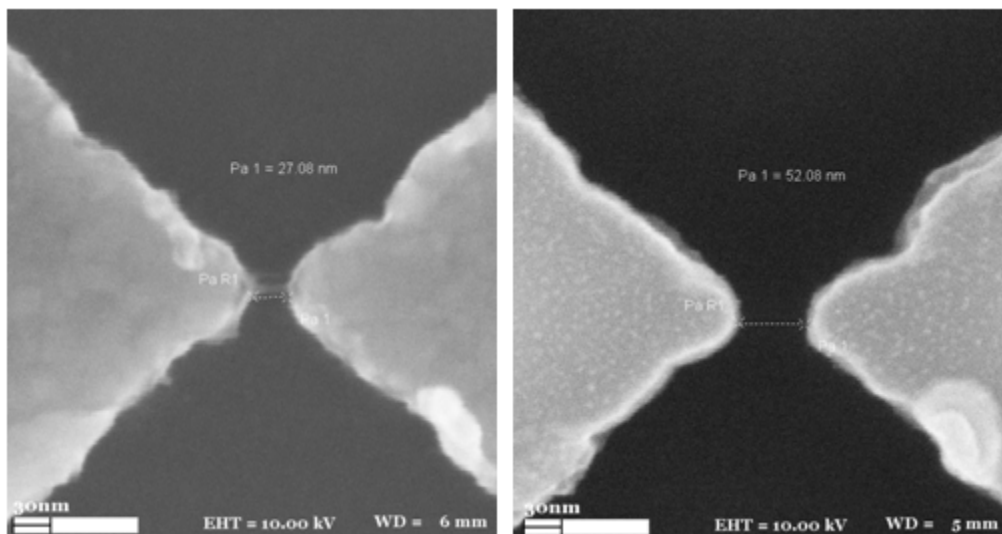


Figure 4.17: The SEM images show that an originally 21 nm gap width is increased to 207 nm after wet etch.

PROCESS FLOW 3:

All the problems other than the widening of the gap have been solved and the process flow has been finalized successfully.

1. The alignment markers are patterned using photolithography, O₂ plasma and metal coating (5nm Cr/50 nm Au).
2. Metal tips nm are patterned using monolayer EBL, O₂ plasma and metal coating (5nm Cr/30 nm Au).
3. The contact pads are patterned using photolithography, O₂ plasma and metal coating (10nm Cr/200 nm Au).
4. Si₃N₄ layer is etched anisotropically using CHF₃/O₂ gas configuration without damaging the metal layers. Succeeding oxygen plasma is performed after dry etch to remove the organic byproducts.
5. The oxide layer is etched isotropically using BOE.
6. The samples are fragmented using dicer, pasted on chip carrier using silicon and wire bonded. Silicon is preferred to PMMA for pasting since it is softer and it blocks the mechanical vibrations better.



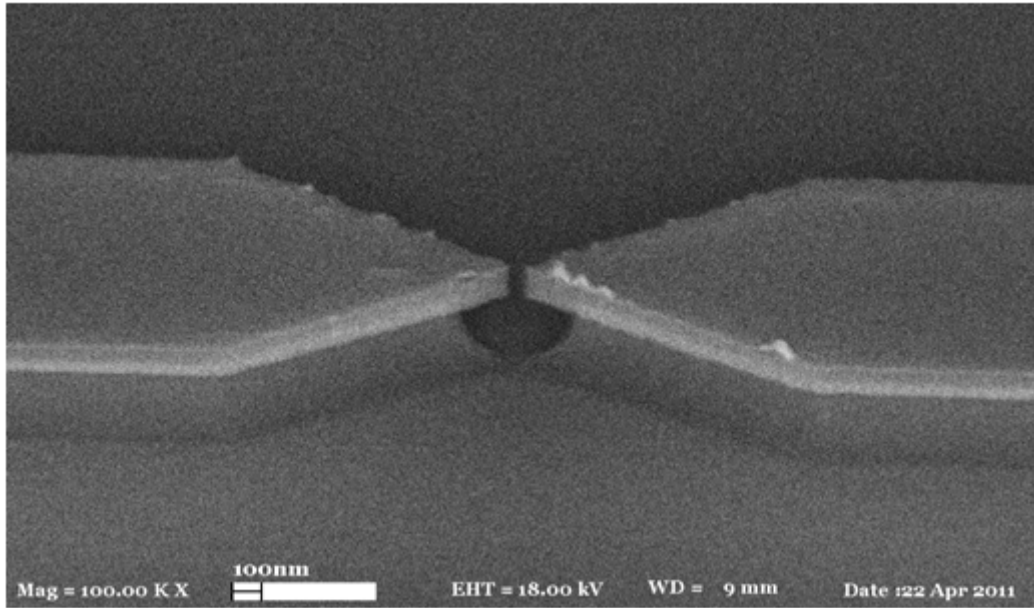


Figure 4.18: The SEM images of the devices fabricated using “Process Flow 3” are given. The top images show the increase in the gap width from 27 nm after EBL (left) to 52 nm after wet etch (right). The bottom image reveals that CHF_3/O_2 plasma etches the nitride layer vertically without contaminating the sample.

4.3.2 Tunnel Junction-Nanobeam Embedded System Fabrication

One of the main motivations of this thesis is to fabricate a nanomechanical doubly clamped beam which is coupled to a vacuum tunnel junction. The device consists of a metalized suspended beam and a metal tip with a nanogap in between as depicted in Figure 4.19.

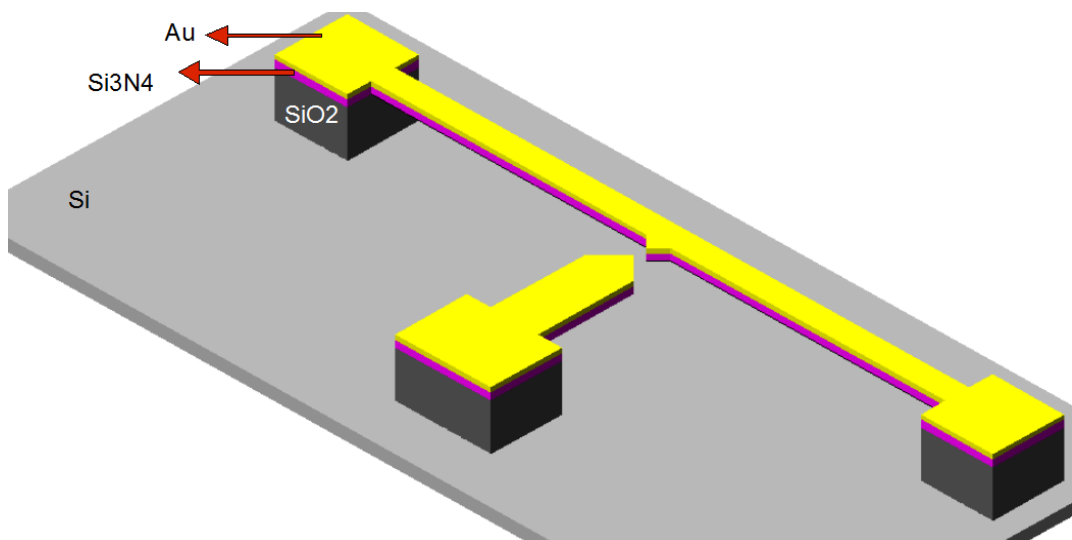
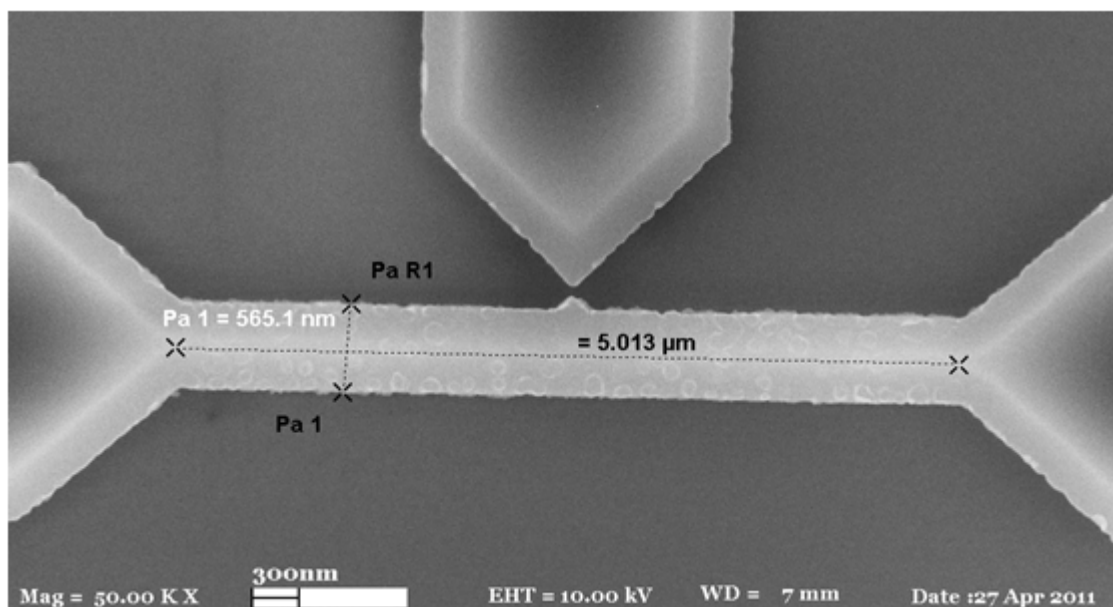


Figure 4.19: The schematic illustrates the isometric view of tunnel junction-nanobeam embedded system.

The final process flow developed for the tunnel junction fabrication is applied successfully to the tunnel junction-nanobeam embedded system. A new photolithography mask is designed and developed for the new pattern. Bilayer EBL is preferred for cleaner lift-off results. The anisotropy of the silicon nitride dry etch is critical for nanobeam fabrication since the geometry of the beam affects the mechanical characteristics of the resonator such as resonance frequency and dissipation. The former devices are fabricated using CHF_3/O_2 in DSE system and then switched to SF_6/O_2 in Oxford system. The thickness of the nanobeam is determined by the thickness of the nitride thin film which is 100 nm. Wet etch time is adjusted such that the entire oxide layer under the nanobeam is etched and the structure becomes suspended. In other words, wet etch time is determined according to the width of the nanobeam. The LPCVD silicon nitride thin film has high tensile stress and it is mechanically stable. As a result, there is no need for a special method like critical point drying after wet etch. The samples are first gently rinsed in de-ionized water for 5 minutes. Then the samples are immersed in a low surface tension liquid like IPA or methanol for another 5 minutes. Finally the samples are dried with nitrogen gun. No series stiction problem has occurred during nanobeam fabrication. SEM images of the one of the fabricated devices are given in Figure 4.20.



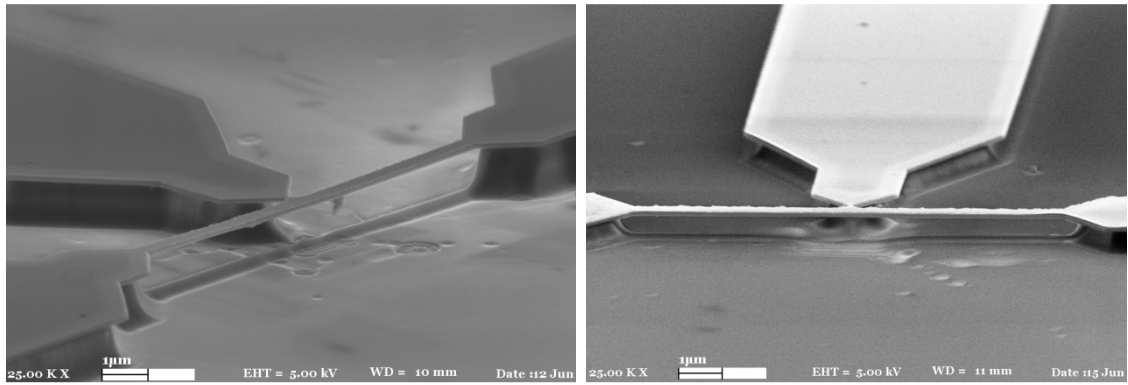
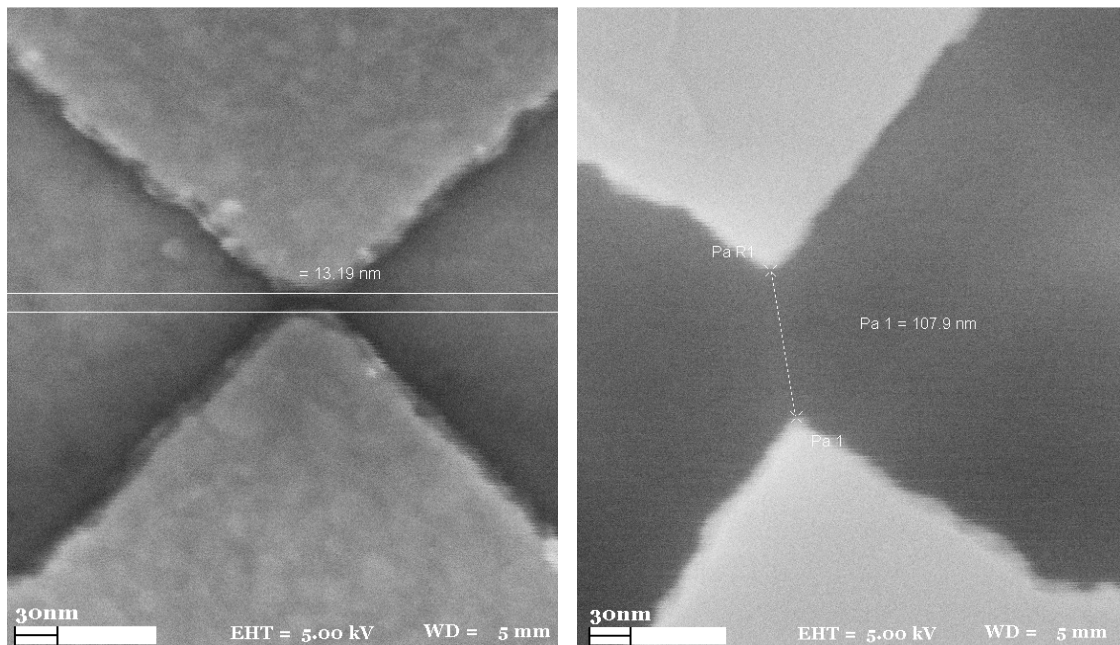


Figure 4.20: The top view SEM image of a metal tip-nanobeam embedded device is given. The length, width and thickness of the nanobeam are 5 μm , 500 nm and 100 nm respectively (top). The side view SEM images of another device are given from different angles (bottom).

The widening of the gap after wet etch is also observed for metal tip-nanobeam embedded system. In Figure 4.21, it is shown that the originally 10 nm gap width increases to 100 nm after wet etch. This problem is caused by the intrinsic high tensile stress of the nitride film and it is not related to the recipes or the process flow applied. Since it is an intrinsic problem, a novel solution has been developed to solve this problem as discussed in Chapter 6.



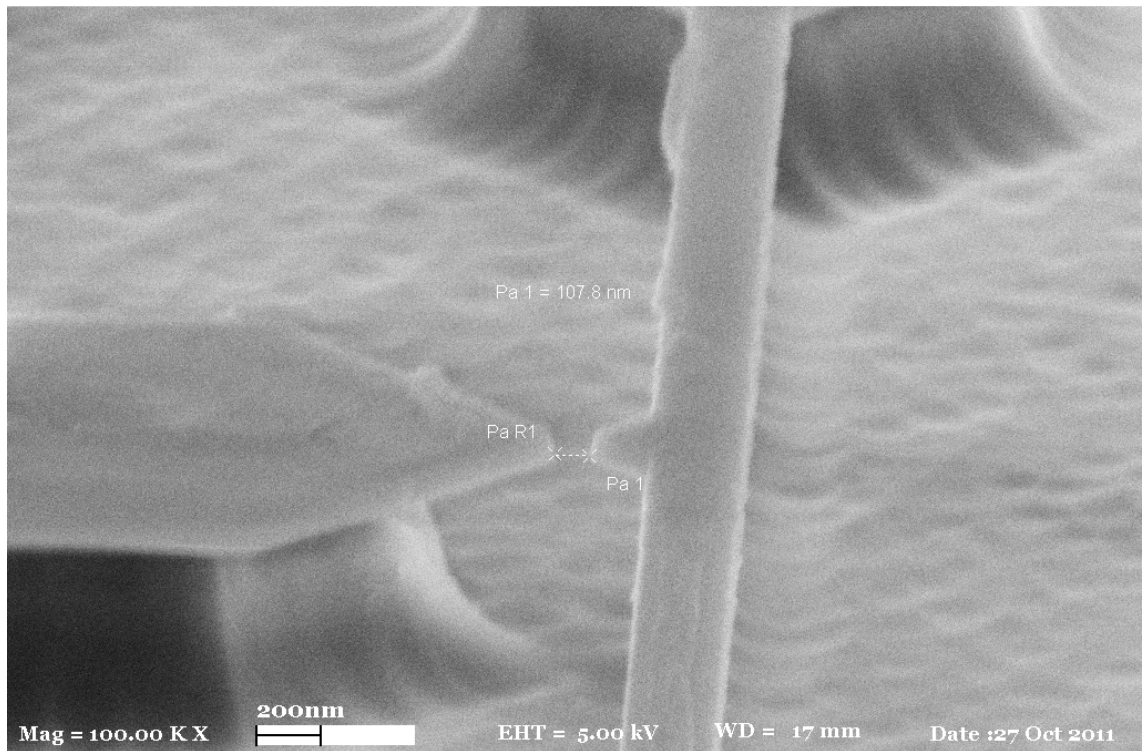


Figure 4.21: The top view SEM images show the increase in the gap width from 13 nm after EBL (left) to 108 nm after wet etch (right). The side view of the same device after wet etch is given at the bottom.

CHAPTER 5

CONTROLLED FABRICATION OF VACUUM TUNNEL JUNCTIONS

5.1 Introduction

Vacuum tunnel junction or nanogap can be basically defined as two metallic electrodes with a few-nanometer or a sub-nanometer gap in between. As mentioned earlier in Chapter 3, nanogaps find a wide range of applications in high end and state of the art technologies. Conventional lithographic techniques like EBL cannot yield the sub-nanometer resolution required for such applications and hence advanced novel techniques have to be developed for the realization of nanogaps. A diverse range of nanogap fabrication techniques have been discussed in Chapter 3. Although these methods successfully produce nanogaps, they either suffer from low yield or have inherent bulky structures incompatible with integrated electronic or nanoelectromechanical device applications. Therefore, there is still a great need for a well-controlled fabrication technique for the realization of clean nanogaps.

In this work, we introduce a new method in which high stability vacuum tunneling gaps are produced via controlled-shrinkage of a wider gap by thermal evaporation. Therefore, it is possible to consistently produce rigid and stable nanogaps with about 1 nm or less gap size. In this chapter, first the experimental details of sample preparation and controlled thermal evaporation are given. Then the details of three, successfully fabricated devices are provided. The fabricated nanogaps are characterized using Simmons's model. The stability of the tunnel junctions are tested with further electrical measurements. The results are analyzed and discussed in detail.

5.2 Experimental Setup

5.2.1 Sample Preparation

The devices were fabricated on a Si wafer with a thermally grown 1 μm SiO_2 layer on top of the Si and a 100 nm thick LPCVD grown Si_3N_4 layer on top of the oxide layer. The primary metallic tips or the nanobeam-metal tip system were patterned with EBL and metallized by 5 nm Cr / 30 nm Au. 10-50 nm gaps between metal tips were routinely achieved using EBL. The nitride layer was vertically etched using either CHF_3 or SF_6 reactive ion etching while the metal pattern was serving as an etch mask. The oxide layer was isotropically removed by chemical etching in BOE and the metal tips became suspended in air. The devices were bonded on a chip carrier by using a soft adhesive to minimize the transfer of mechanical stress to the device during its handling. The fabrication steps are illustrated in Figure 5.1 and the details of device fabrication is provided in the previous chapter.

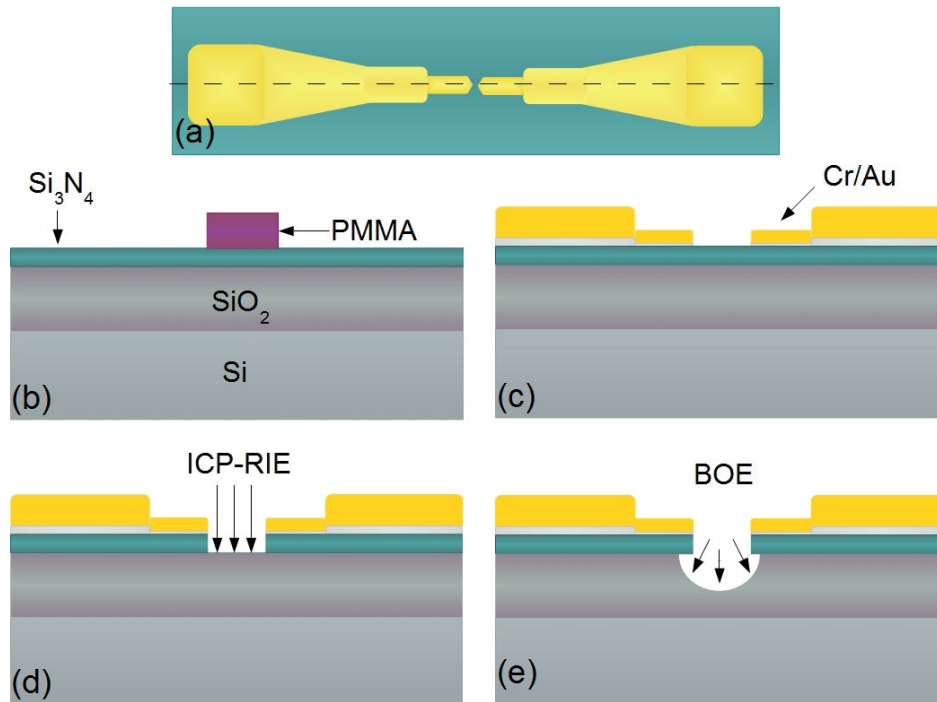


Figure 5.1: The fabrication steps of the device: (a) Top view of the device fabricated. The dashed line shows the position of the cut for the cross-sectional views shown in (b) to (e). (b) PMMA coated on top of LPCVD nitride thin film, then exposed and developed, (c) a thin layer of Cr/Au coated and lifted-off, (d) the pattern is transferred to nitride layer using ICP-RIE, (e) the sacrificial oxide layer etched using BOE to form an undercut under the metal electrodes.

5.2.2 Controlled Thermal Evaporation

The main motivation of this work is to produce nanogaps by filling the lithographically defined gap between the metal tips which is about 20-40 nm. This is done by further coating the tips with Au by thermal evaporation. The evaporation is performed under a vacuum of 10^{-7} mBar and the gold deposition rate is kept at 1 Å/s. In order to keep the sample temperature as low as possible, deposition is performed in a number of steps as needed with cool down phases in between. Although the evaporated Au atoms land vertically on the metal tips, they also overhang at the sides and result in the reduction of the gap size. Even though it varies from sample to sample, we found that the swelling at the sides is in average between 1/7 and 1/9 of the coated thickness. A mechanical mask is employed to prevent formation of any parallel conductance elsewhere. Throughout the evaporation, temperature, pressure, film thickness and evaporation rate are monitored continuously. The gap is DC biased and the current flow across it is measured at 5 Hz rate during the evaporation. A threshold current is set before the evaporation and the system compares the measured current and the threshold current throughout the evaporation. As the gap shrinks to about a nanometer, a tunneling current starts to flow between the electrodes. As soon as the tunneling current exceeds the pre-set threshold current, the evaporation is immediately halted by shutting off the evaporator source current. The working principle of the experimental setup is given in Figure 5.2.

A home-made, high vacuum thermal evaporation system has been designed, built and functionalized by our research group to perform nanogap fabrication experiments. The schematic and the real pictures of home-made thermal evaporator are given in Figure 5.3 and Figure 5.4, respectively. The details of the system are as follows:

1. The system basically consists of a stainless steel base with vacuum feedthroughs and a glass belljar. The high vacuum is sustained with a turbo pump (Varian TV-301) and a scroll pump (Varian SH-110). It takes approximately 1 hour for the system to reach the operating pressures of 10^{-6} to 10^{-7} mBar. The pressure is monitored continuously using an ion gauge.

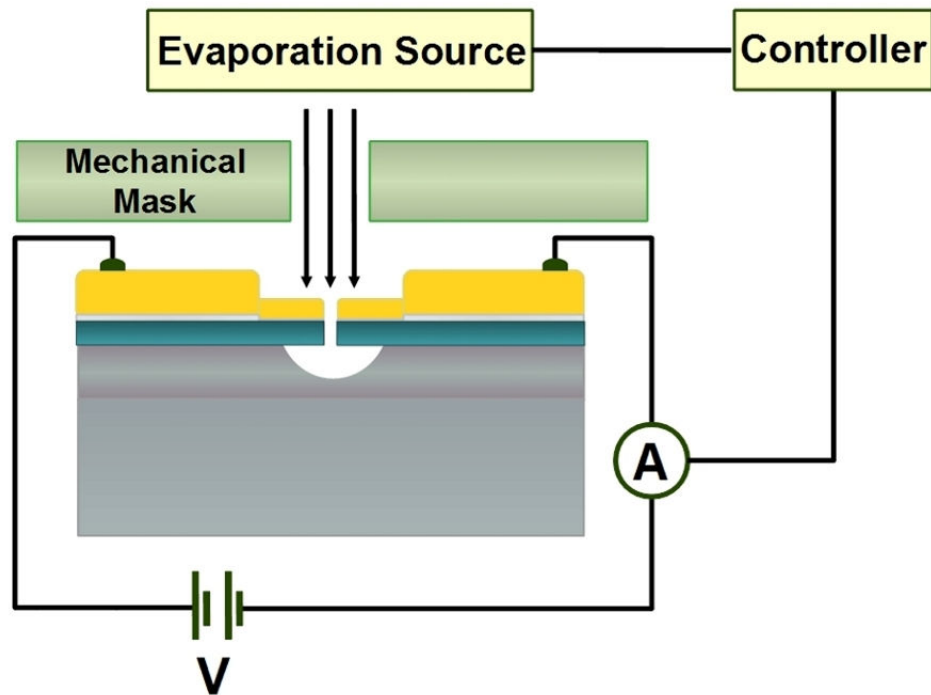


Figure 5.2: The figure illustrates the working principle of the controlled thermal evaporation.

2. Thermal evaporation is performed by heating a resistive element like a tungsten boat or basket, by passing through a high current. The material to be coated is placed on the source and the coating starts when the sample is taken to a temperature which produces sufficient vapor pressure. Our system has three separate sources for the use of different materials like gold, chromium, and titanium. The sources are heated using a high current power supply (Agilent N5762A, 8V, 165A, 1320W).
3. The chip carrier is placed in a socket to which the electrical wires are connected (Figure 5.4). The socket is screwed to a small sample holder which can be inserted to different locations on the top plate. By changing the location of the sample holder, the evaporation angle between the source and the sample can be adjusted. Additionally, the stage of the sample holder is rotatable through a vacuum step motor. Both the direction (clockwise, counterclockwise or alternating) and speed of the rotation are controlled with a home-made electronic system.

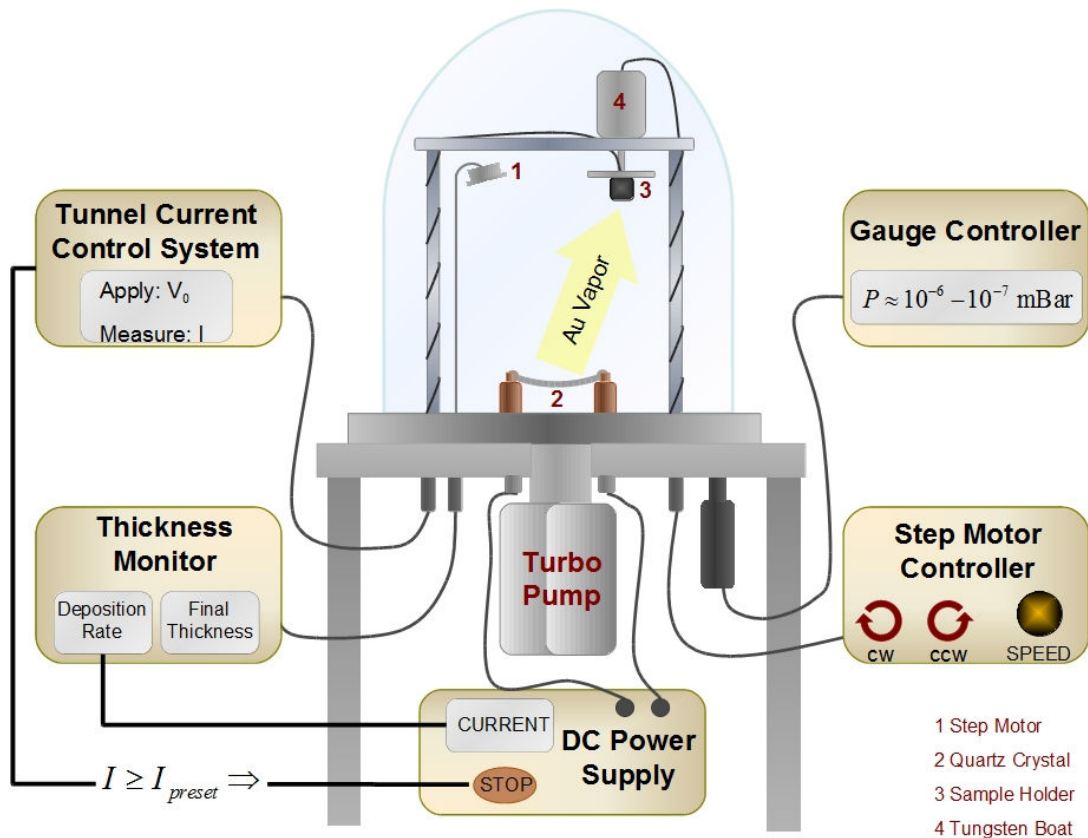
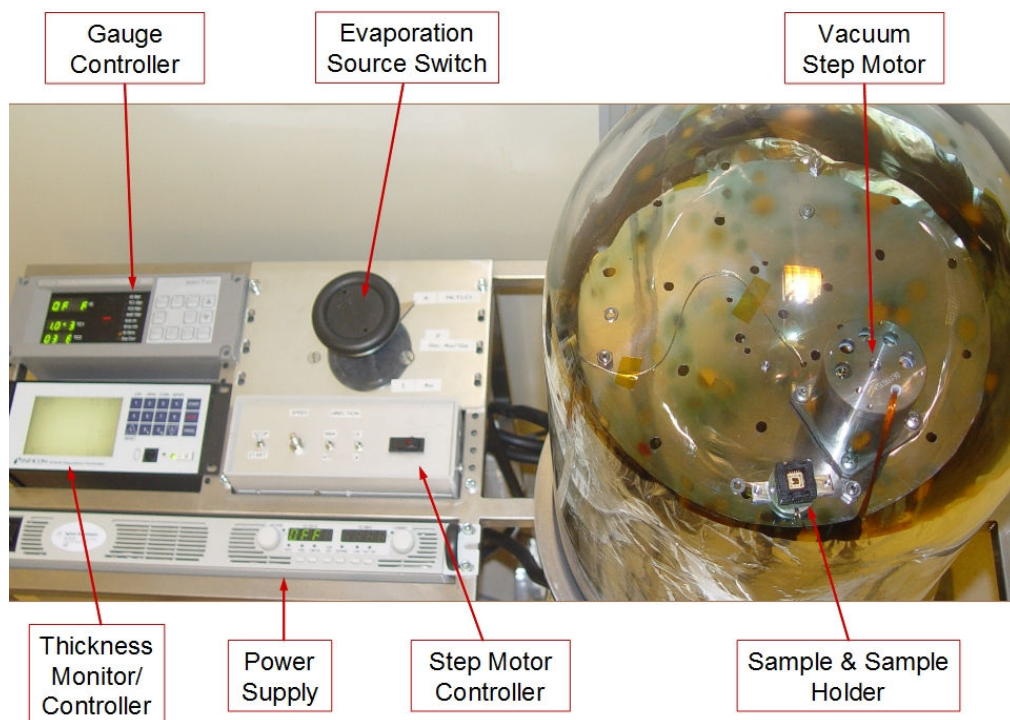


Figure 5.3: The figure illustrates the “home-made” thermal evaporation system

4. The deposition rate and thickness can be monitored and controlled using a quartz crystal inside the chamber and a thickness monitor/controller unit (Inficon XTC2). A quartz crystal’s resonance frequency shifts with the additional mass of deposited material. Thickness monitor calculates the deposition rate and total thickness of the thin film from the shift in the quartz crystal’s resonance frequency. In addition to monitoring, XTC2 controls the output current of the power supply to adjust the deposition rate. For more accurate measurements, a water cooling system is installed to cool down the quartz crystal and minimize the thermal drift during evaporation.

5. The most important and unique feature of the home-made thermal evaporator is the in-situ conductance measurement. The sample is electrically connected to a source/measure unit (Agilent 4156C semiconductor parameter analyzer). The unit is controlled from the PC using LabView Program and it can be operated either in sweep or

sampling mode. In the sampling mode, it applies a constant DC bias to the sample and measures the current simultaneously during evaporation. A threshold current is determined before the evaporation and the system constantly compares the measured current with the predetermined threshold current. As the deposition proceeds, the gap becomes narrower and narrower and at some point, it enters the tunneling regime that causes a very sharp increase in the measured current. When the measured current reaches the threshold value, the PC immediately terminates the evaporation by halting the power supply. At the end of this process, a vacuum tunnel junction is formed at a predetermined resistance. The typical values we practice are a bias voltage of 100 mV-2V and a tunneling current of 10-20 pA, which forms a tunnel junction with a resistance of GΩ-TΩ. The values of the tunneling resistance and hence the tunneling gap can easily be tuned by simply changing either the bias voltage or the threshold current. This method offers great control over the process and increases the fabrication yield. Sweep mode basically stands for I-V measurement and is performed by applying a linearly increasing/decreasing bias and measuring the current. I-V measurements are required for the characterization of fabricated nanogaps.



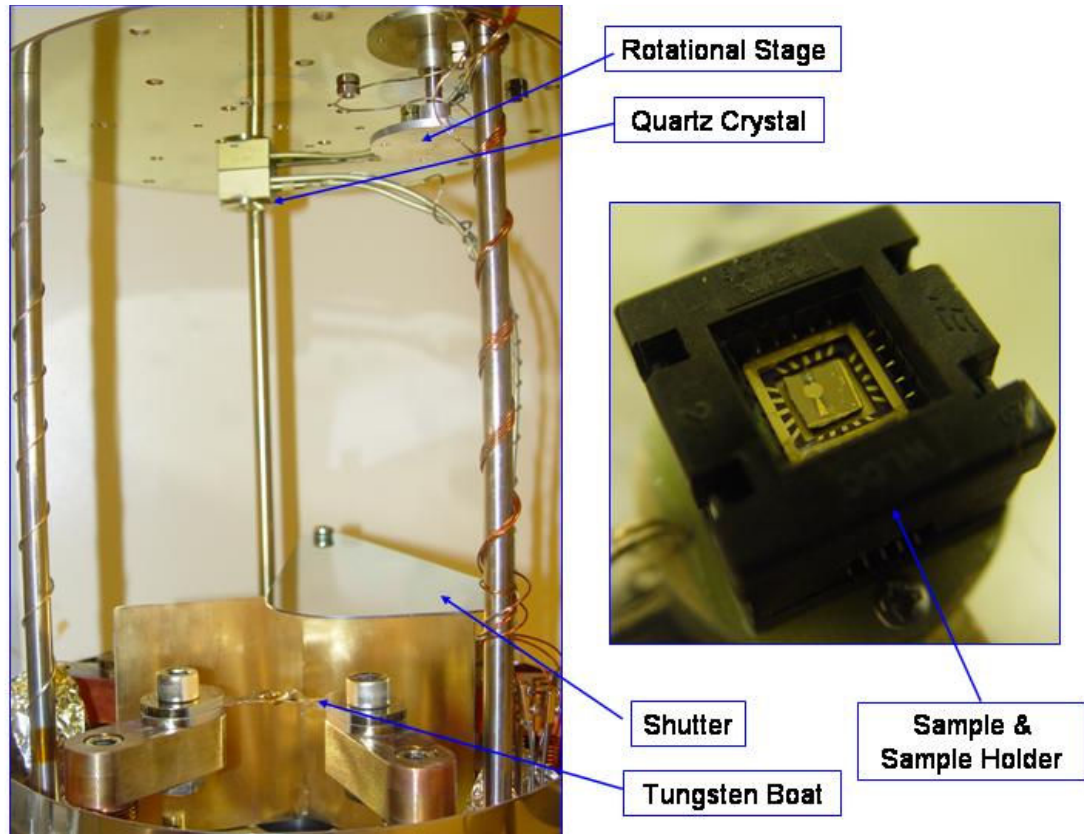


Figure 5.4: The pictures of the outside (top) and inside (bottom-left) of home-made thermal evaporator and the sample holder (bottom-right) are given.

5.3 Results of the Experiments and Characterization of Nanogaps

During this work, stable nanogaps are successfully fabricated and characterized for three samples. The number of successful experiments is restrained because of the “widening of the gap sizes after release” problem as mentioned in the previous chapter. In most of the samples, initially 20-40 nm gap sizes increased to over 100 nm after wet etch. The coating thickness during controlled thermal evaporation should be close to μm range in order to be able to fill such wide gaps. The increase in the coating thickness impairs the experiments in three ways. First of all, the risk of unwanted parallel conductance from other parts of the sample increases drastically for thicker coatings. Secondly, the sample goes through more heat and cool cycles as the number of evaporation steps increases. As a result, metal layers buckle and curve due to successive thermal expansions and contractions. Last but not least, when the inner surface of the bell jar is coated with gold, the thermal radiation from the boat is trapped inside and causes an increase in the sample temperature. In other words, the maximum

sample temperature reached during experiment is higher for thicker coating because the bell jar becomes a stronger reflector. The over-heating of the sample causes shape distortions on the metal layers and increases the thermal noise which hinders the experiment. All in all, wide gaps are not suitable for nanogap fabrication using controlled thermal evaporation. Experiments performed on numerous samples with different gap sizes showed that, for nanogap fabrication, the gap size should be smaller than 40 nm before controlled thermal evaporation. During this work a new method is developed to treat the gap widening problem which is discussed in the next chapter. Here, the details of nanogap fabrication and characterization of three samples with sub-40 nm initial gaps are given in chronological order.

SAMPLE 1:

The initial gap size of Sample 1 was 22 nm. A constant bias of 100 mV was applied between the metal tips during evaporation. The threshold current was set to 20 pA which means a $5 \text{ G}\Omega$ tunnel junction resistance was targeted. The gold deposition rate was kept low at 1 \AA/s to sustain a better control over the halting instance when the nanogap is formed. The evaporation was performed in steps of 10 nm to avoid the over-heating of the sample. The sample was waited to cool-down to room temperature after each evaporation step. The evaporation was immediately halted when the preset threshold current was reached in the 8th evaporation step. At the end of the experiment, the total thickness of gold coated was 78 nm. The swelling at the sides is approximately 1/7 for this sample. The pressure was 4×10^{-6} mBar before the experiment and it did not rise significantly during evaporations since the deposition was carried at low rate and for short durations. The maximum temperature reached during the whole process was 75°C. The SEM images of the sample before and after controlled thermal evaporation are given in Figure 5.5 and Figure 5.6, respectively.

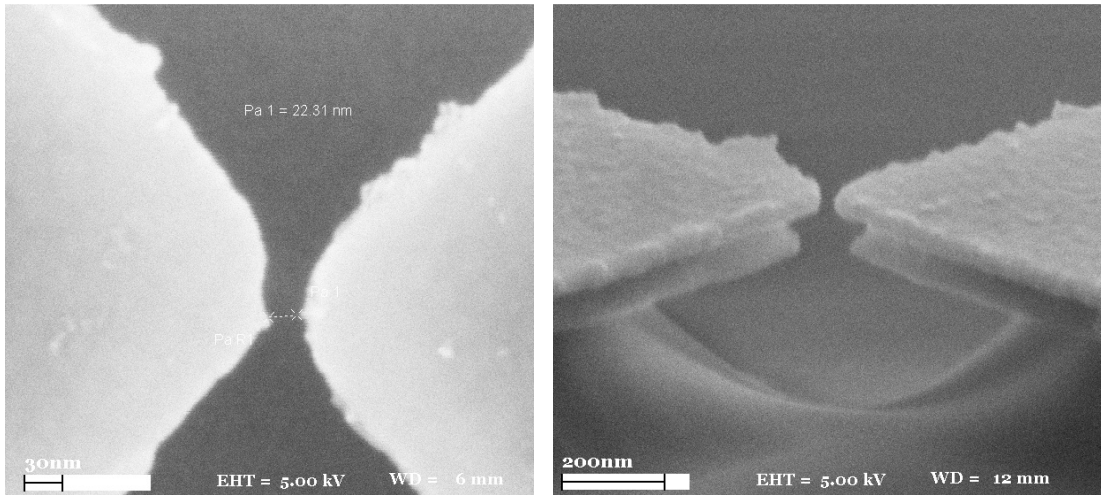
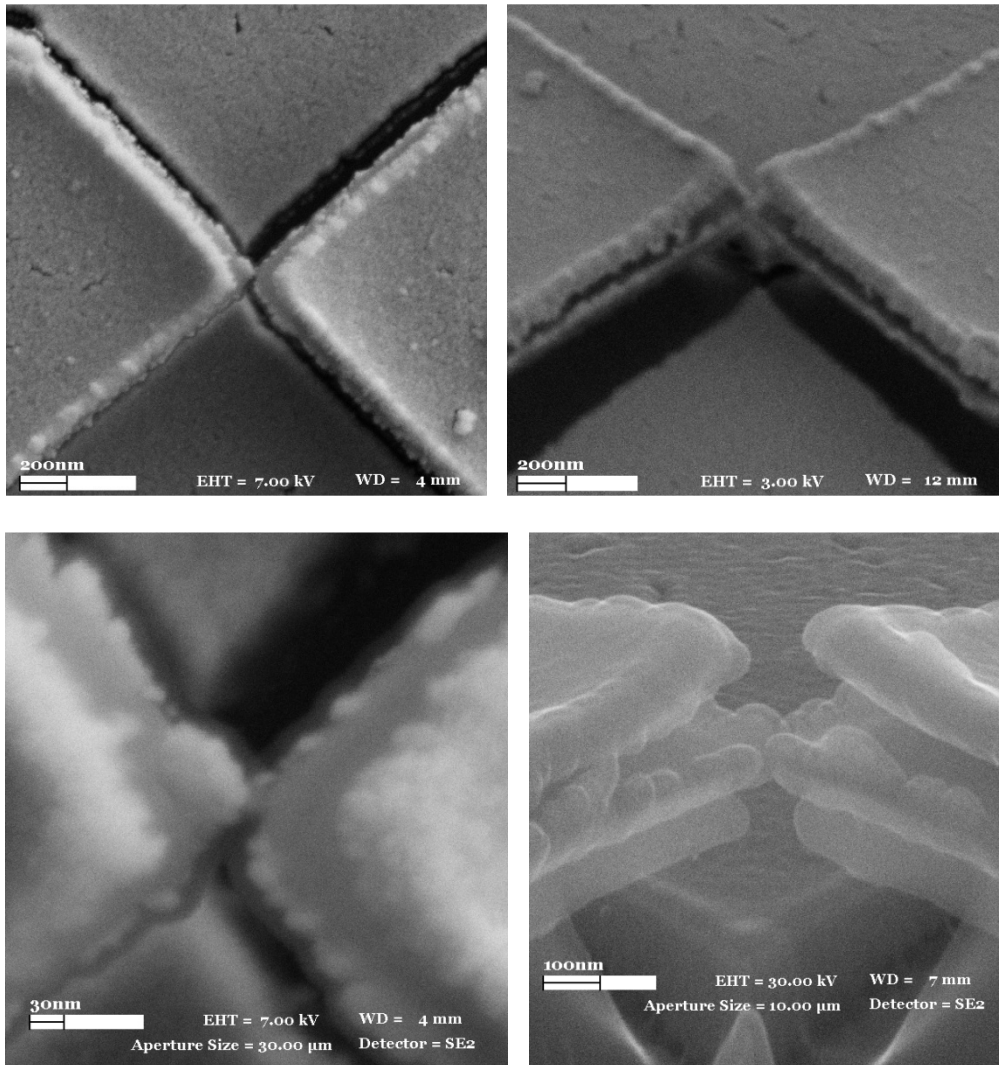


Figure 5.5: The top-view (left) and tilted (right) SEM images of Sample 1 before controlled thermal evaporation are given. The initial gap size of the device is 22 nm.



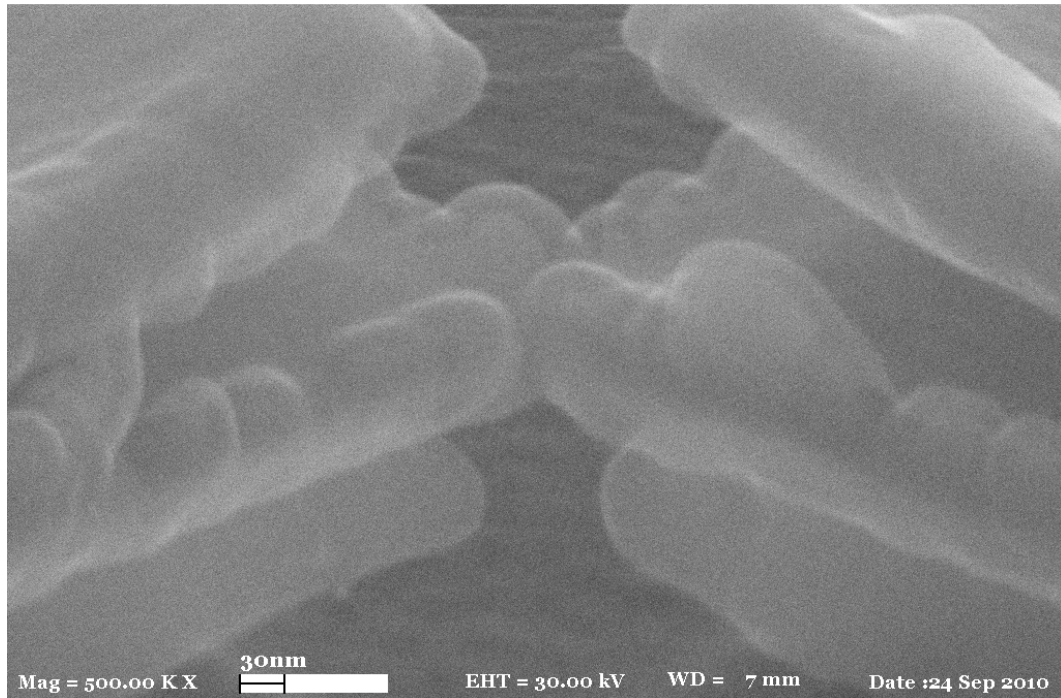


Figure 5.6: The SEM images taken at different magnifications and from different viewpoints are given. The gap size cannot be measured directly using SEM because of over 3 nm resolution of the microscope and three dimensional nature of the sample.

The gap size cannot be determined directly using SEM since the resolution of this imaging technique is not enough to measure sub-nanometer features. Besides, the three dimensional nature of the sample makes it inconceivable to specify the exact position and size of the nanogap. Even so, they nicely reveal the shrinkage of lithographically defined wide gaps as a result of thermal evaporation until they form a nanogap.

The SEM images after evaporation show that the gold thin film layers of the metal tips were curved up during evaporation and the nanogap was formed between the gold coated on the underlying chromium thin film. The device consists of multiple layers of oxide, nitride, chromium, gold with different thermal expansion coefficients and it went through multiple heat and cool cycles during the experiment. We think that the mismatch in the thermal expansion coefficients might have been exerted a stress on the gold layer and bended it. Therefore, the temperature must be kept as low as possible during experiments to minimize this thermal oriented stress.

The current versus time graphs during and after thermal evaporation are given in Figure 5.7. In the first graph, it is seen that when the measured current exceeded the preset threshold current of 20 pA, the evaporation was immediately halted. The system continued to measure the current for another 8 minutes after the evaporation to observe the behavior of the device while it was cooling down. The DC bias was 100 mV for both during and after evaporation measurements. The tunneling current increases from 20 pA to 250 pA in 8 minutes after evaporation. During this measurement, the device is cooled down to room temperature after evaporation and the metal tips might have approached to each other due to the change in the stress on thin films. As a result, the tunneling current increased when the tips came closer. The desired tunneling resistance was 5 G Ω according to the applied bias and preset threshold current but it decreased to 400 M Ω , 8 minutes after nanogap formation.

Sampling measurements were continued to follow the change in the tunneling current in time. Two tunneling current measurements were performed 1 hour and 16 hours after the experiment. The applied bias was 1 V for both cases and tunneling resistance versus time graphs are given in Figure 5.8. The tunneling resistance is calculated by dividing the applied bias by the measured tunneling current. After 1 hour, the resistance increased from 400 M Ω to around 4 G Ω which is close to the preset value. Then the resistance once again decreased to 2 G Ω after 16 hours and remained stable for the rest of the measurements. All in all, the resistance of the fabricated nanogap fluctuated for 16 hours until it stabilized. The tunneling current or the tunneling resistance also fluctuated randomly throughout the measurements. According to Simmons model, the tunneling current is affected by the gap size, potential barrier height, and the emission area for a given bias. Therefore, fluctuations in any of these parameters are reflected in the tunneling current. The gap size might fluctuate due to thermal stress and the mechanical vibrations coming from outside. The potential barrier height might be affected from the contaminations on the metal surface and in the gap which can change over time. The change in the atomic arrangement at the tip also affects the emission area and potential barrier height. Last but not least, there is relatively small external noise coming from the wiring and electrical measurement devices. In summary, the tunneling current can fluctuate due to multiple reasons but it is considered as a stable nanogap as long as it stays in the tunneling regime.

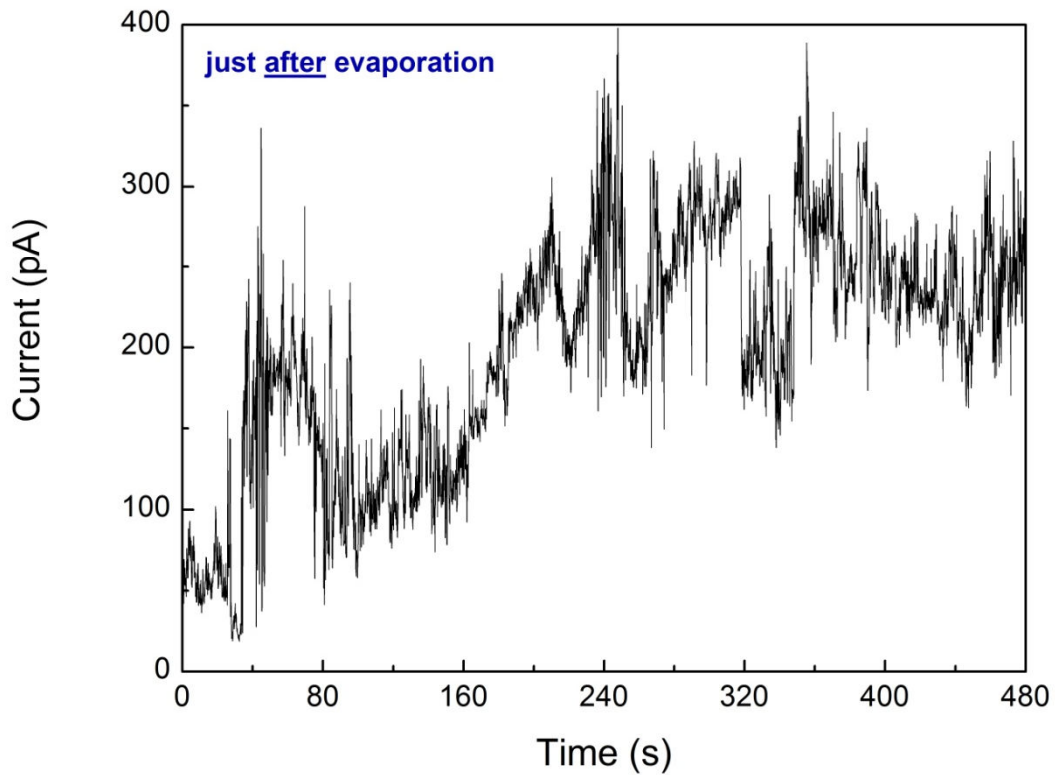
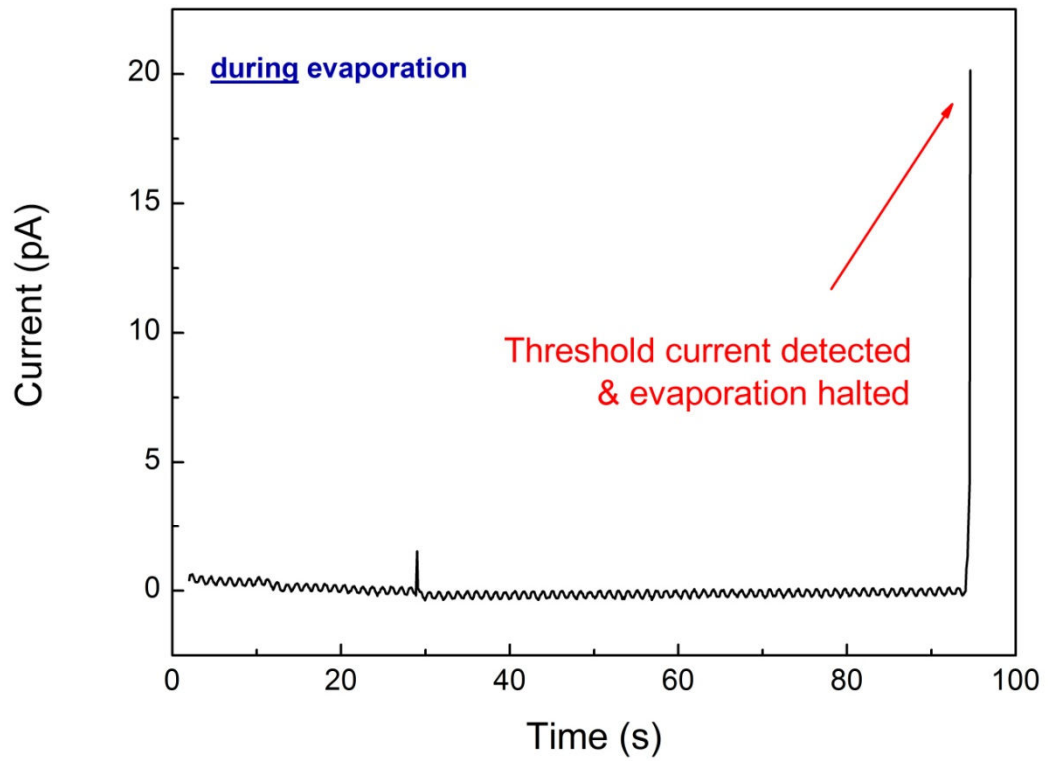


Figure 5.7: The time-current graphs of Sample 1 during (top) and just after (bottom) thermal evaporation are given. The sample was under constant bias of 100 mV for both graphs.

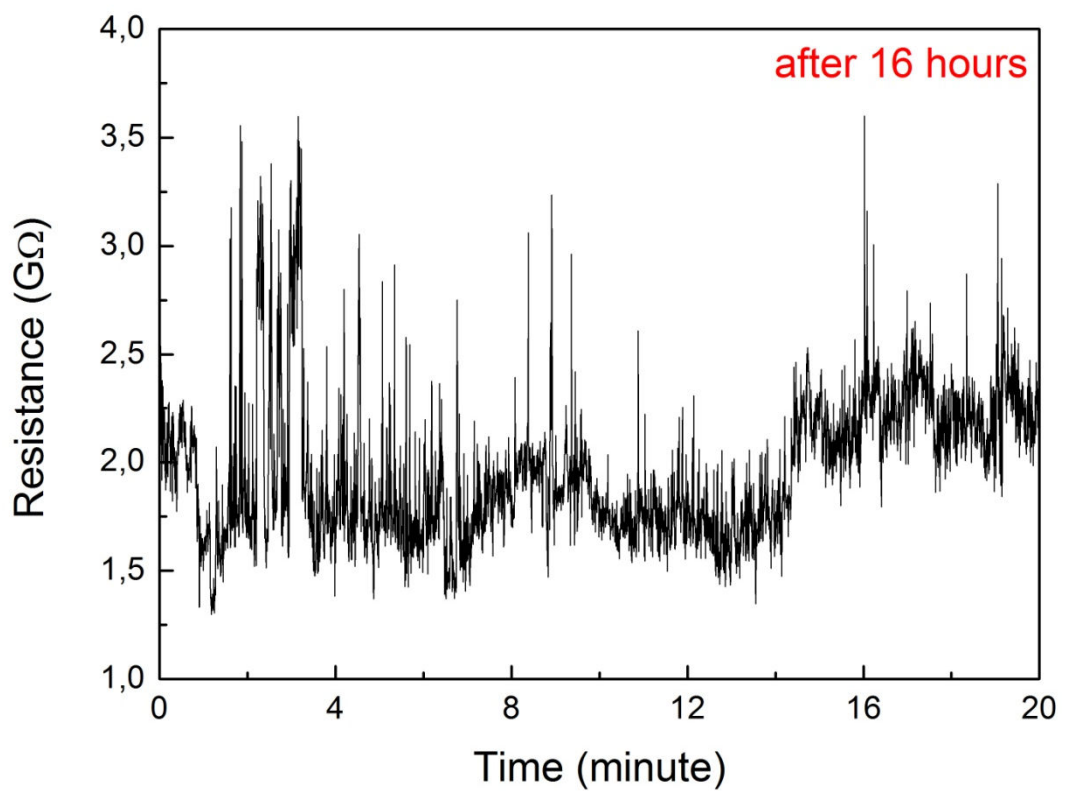
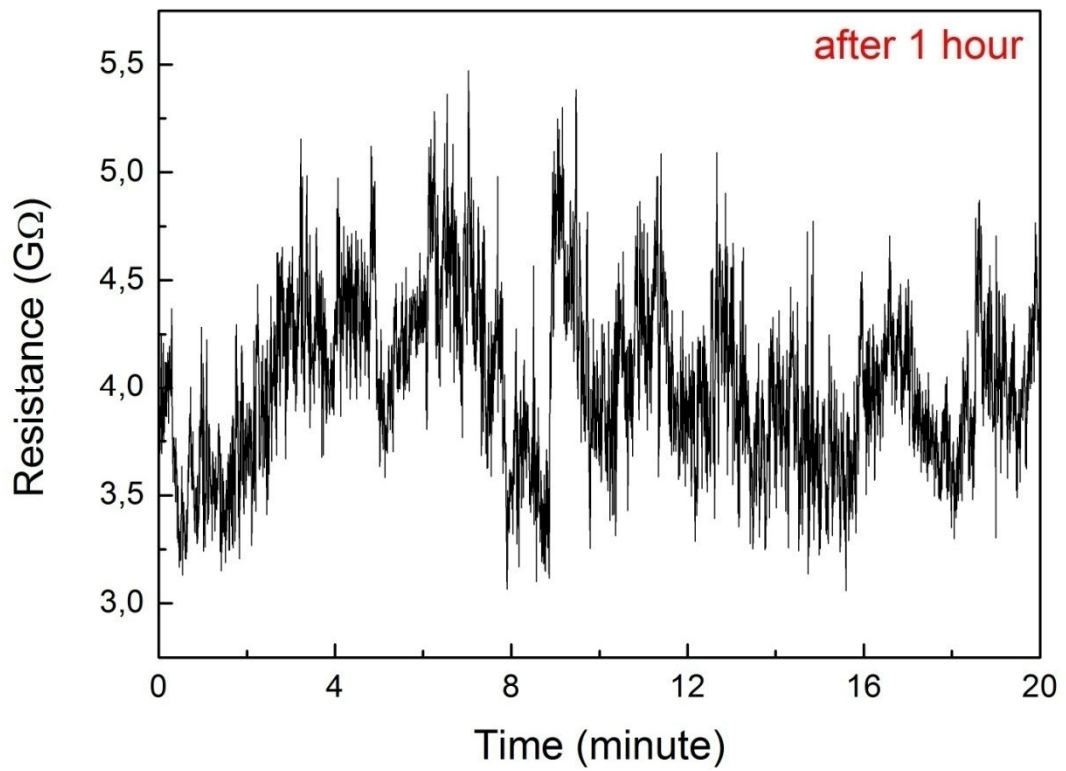


Figure 5.8: Tunneling resistance versus time graphs are given for 1 hour (top) and 16 hours (bottom) after nanogap formation. The applied bias was 1 V for both cases and the tunneling resistance was calculated by dividing the applied bias by the measured tunneling current.

Once the tunnel junction was stabilized, I-V measurements were performed to confirm and characterize the nanogap. In order to prove that the device was in the tunneling regime, the measured I-V characteristics of the device were fitted to the Simmons model ⁴⁷. As discussed in detail in Chapter 3, the device shows ohmic behavior when the applied bias is very small, i.e. $V \approx 0$ (Equation 3.3). The I-V curve given in Figure 5.9 is obtained by averaging 4 successive measurements to minimize the random noise and it is seen that the current changes linearly with applied bias as the model suggest for this interval.

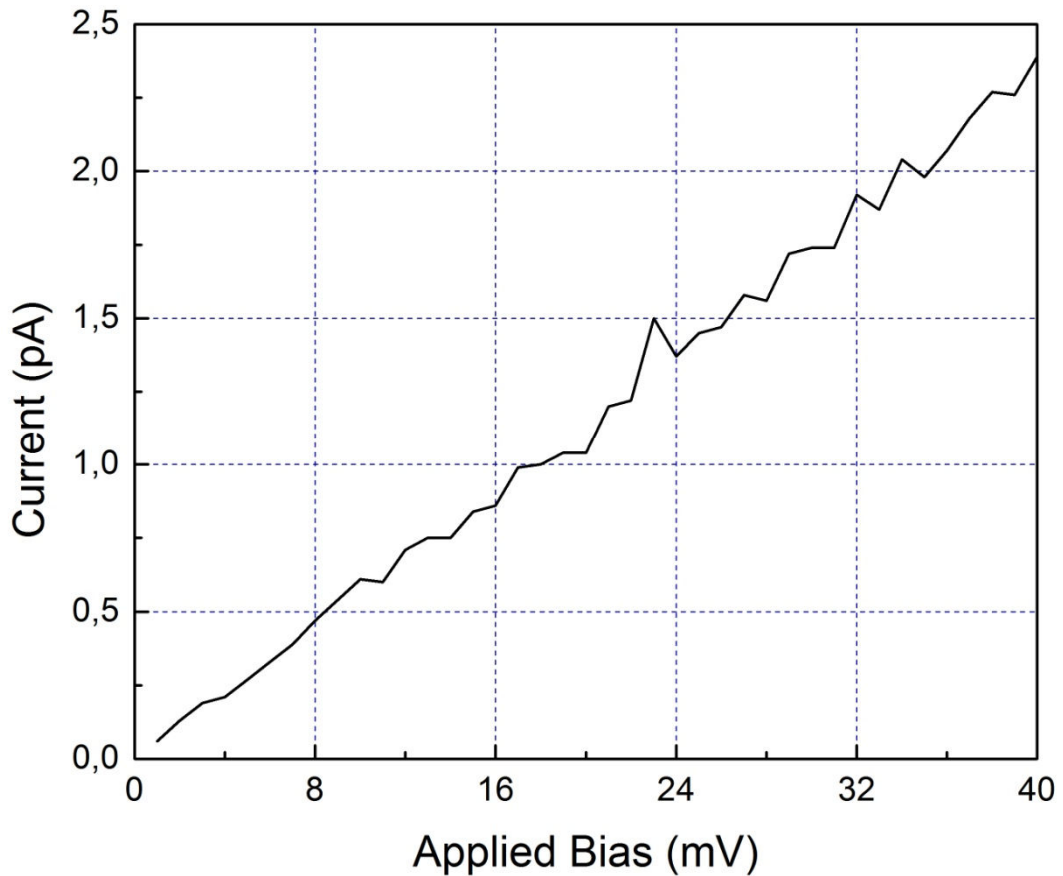


Figure 5.9: The I-V curve of Sample 1 for $V \ll \phi/e$ is given. The device exhibits ohmic behavior for extremely low biases as the Simmons' model suggests.

The most suitable interval of the model to fit the data and extract the tunnel junction parameters like gap size and potential barrier height is the intermediate-voltage range, $V < \phi/e$. The current density for this interval is given by Equation 3.4 and the tunneling current can easily be calculated by multiplying the current density by current emission area:

$$I = A \times J = \left(A \times \frac{6.16 \times 10^{10}}{s^2} \right) \times \left\{ \left(\phi - \frac{eV}{2} \right) \exp \left(-1.024s \sqrt{\phi - \frac{eV}{2}} \right) - \left(\phi + \frac{eV}{2} \right) \exp \left(-1.024s \sqrt{\phi + \frac{eV}{2}} \right) \right\}. \quad (5.1)$$

In this equation, I (A) is the tunneling current, J (A/cm²) is the current density, s (Å) is the gap width, V is the applied bias, ϕ (eV) is the height of the potential barrier between the electrodes, and A (cm²) is the current emission area. There are three unknown parameters to be extracted by fitting the experimental data to the Simmons' model: gap size, potential barrier height, and current emission area. If the current emission area, A is taken as a free parameter, it produces large errors and nonphysical results which imply an area smaller than a single atom. Same problem has been mentioned in similar previous works^{118, 120, 132}. As a solution, the emission is considered to be between the two closest atoms at the very end of the metal tips. In other words, the emission is taken only from a single atom and the emission area is equal to the cross-sectional area of the single atom. In this work the tunneling occurs between gold atoms and the radius of gold atom is 1.44 Å which gives an emission area of $A = \pi r^2 = 6.51 \times 10^{-16}$ cm². Therefore, there are only two parameters left to be extracted by fitting the experimental data to the theoretical model: s and ϕ .

The fitting was performed using Mathematica. Before fitting, data from 4 measurements were averaged to minimize the noise and the offset coming from the measurement unit was corrected. All the data were collected at room temperature and in air. A least square error minimization code was written to determine the appropriate initial values of the parameters. It is important to find the proper initial values before fitting, otherwise this complex nonlinear function might be stuck in a local minimum instead of the global minimum. The fitting algorithm was run using the initial values calculated by least square error minimization. The fitting algorithm calculated the gap size and the potential barrier height as $s = 9.260 \pm 0.038$ Å and $\phi = 1.050 \pm 0.009$ eV, respectively. These fitting results with low error values and the consistency of the data and the fitting curve as seen in Figure 5.10 proved that the fabricated device is compatible with the Simmons' model.

In theory, for a rectangular barrier, if the metal tips and the gap are completely free of contamination and the measurement is performed under absolute vacuum, the potential barrier height should be equal to the work function of the metal used. As the pressure increases, the particles on the metal surface and within the gap change the potential barrier shape and height. The effective potential barrier height decreases with the loss of vacuum. Previous STM measurements show that the potential barrier height between a gold metal tip and gold surface is around 1 eV in air¹³³. Therefore, the potential barrier height of $\phi = 1.05 \pm 0.009$ eV is compatible with literature values. During the measurements, the sweep interval is kept between -2.5 V and 2.5 V. Higher biases were avoided since ultra high electrical field might have ruined the device. Also, for voltages $V > 2\phi/e$, Equation 5.1 gives complex values which cannot be used in fitting.

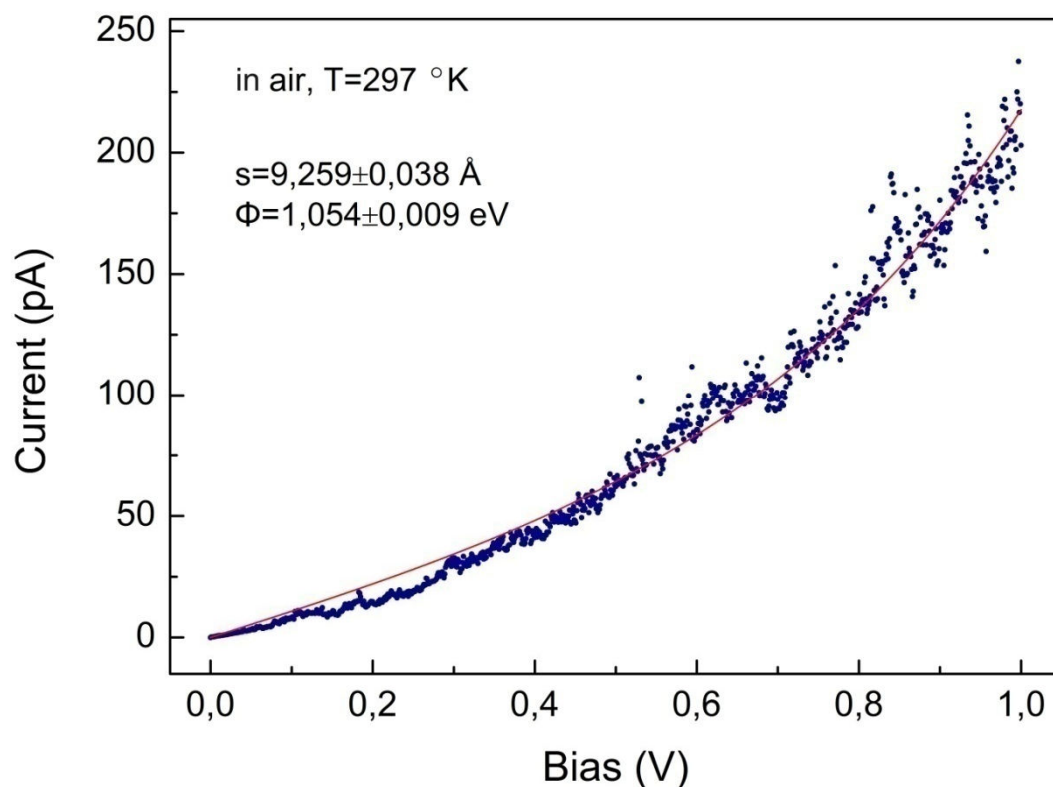


Figure 5.10: The experimental data (blue dots) and the curve obtained from fitting to the Simmons' model (red line) are given for intermediate voltages ($V < \phi/e$). The measurement is taken at room temperature, in air.

In addition to the model fitting, the device was also measured for opposite polarities to investigate the symmetry of the tunnel junction. As seen in Figure 5.11 the current values of Sample 1 are measured for biases between -2.5 V and 2.5 V. Even though, the general behavior of the device is similar for opposite polarities, the corresponding current values are slightly different for voltages with the same absolute values. When the polarity of the bias is reversed, the metal tip which acts as the electron emission source is also switched. The emission area and the potential barrier height might slightly change from tip to tip as a result of different atomic arrangement which results in these minor differences in the current values.

All in all, the small errors in ϕ and s and the consistency of the experimental data with the model prove that the fabricated device is a stable tunnel junction with subnanometer gap size. The extracted potential barrier height is compatible with the previous results in the literature and the device behaves in an expected manner for opposite polarities.

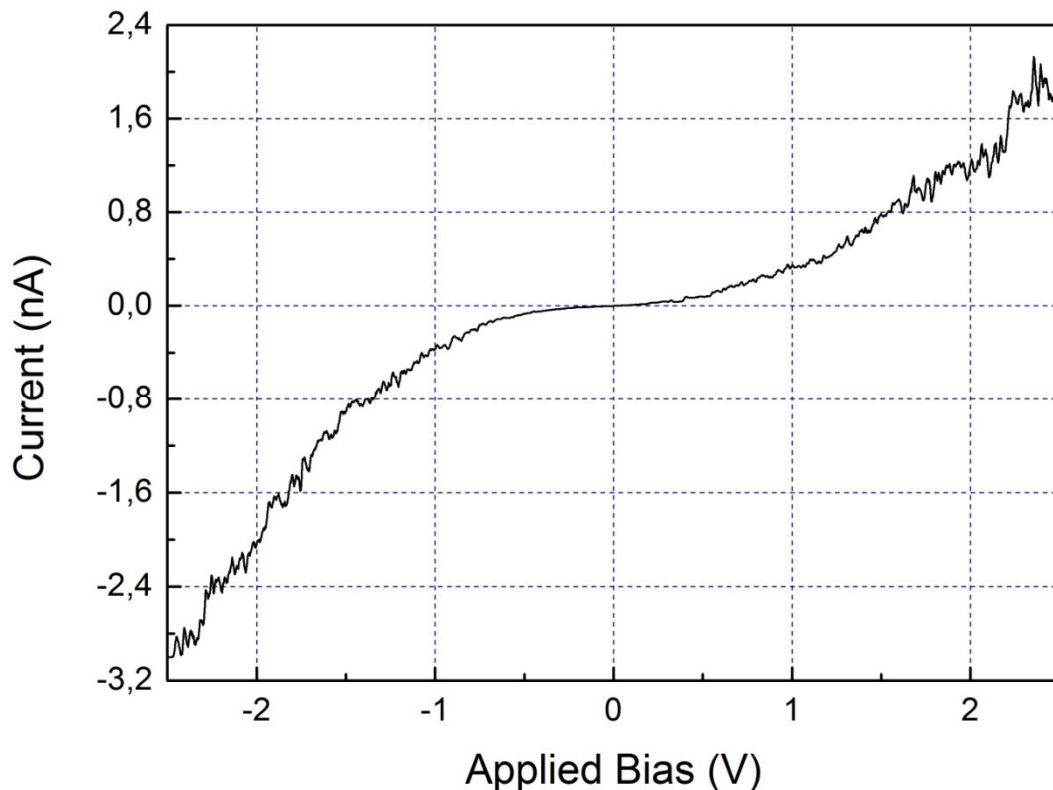


Figure 5.11: The voltage sweep measurement of Sample 1 for both negative and positive polarities is presented.

SAMPLE 2:

The second nanogap fabrication was performed on a tunnel junction-nanobeam embedded system and the initial gap size was 27 nm. The threshold current was set to 15 pA and a constant bias of 2 V was applied between the metal tips during evaporation. Thus, a tunnel junction resistance of ~ 1.33 T Ω was targeted in this experiment. A higher DC bias was preferred compared to the first sample to obtain a higher tunneling resistance. The first three evaporation steps were performed at higher rates (3-5 $\text{\AA}/\text{s}$) for higher thicknesses (20 nm) since the tunneling junction was unlikely to be formed at this point. The rest of the evaporation was carried out in 5 nm steps with lower deposition rate (1 $\text{\AA}/\text{s}$) to avoid the overheating of the sample and to be able to stop the evaporation instantly when the junction is formed. Just like Sample 1, Sample 2 was waited to cool-down to room temperature after each evaporation step. The preset threshold current was reached when the total thickness of gold coated was 120 nm and the evaporation was automatically halted at this instant. The swelling at the sides is approximately 1/9 for this sample. The pressure was 1.2×10^{-6} mBar during evaporation. The maximum temperature reached throughout the whole process was 53°C. The SEM images of the sample before and after controlled thermal evaporation are given in Figure 5.12 and Figure 5.13, respectively.

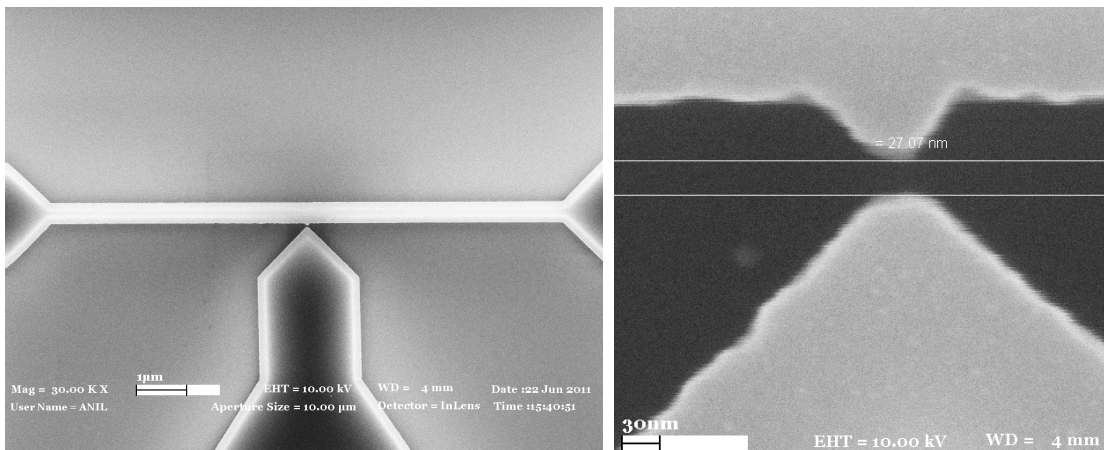


Figure 5.12: The top-view SEM images of Sample 2 at different magnifications are presented. Sample 2 is a tunnel junction-nanobeam embedded system (left) and the initial gap size is 27 nm (right).

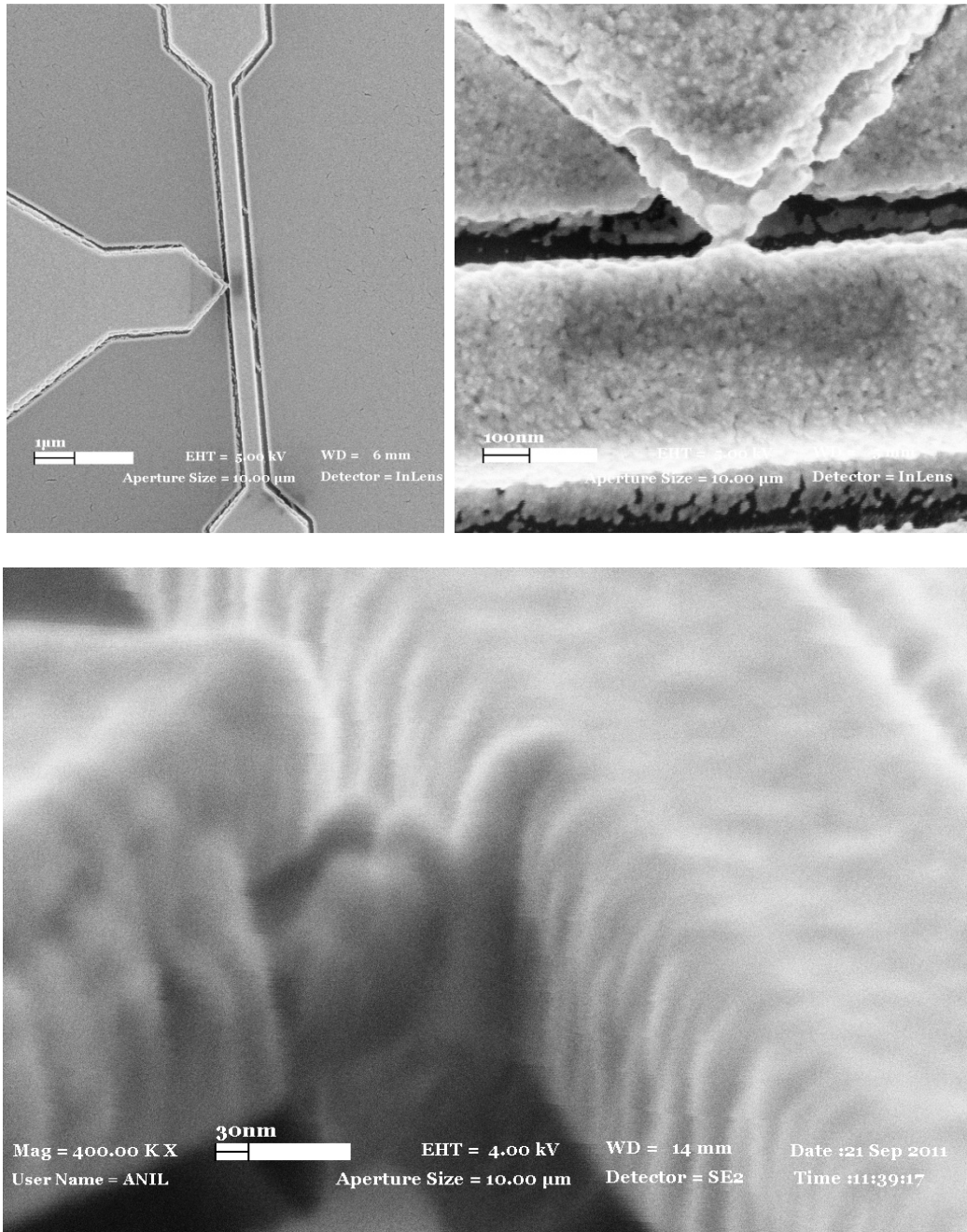


Figure 5.13: The SEM images of Sample 2 taken after controlled thermal evaporation are shown for different magnifications and viewpoints.

As seen in Figure 5.13, The SEM images taken after the experiment can not reveal the exact gap size because of the inadequate resolution and three dimensional structure. Just like Sample 1, gold thin film layers of the metal tips were curved up during evaporation as a result of thermal oriented stress. The curving was less pronounced in Sample 2 since the maximum temperature reached during the whole process was lower than the first one.

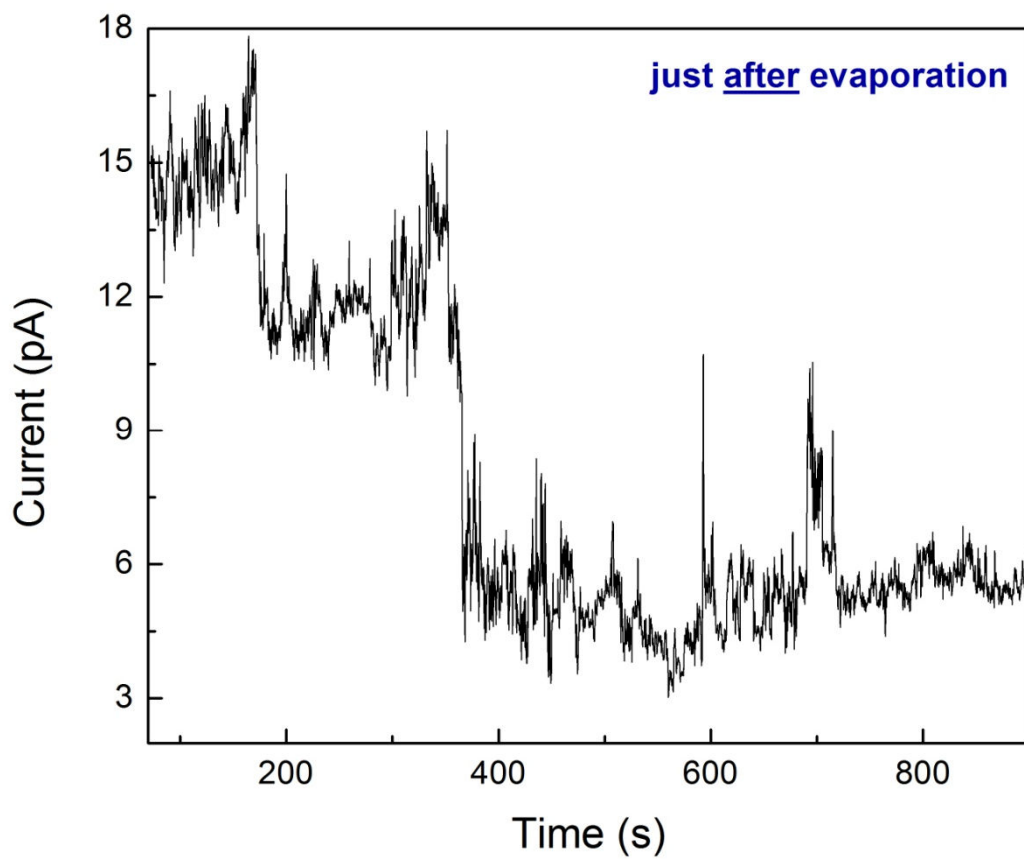
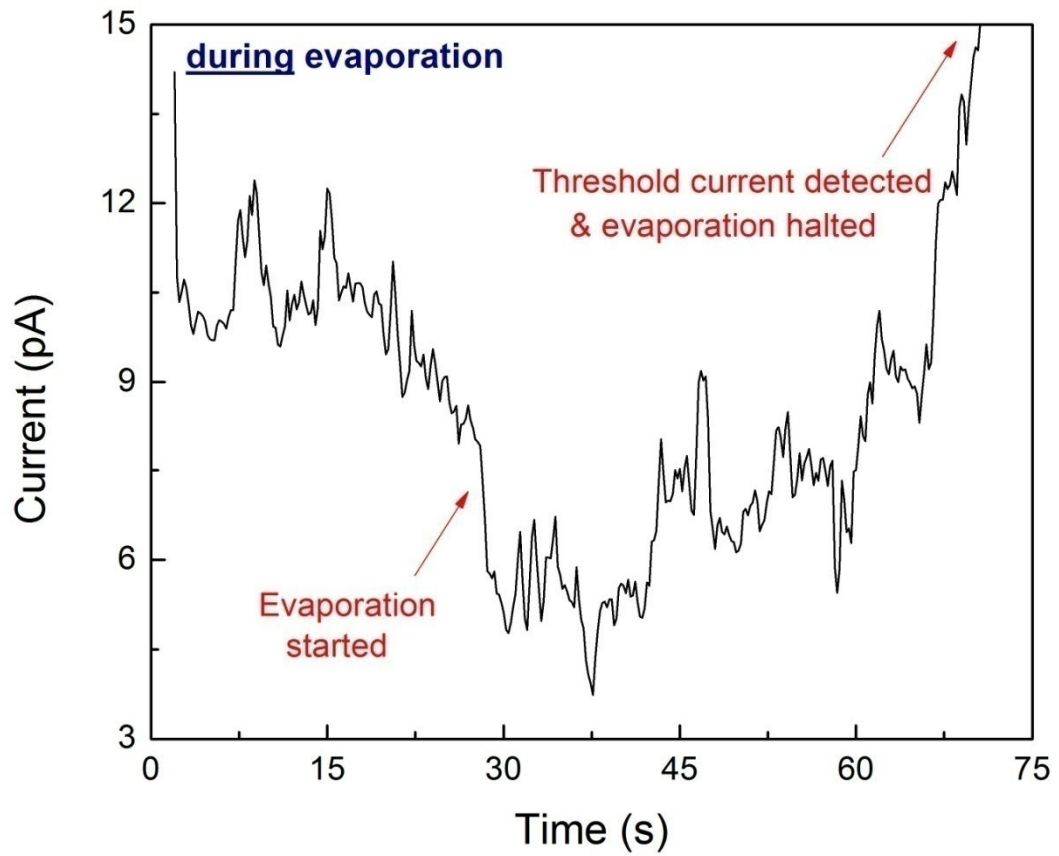


Figure 5.14: The time-current graphs of Sample 2 during (top) and just after (bottom) thermal evaporation are given.

The I-V graphs of Sample 2 during and after thermal evaporation are given in Figure 5.14. In the first graph, the tunneling current is increased slowly with time as the evaporation proceeded and the evaporation was halted as soon as the measured current exceeded the preset threshold current of 15 pA. While the device was cooling down to room temperature after the experiment, the system continued to measure the tunneling current for another 15 minutes. The tunneling current decreased from 15 pA to around 4-5 pA at the end of the measurement. The decrement occurred in a discrete manner which suggested that the gap size increased in abrupt steps as a result of the cooling of the device and the atomic rearrangement under high electrical field.

The sweep measurements were taken to characterize Sample 2, once the tunneling current was stabilized. This time, the measurements were carried at two different vacuum values of $P = 3 \times 10^{-1}$ mBar and $P = 3 \times 10^{-6}$ mBar. The mathematical procedure explained for Sample 1 was exactly used for Sample 2 to find the best-fitting curve. Because of the reasons mentioned previously, the emission area was assumed to be the cross-sectional area of a single gold atom ($A = \pi r^2 = 6.51 \times 10^{-16}$ cm²). The free parameters of ϕ and s were extracted by fitting the experimental data to Equation 5.1. The effective barrier height and the gap size are calculated as $\phi = 3.983 \pm 0.039$ eV and $s = 9.878 \pm 0.087$ Å for $P = 3 \times 10^{-1}$ mBar and $\phi = 3.917 \pm 0.033$ eV and $s = 9.540 \pm 0.071$ Å for $P = 3 \times 10^{-6}$ mBar. The experimental data and the curves obtained by fitting to Simmons' model are given in Figure 5.15 for both pressure values. Once again, the small error values in the extracted parameters and visual coherence between the experimental data and fitting curve prove that the fabricated device is a stable tunnel junction with subnanometer gap size.

The calculated potential barrier heights are similar for two different pressure values. These results suggest that ϕ does not depend on the pressure of the environment. On the other hand, theoretically the effective potential barrier height should decrease with increasing pressure. There are other factors that affect the potential barrier height like the shape of the barrier and the chemical purity of the metal tips and the gap¹³⁴⁻¹³⁷. Numerous controlled measurements have to be performed on a large number of tunnel junctions to understand the role of environment pressure on the effective potential barrier height.

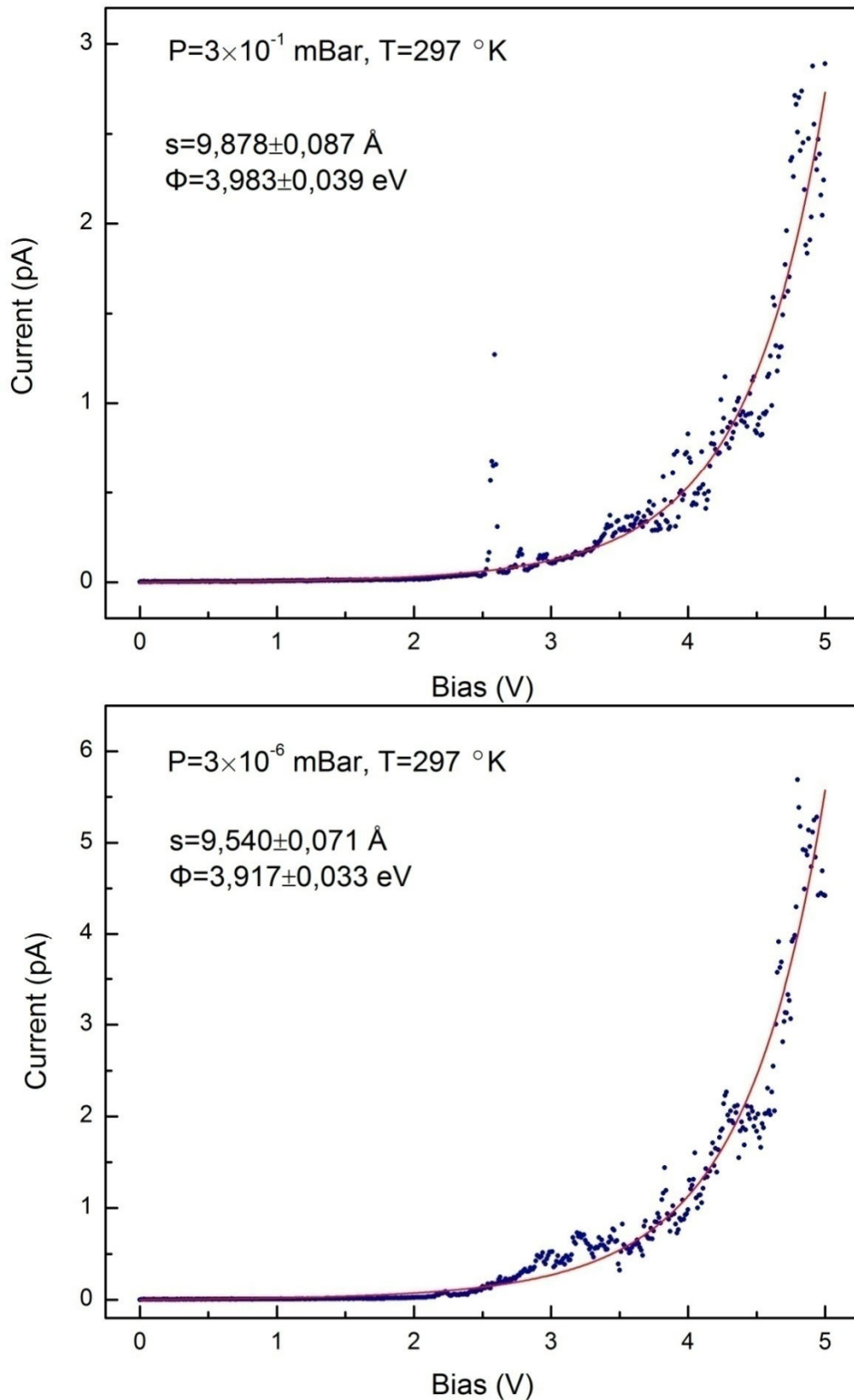


Figure 5.15: The experimental data (blue dots) and the fitting curves (red line) are given for intermediate voltages ($V < \varphi/e$). The measurements were performed at room temperature for pressures, $P = 3 \times 10^{-1} \text{ mBar}$ (top) and $P = 3 \times 10^{-6} \text{ mBar}$ (top).

The sweep measurements were repeated nine times in a 50 hour-period in order to test stability of fabricated tunnel junction. All the I-V measurements were fitted to the Simmons' model. The extracted potential barrier heights (ϕ) and the gap sizes (s) are presented in Figure 5.16. The error bars represent the error values in the extracted parameters. As seen from the graphs, the potential barrier height varies between 3.5 and 4.5 eV and the gap size varies between 8 and 12 Å for 50 hours. The two graphs indicate a correlation between the gap size and the potential barrier height since one parameter increases while the other one decreases and vice versa. In order to better understand the correlation between the two free parameters, the barrier height is taken as $\phi = 3.89$ eV for all set of curves and the data is fit to Equation 5.1 with the only free parameter s . The fixed value of ϕ is calculated by averaging the potential barrier heights given in Figure 5.16. The gap size over 50-hour period is calculated using free and fixed ϕ and the results are compared in Figure 5.17. The gap size varies between 9 and 11 Å when potential barrier height is fixed.

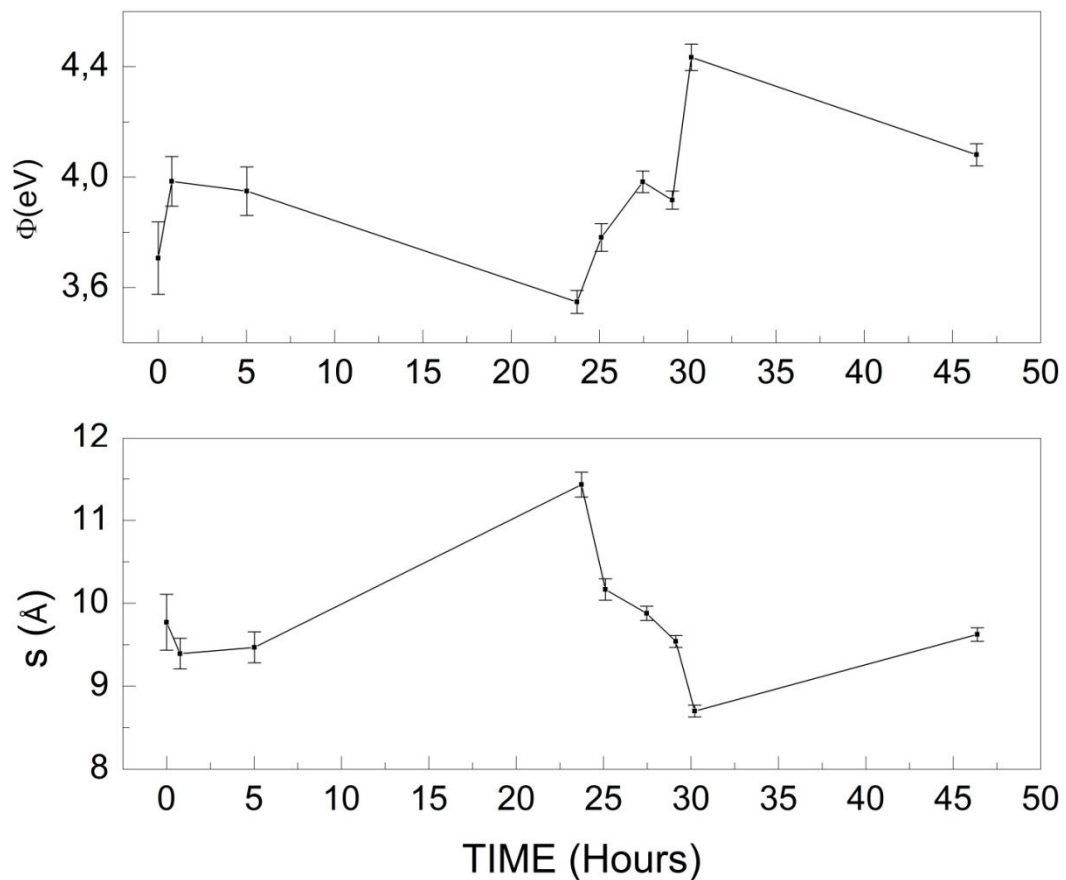


Figure 5.16: The potential barrier heights (top) and the gap sizes (bottom) with corresponding error values were obtained for nine measurements taken at different times in a 50 hour-period.

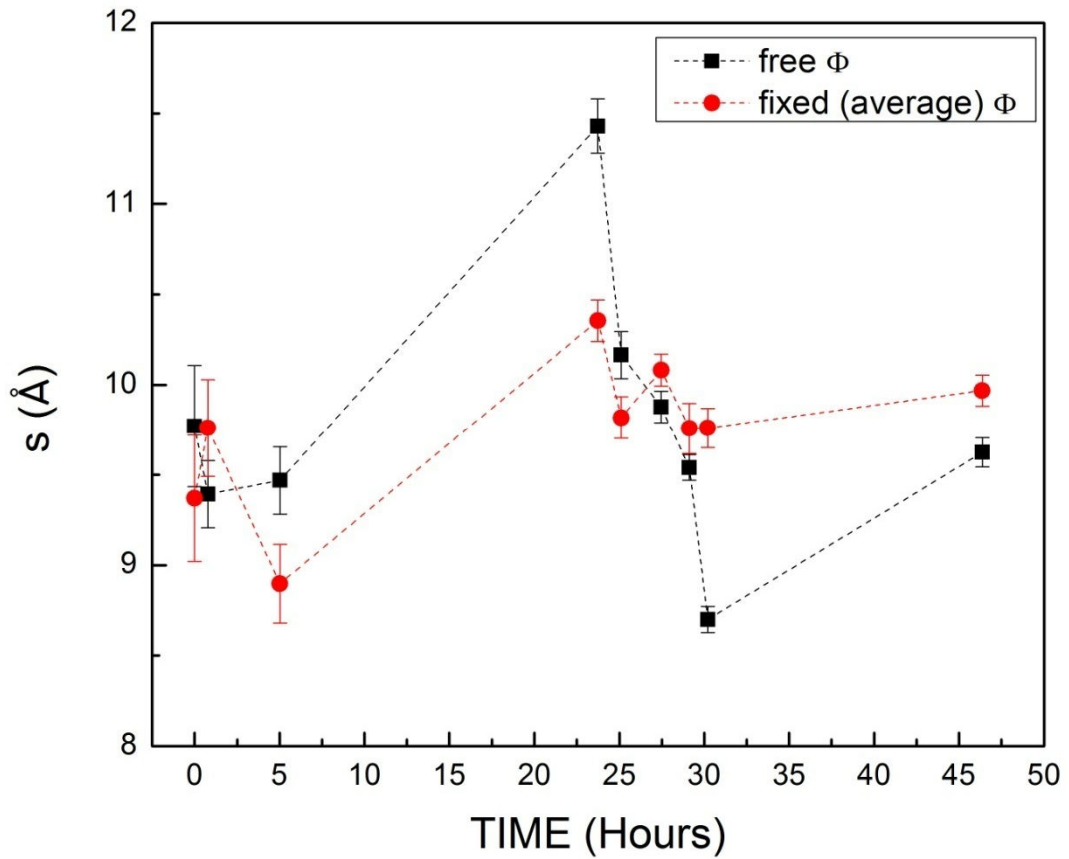


Figure 5.17: The gap separation with corresponding error values over 50 hours time is calculated by taking potential barrier height, ϕ , as a free parameter (black squares) and as a fixed parameter of 3.89 eV (red circles).

All in all, both parameters remain in a reasonable interval and do not change significantly over time. These measurements prove that the fabricated device has high stability and can operate in the tunneling regime for more than 2 days. On the whole, a stable subnanometer size tunnel junction has successfully been fabricated on Sample 2 using controlled thermal evaporation. The fitting curves and the extracted parameters with small error values prove that the device is compatible with the Simmons' model.

SAMPLE 3:

Two metal tips which were initially 35 nm apart were used for the third nanogap fabrication experiment. A constant bias of 100 mV was applied between the metal electrodes and the threshold current was set to 10 pA. The targeted tunnel junction resistance was 10 G Ω for this sample. 30 nm thick depositions at 3 $\text{\AA}/\text{s}$ rate were performed for the first three evaporation steps. The rest of the evaporation was carried out in 10 nm steps with 1 $\text{\AA}/\text{s}$ deposition rate. Just like the previous experiments, the sample was cooled down to room temperature after each evaporation step. The evaporation was halted as soon as the measured current exceeded the pre-set threshold current. A total of 130 nm gold had been coated at the time the deposition stopped. The swelling at the sides is approximately 1/7 for this sample. The pressure was on the order of 10^{-7} mBar during evaporation. The maximum temperature reached throughout the whole process was 45°C and when the deposition halted in the last cycle the temperature was 28°C. The SEM images of the sample before and after controlled thermal evaporation are given in Figure 5.18 and Figure 5.19, respectively. The SEM images in Figure 5.19 reveal that two small grains at the tip ends were grown to close the gap and formed the tunneling junction. In contrast to previous samples, the metal layers did not curve up during this experiment. Although the scanning electron microscope cannot resolve the gap, views from various angles verify sub-resolution separation of less than 5 nm.

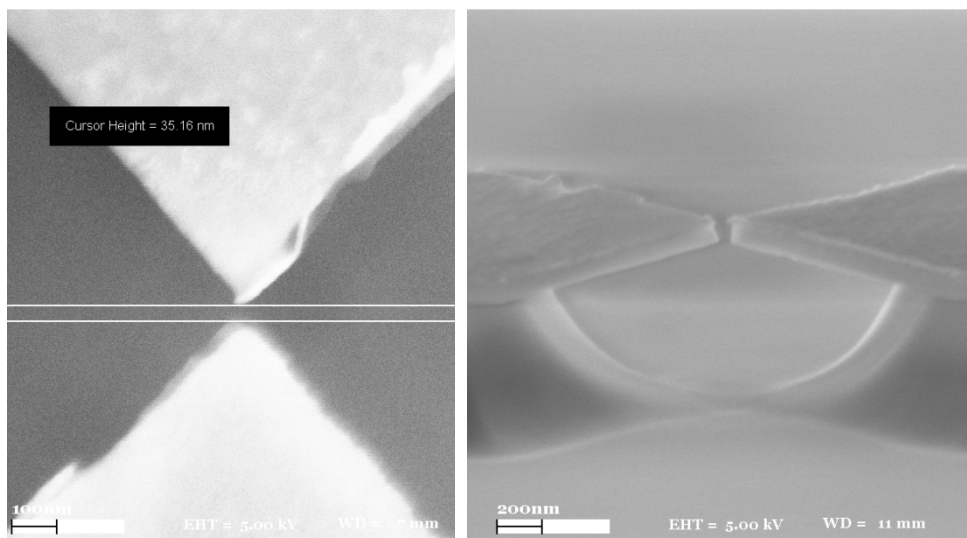


Figure 5.18: The top-view (left) and tilted (right) SEM images of Sample 3 before controlled thermal evaporation are given. The initial gap size of the device is 35 nm.

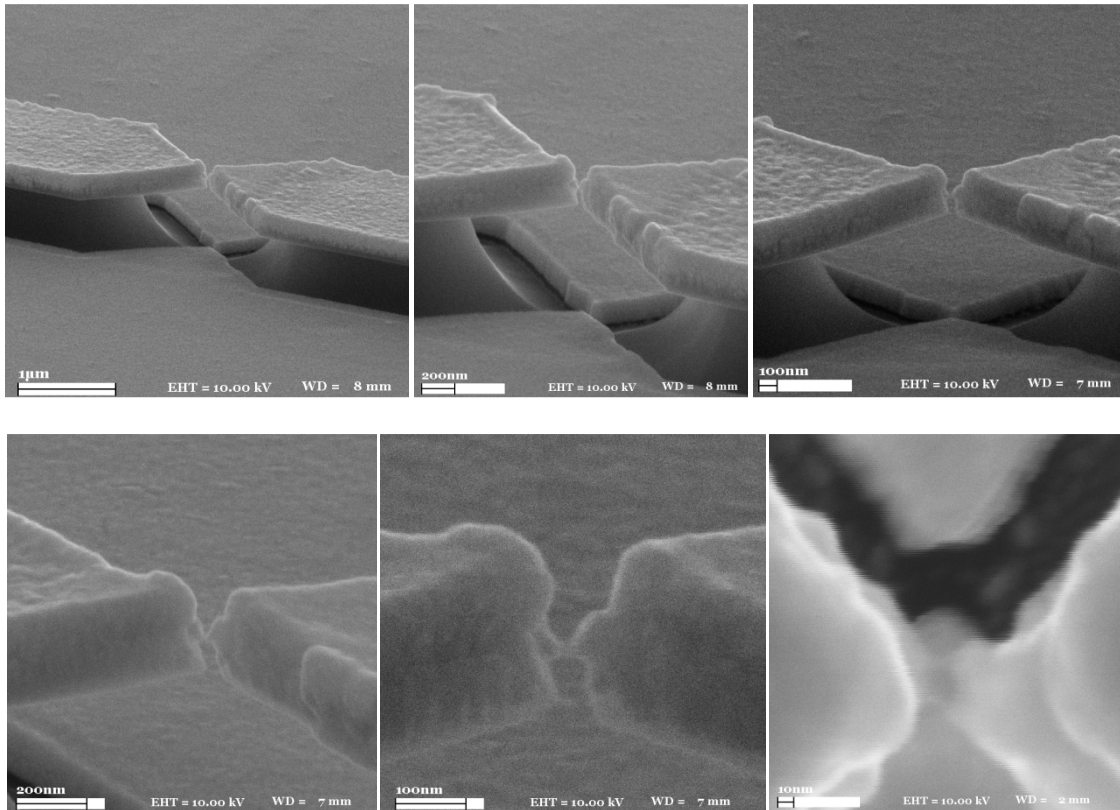


Figure 5.19: The SEM images of Sample 3 after controlled thermal evaporation are presented for various magnifications, from different viewing angles.

The current values during and after in-situ controlled thermal evaporation are shown in Figure 5.20. There are minor fluctuations in current before the 10 pA threshold is reached. This is possibly due to atom dynamics at the tip ends which result in momentary jumps in the gap conductance. However once the threshold was reached, the junction was formed irreversibly. The measurement was continued for another 15 minutes after evaporation but, the current exceeded the preset compliance level of the parameter analyzer (100 pA) and could not be measured correctly after 70 seconds. Therefore only the first 70 seconds after the evaporation is included in the graph. The increase in the tunneling current after the experiment might originate from thermal relaxation of the device or the atomic rearrangement at the metal tip ends. Despite the increase in the tunneling current and the fluctuations, further sampling measurements with higher compliance levels showed that the device was stabilized in a short while and remained in tunneling regime.

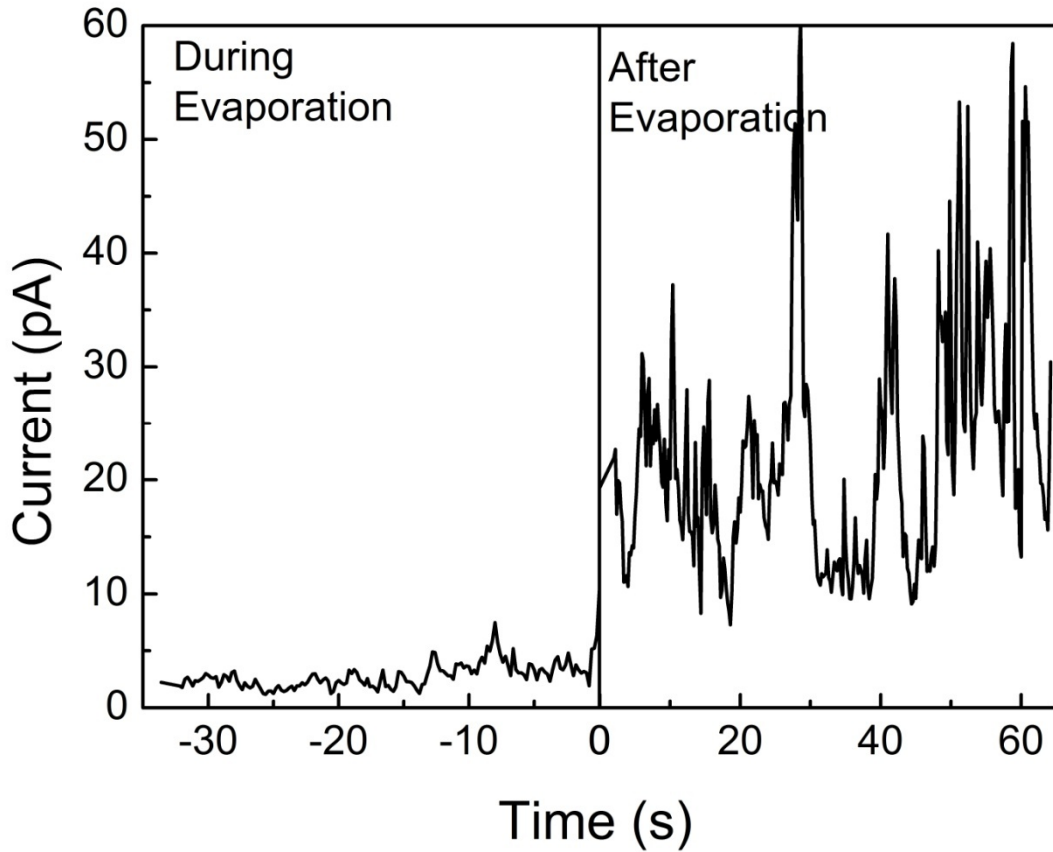


Figure 5.20: The graph shows the progress of the current flow between the electrodes before and after controlled thermal evaporation.

When the tunnel junction became stable, the sample was characterized using its current-voltage measurements. The I-V measurements were repetitively recorded over days and in spite of the fluctuations the overall behavior remained stable. The sweep measurements were performed in air, at room temperature. Once again, the I-V characteristics were analyzed by Simmons' model to be able to estimate the gap separation and the potential barrier height. Assuming that the tunneling current flows through the single atom at the tip end, the area is taken as $A = \pi r^2 = 6.51 \times 10^{-16} \text{ cm}^2$. On the other hand, s and φ are the parameters to be interrogated from the experimental data by fitting it to Equation 5.1 for intermediate voltages ($V < \varphi/e$). According to the best fit curve to the measurement (Figure 5.21), the potential barrier height is calculated to be $\varphi = 0.770 \text{ eV}$ while the gap width is $s = 11.32 \text{ \AA}$ with standard errors of 0.005 eV and 0.05 \AA respectively. The potential barrier height of Sample 3 is consistent with the results of Sample 1 and the previous studies in literature¹³³.

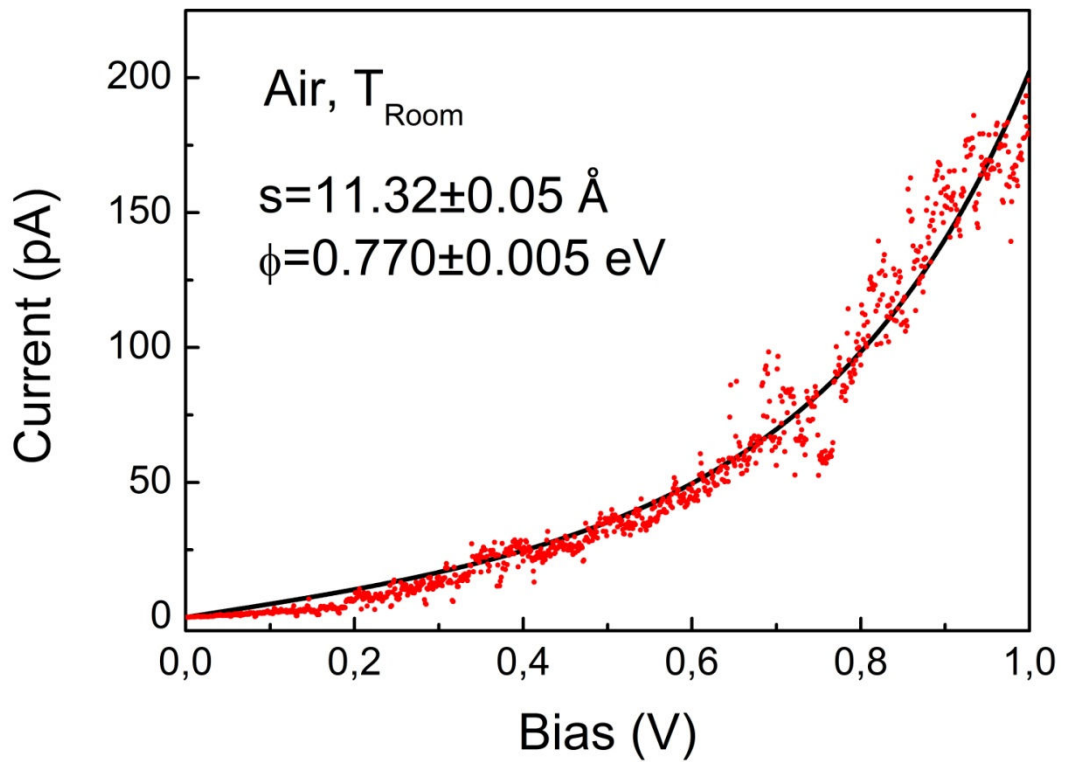


Figure 5.21: Red dots represent the measured current versus voltage characteristics of Sample 3 and the black line is the fitted curve to Simmons' model. The measurements were performed at room temperature, in atmospheric pressure.

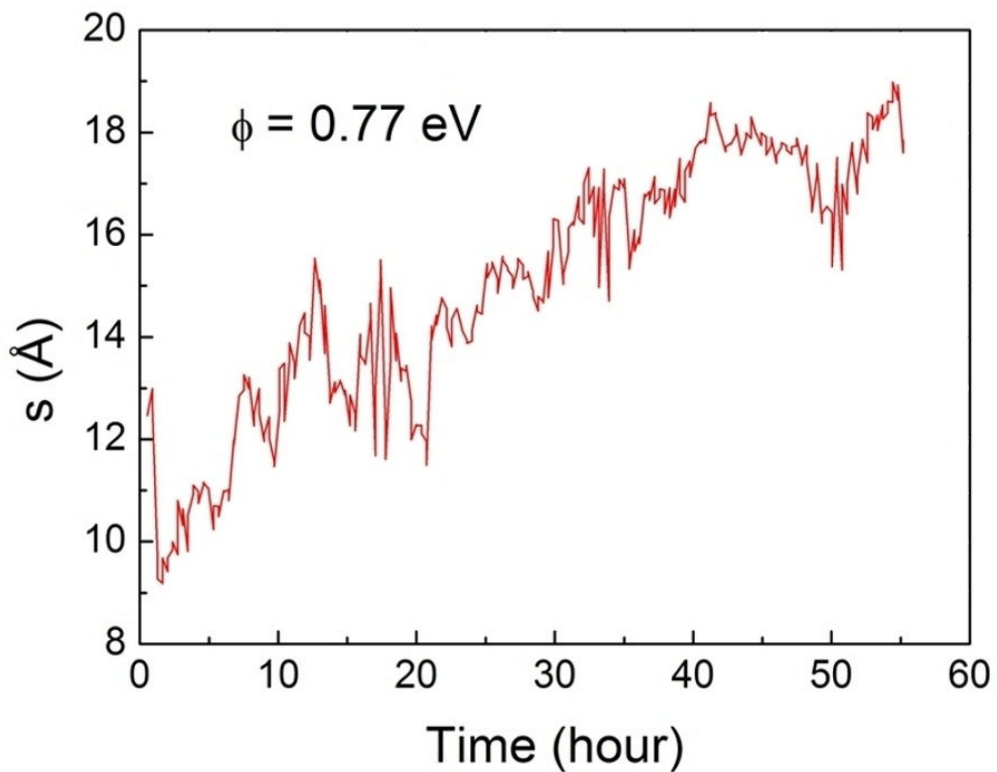


Figure 5.22: The variation of the calculated gap separation, s , over 55 hours time is given. The potential barrier height, ϕ , is taken as 0.77 eV.

The results of the fitting to the curves taken from the same sample over the period of two days gave similar results. In order to see the stability of gap size, the barrier height is taken as $\phi = 0.770$ eV for all these set of curves and the data is fit to Equation 5.1 with the only free parameter s . Graph in Figure 5.22 shows the variation of the calculated gap separation, s , over 55 hours time. It is observed that s tend to fluctuate with an amplitude of ~ 1 Å in between adjacent measurements. Sample 3 remained in the tunneling regime over 4 weeks.

5.4 Discussions and Conclusion

Three samples have successfully been fabricated using in-situ controlled thermal evaporation. The details of the fabrication technique and the home-made experimental setup are discussed thoroughly. The samples are observed, analyzed and characterized by using high resolution SEM images and electrical measurements. The procedure of fitting of the experimental data to the theoretical model (Simmons' model) is explained in detail and the extracted tunnel junction parameters are provided. Further sweep and sampling measurements have proven that all the fabricated nanogaps are stable. The summary of the results of three samples is given in Table 5.1.

Table 5.1. Summary of the important process parameters and resulting junction parameters from controlled fabrication of three different samples are given.

	Initial gap (nm)	Deposited gold thickness (Å)	Fitting Pressure (mBar)	s (Å)	ϕ (eV)
Sample 1	22	78	atmospheric	9.3	1.1
Sample 2	27	120	3×10^{-1}	9.9	4
			3×10^{-6}	9.5	3.9
Sample 3	25	130	atmospheric	11.3	0.8

For all three samples, the deposition rate was 1 Å/s in the last cycle when the tunnel junction was formed. This rate is small enough to easily control the average filling in the gap. The response of the thermal evaporator is sufficient to stop the gap narrowing with < 1 Å resolution. In all samples, there were fluctuations and minor jumps in the tunneling current during and after the deposition. According to the Simmons' Model, the tunneling current is affected by three parameters: gap size, potential barrier height and emission area. The variations in any of these parameters are reflected in the tunneling current as fluctuations and jumps:

1. **Gap Size:** The gap size changes when the distance between the very ends of the metal tips change. The high electrical field between the tips ($> 10^8$ V/m) might result in atomic rearrangements at the metal tip ends which ultimately changes the gap size and causes discrete and sudden jumps in the tunneling current. The gap size might also change when the tips move towards or away from each other as a result of the contraction or relaxation in any of the layers of the device (silicon, oxide, nitride and metal layers). The contraction/relaxation can occur as a result of the thermally oriented stresses on the sample and the mechanical vibrations coming from outside.
2. **Potential Barrier Height:** The potential barrier height depends on the Fermi energy level of the metal electrodes and the vacuum condition in the gap. Therefore, the chemical composition and purity of the metal tips and the gap affects the effective potential barrier height and hence the tunneling current. The contaminations on the metal tips and inside the gap continuously changes in time and causes fluctuations in the tunneling current. Even though, an ideally square potential barrier shape is assumed in Simmons' model, in reality the changes in the potential barrier shape also affect the tunneling current.
3. **Emission Area:** Throughout the fittings the emission area is assumed to be the cross-sectional area of a single atom since the tunneling occurs between the two closest atoms. Therefore, the emission area can be assumed to remain unchanged.

Despite the fluctuations and jumps in the tunneling current, once the threshold current is exceeded, the tunnel junction is formed irreversibly and remains in the tunneling regime. The fabricated junctions are very robust against handling and pressure changes and have lifetime over weeks.

The I-V curves of the fabricated nanogaps were fitted to the Simmons' model which is the most widely-used theoretical model in similar works in literature ^{120, 132}. The two important device characteristics, ϕ and s , were deduced by fitting the experimental data to the model. The small error values in ϕ and s , and the visual inspection of fitted curve to the experimental data prove that the fabricated devices operate in tunneling regime. The gap sizes are calculated to be approximately 1 nm which is a typical value for tunnel junctions. The effective barrier heights of Sample 1 and Sample 3 are calculated for atmospheric pressures and the results are consistent with the previous studies ¹³³. The effective barrier height of Sample 2 is interrogated for two different vacuum values of 10^{-1} and 10^{-6} mBar. These measurements generated higher ϕ values compared to the atmospheric pressures as expected. However, there was no noteworthy difference between ϕ values for 10^{-1} and 10^{-6} mBar. The dependence of ϕ on vacuum condition can not be understood totally from these results and it needs further investigation with more samples.

Numerous experiments were performed on initially wider gaps (>40 nm) but none of them produced successful results. As mentioned before, the deposition thickness has to be higher for initially wider gaps. As a result, not only these samples go through more heat and cool cycles, but they also experience higher temperatures. These thermal effects can easily distort the shape of the metal tips and ruin the sample. Additionally, when the surface is coated with a thicker metal, the chance of an unwanted parallel conductance increases. Our experiments showed that, for nanogap fabrication, the initial gap size should be smaller than 40 nm before controlled thermal evaporation. On the other hand, most of the samples fabricated had a gap size over 100 nm due to the "widening of the gap size after release" problem. At this point, a new technique is developed to compensate the gap widening and to obtain initially narrow gaps. This technique will be discussed in the next chapter.

In conclusion, we have developed a fabrication method for the formation of nanogaps, using conventional lithography and in-situ controlled thermal evaporation. With this method, it is possible to fabricate nanogaps at a predetermined conductance and accordingly at a predetermined size. The fabricated devices are stable and robust and have lifetime over weeks. Even though, only nanogaps between gold electrodes are demonstrated in this study, any material compatible with thermal evaporation can be used for the fabrication of tunnel junctions.

CHAPTER 6

TUNING OF NANOGAP SIZE IN HIGH TENSILE STRESS THIN FILMS

6.1 Introduction

High tensile stress thin films are widely used for the fabrication of suspended nanomechanical structures since they offer higher quality factors and resonant frequencies^{43-46, 66, 67, 69}. Additionally, they are mechanically durable and stable and more resilient to the fabrication problems like stiction¹³⁸. On the other hand, the intrinsic high tensile stress cause shape distortions such as contracting, buckling and twisting, once the structures are released from the underlying layer. Even though there are some studies that actually utilize the shape deformation for the fabrication of 3D structures^{139,141}, it becomes problematic when the precise positioning of the suspended structures is desired. It is already mentioned in the previous chapter that the main issue with the fabrication of nanogaps using controlled thermal evaporation is the gap widening problem. The metal tips move apart from each other after wet etch as a result of the intrinsic high tensile stress of nitride thin film. The fabrication yield decreases dramatically since the over-wide gaps are not compatible with the controlled thermal evaporation method. Therefore, a new technique is developed with the motivation of compensating the gap widening and maintaining the original gap size after release. The chapter starts with a literature review on the use of high tensile stress thin films in nanomechanics with pros and cons. Examples from earlier studies that either utilize or compensate the effects of high tensile stress are introduced. Then, the implementation of the technique, geometrical design and the device fabrication procedures are given. Finally, the results of the experiments are presented by comparing before and after SEM images of the gap width and supporting the experimental data with FEA.

6.2 High-Stress Thin Films and Nanomechanics

The growing interest on NEMS over the last decades has been expressed in detail in Chapter 2. The primary component of NEMS is a suspended mechanical resonator with micro- and nano-dimensions. As a consequence of their diminished size, nanomechanical resonators have extremely small effective masses and very high fundamental resonant frequencies¹³. Owing to these unique properties, NEMS have been employed in numerous applications for the ultrafast and ultrasensitive detection of various physical properties such as mass, position, and charge^{3, 11-21, 60}. In addition, the extraordinary dynamical behavior of nanomechanical resonators arouses the interest of fundamental research in the context of energy dissipation and damping^{43, 44}.

The sensitivity of a NEMS detector is maximized by decreasing the mass as well as increasing the quality factor of the resonator. However, the experimental results show that the mechanical quality factor diminishes as the dimensions and hence the mass of a nanoresonator decrease¹³. As a solution to this dilemma, previous studies show that tensile stress can be used to increase the quality factor of a nanomechanical resonator for a given dimension^{43-46, 66}. High tensile stress thin films can be grown using low pressure chemical vapor deposition (LPCVD). In literature, the most widely preferred material is the LPCVD grown silicon nitride thin film with high tensile stress, ranging from hundreds of MPa to few GPa^{43-46, 66, 67, 69}. A quality factor over a million at room temperature has been reported using this material⁴⁶. In addition to high tensile stress, silicon nitride has also high Young's modulus which is demanded for high resonance frequency as given in Equation 2.12. Last but not least, high tensile stress combined with high Young's modulus makes the nanostructures mechanically stable and durable. They are more resilient against the stiction effect which is a well-known problem for the fabrication of suspended micro and nano structures¹³⁸. On account of high tensile stress, it is possible to fabricate doubly clamped beams as long as hundreds of microns without using sophisticated techniques like critical point drying⁴⁶.

Despite its numerous advantages mentioned above, the main drawback of high tensile stress is that the structures will be deformed in- and out-of-plane once they are released from the layers underneath. Depending on the geometry of the pattern, the deformation occurs in a complex way by contracting, buckling, bending and twisting the structures. In some applications, the shape deformation can be utilized for the fabrication of 3D structures like micro-turbines¹³⁹, sensors¹⁴⁰, and atomic force microscope cantilevers¹⁴¹. On the other hand, in some applications such as the fabrication of tunnel junctions, the original positions of the patterned structures must be preserved after release process. In some earlier work, different geometries are proposed and implemented to reduce the sensitivity of the suspended structures to thin film stresses^{142, 143}. However, these geometries are tested only for relatively small tensile stresses (70MPa) compared to the silicon nitride films used in contemporary NEMS. In some other studies, the intrinsic tensile stress of the nanoresonator is reduced by embedding spring-like structures on doubly-clamped beams^{144, 145}. All in all, there is a great need for a fabrication technique which incorporates the tensile stress to fabricate suspended structures with nanometer range precision. The main motivation behind developing this technique is to control the gap size between two suspended structures made of high tensile stress silicon nitride, after release.

6.3 Device Fabrication

The free standing nanogap structures studied in this thesis were fabricated from a 100 nm thick stoichiometric LPCVD grown nitride film (NOVA Electronic Materials). The nitride film has the tensile stress of 800 MPa (provided by the manufacturer) and is grown on top of a 1 μm thick thermal oxide which is used as the sacrificial layer. During this study, all the inspections and measurements were performed by SEM imaging and no electrical connections were required. Therefore, there was no need for optical lithography and all the patterns were defined by EBL only. The patterns were transferred to nitride layer by anisotropic dry etch and the underlying oxide layer is removed by wet etch to release the structures. The fabrication steps are illustrated in Figure 6.1 and the details of device fabrication methods are provided in Chapter 4. The device fabrication process flow can be summarized as:

1. The structures are patterned using bilayer EBL, 5 s O₂ plasma, metal coating (5nm Cr/30 nm Au) and lift-off in acetone. This metal pattern serves as an etch mask during the physical etching of nitride layer.
2. Nitride layer is etched vertically in a CHF₃/O₂ plasma using ICP-RIE. 3 minute O₂ plasma is performed after dry etch to remove the organic byproducts.
3. The oxide layer is etched isotropically using buffered HF to release the nitride structures.

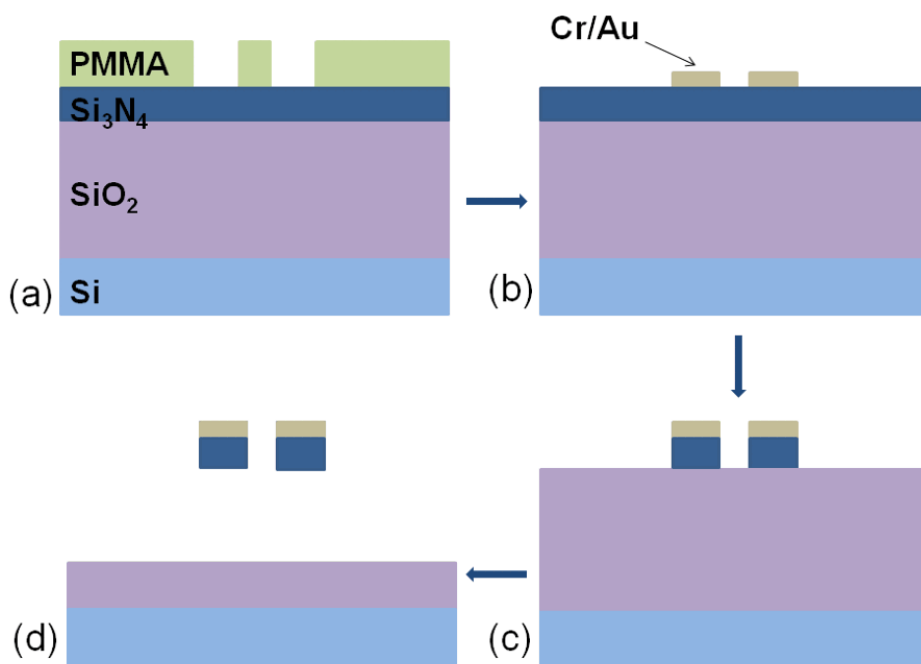


Figure 6.1: The fabrication steps of the device: (a) Bilayer PMMA covered on top of LPCVD nitride thin film, then exposed and developed, (b) a thin layer of Cr/Au coated and lifted-off, (c) the pattern is transferred to nitride layer using fluorine plasma, (d) the sacrificial oxide layer etched using buffered HF to suspend the nitride structures.

6.4 Results and Discussions

The most handicapping problem faced during nanogap fabrication was the widening of the gap between the suspended structures when they were released from the layers underneath. The EBL could define two metal tips separated by sub-10 nm gap but, the gap size increased by 50-100 nm after wet etch (Figure 4.21). As discussed previously in Chapter 4, the widening of the gap impaired the nanogap fabrication using controlled thermal evaporation, in many different ways. Therefore, this problem had to be solved to increase the yield and repeatability of the method developed for nanogap fabrication. The controlled experiments and the literature review revealed that the problem was originated from the intrinsic high tensile stress of the nitride layer. As a result, we started to work on a new technique in which the position of the suspended structures, which are made of high tensile stress thin film, can be controlled by tailoring the geometry of the structures.

The main motivation is to design a geometry which compensates for the widening of the gap. Since the geometry of the nanomechanical resonator cannot be modified, the previously fixed metal tip is now placed on a completely suspended structure which is supposed to approach the tip to the resonator after release. In the earliest model, the metal tip is placed on a free structure that has multiple grids as shown in Figure 6.2. These grids are supposed to contract and pull the metal tip towards the doubly-clamped beam. In this model, it is assumed that the only reason behind the widening of the gap is the linear contraction of the nitride layer in the active region. Hence, the length of the grids is chosen equal to the amount of the nitride layer that will be contracted in the active region (Figure 6.2). This new design has complex structures with small windows and the proximity effect ruins the lift-off even though bilayer process is employed. Therefore, a different development method using ultrasonically-assisted development in water:IPA is used instead of the conventional MIBK:IPA development¹²⁶. The SEM images in Figure 6.3 compare the results of both development methods and prove the superiority of water:IPA ultrasonic development for this particular pattern.

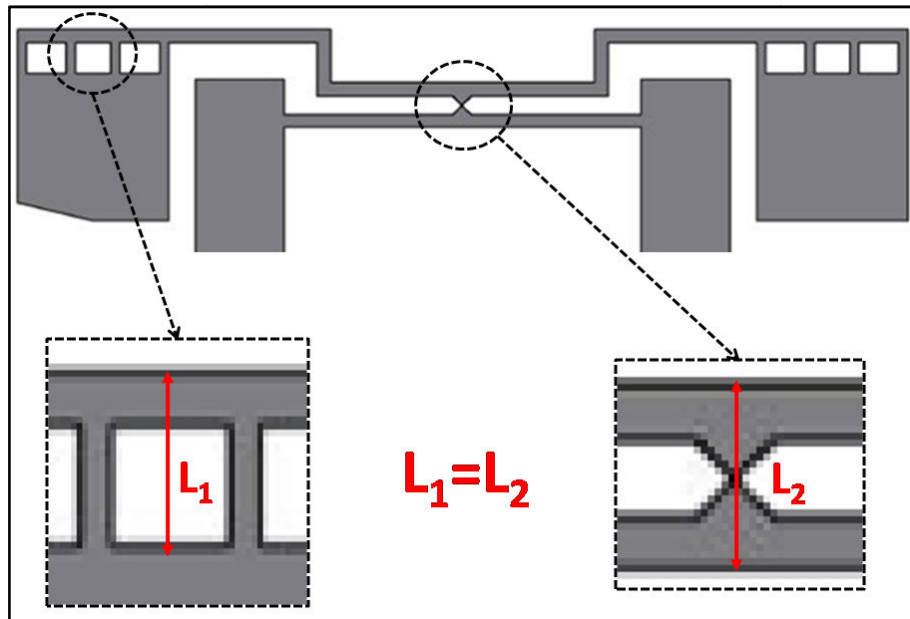


Figure 6.2: The first model developed for the compensation of gap widening and its basic operation principle are illustrated.

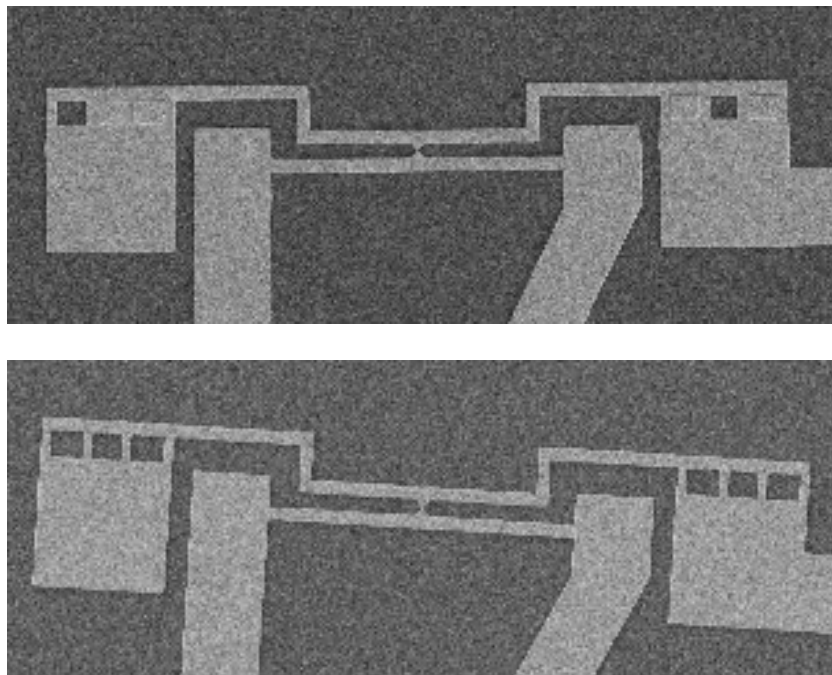


Figure 6.3: The lift-off results of bilayer EBL using MIBK:IPA (top) and ultrasonically-assisted water:IPA (bottom) development are given.

The new devices successfully fabricated using ultrasonically-assisted water:IPA development are first dry-etched vertically and then the structures are released using wet etching. The SEM images of two separate devices before dry etch and after release are given in Figure 6.4.

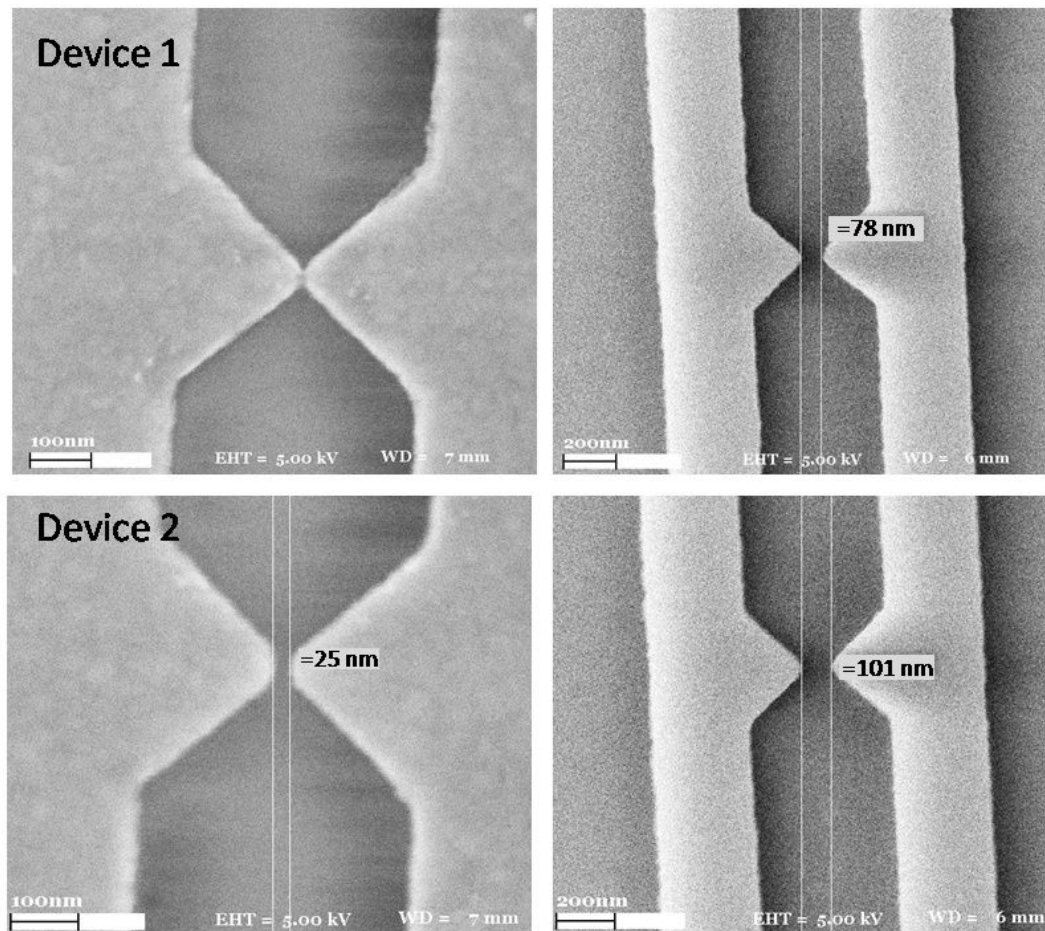


Figure 6.4: The SEM images of the gap before (left) and after (right) wet etch are given for two separate devices. The gap width increases approximately 75 nm after release for both devices.

Contrary to the expectations, the SEM images show that the gap size increases approximately 75 nm after release. Thus, this heuristic design with grids cannot correct the widening of the gap. These results suggest that there ought to be mechanisms other than the linear contraction of the nitride layer. The detailed SEM images from different viewports reveal that, in addition to the contracting, the structures undergo a complex shape deformation by buckling, bending and curling (Figure 6.5). Actually, it can be observed that the metal film on nitride layer wrinkles at points where the shape deformation is most pronounced. The deformation tends the middle of the structure to move towards its center of mass. Therefore, the metal tips move away from each other after release. The earliest model was unsuccessful since it did not take into account the complex shape deformation mechanisms other than linear contraction.

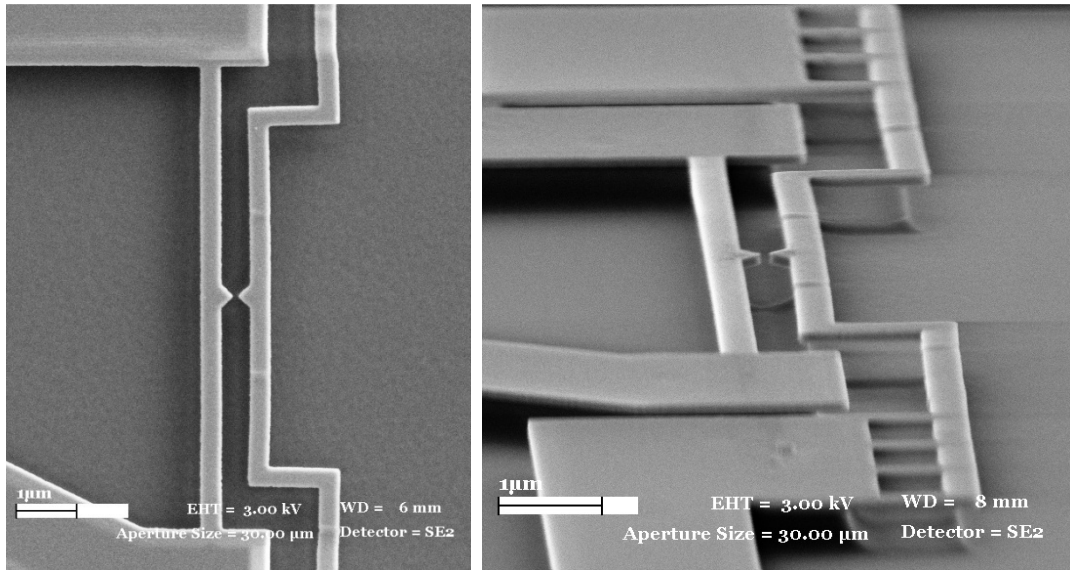


Figure 6.5: The top view (left) and side view (right) SEM images of the earliest design show that the intrinsic high tensile stress causes complex shape deformation by contracting, buckling and bending the structure.

The displacement of the nitride structures can be analyzed by static beam equations via stress-strain relations to picture the shape deformation. The structure is analyzed by numerical calculations to estimate the displacement distribution. Comsol Multiphysics 4.2 Finite Element Analysis Simulation Software is utilized to find the displacement, strain and stress distributions over the whole structure. The tensile stress is along the planar directions, $\sigma_{xx} = \sigma_{yy} = 800$ MPa and $\sigma_{zz} = 0$. Young's modulus and the Poisson's ratio of nitride is taken to be $E = 270$ MPa and $\nu = 0.23$ respectively. The thermal oxide layer is assumed to have an internal compressive stress of 350 MPa. However, the stress in the oxide layer is virtually ineffective since its bottom is completely fixed to the substrate. The simulation results giving the displacement along the gap direction are compared to the experimental results in Figure 6.6. The simulation confirms that the suspended structures contract and deform due to tensile stress and the metal tip moves apart from the doubly-clamped beam. The simulations predict that the gap widens by 55 nm after release. On the other hand, in the actual sample, the gap size is increased by 75 nm. Apart from this 20 nm discrepancy, which will be discussed later in this chapter, the simulations and the experimental findings yield parallel results. The simulation can sufficiently predict how the structure will deform after release. Therefore, new designs are first tested with simulations before the fabrication of the real devices.

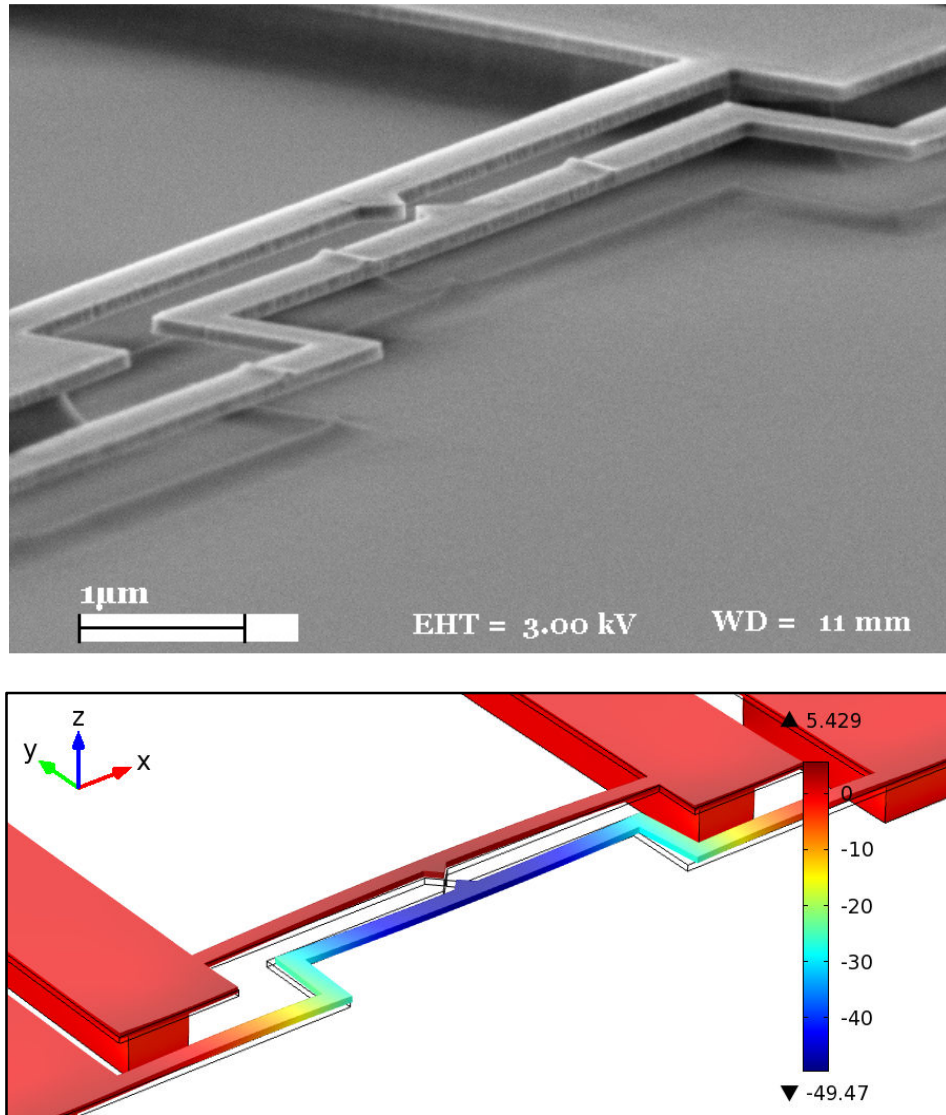


Figure 6.6: The SEM image (top) and the FEA simulation (bottom) of the uncompensated structure. The color-code represents the displacement in the y-direction in nanometers and the surface deformation is the total displacement of the material.

In the earliest design, grid model with multiple arms forms a rigid structure which cannot bend or buckle. On the other hand, only the linear contraction of multiple arms is not enough to compensate the shape deformation in the central region. The length of the multiple arms should be around 25 μm to be able to pull the metal tip to its original position. Such long arms are not feasible due to the increased device area and stiction problem. Therefore, the new models are designed with single arms in order to have a more flexible and controllable structure. In the first design, it is observed that the long, straight beam, on which the metal tip is placed, tends to curve back and pull the metal tip away from the nanobeam. In the new models, this long straight beam is replaced with three different central geometries which have shorter central beams along the x-

axis to minimize the curving back and zigzag or straight components in the y-axis to absorb the excessive stress. The simulation results of new models are shown in Figure 6.7. All the models have single arms with length, L but the central geometries are slightly different. The color code and the surface deformation represent the position change in y-direction and the total displacement of the material, respectively. In the simulation results, the calculated values for total displacement of the material are amplified ten times to be able to observe the surface deformation more evidently.

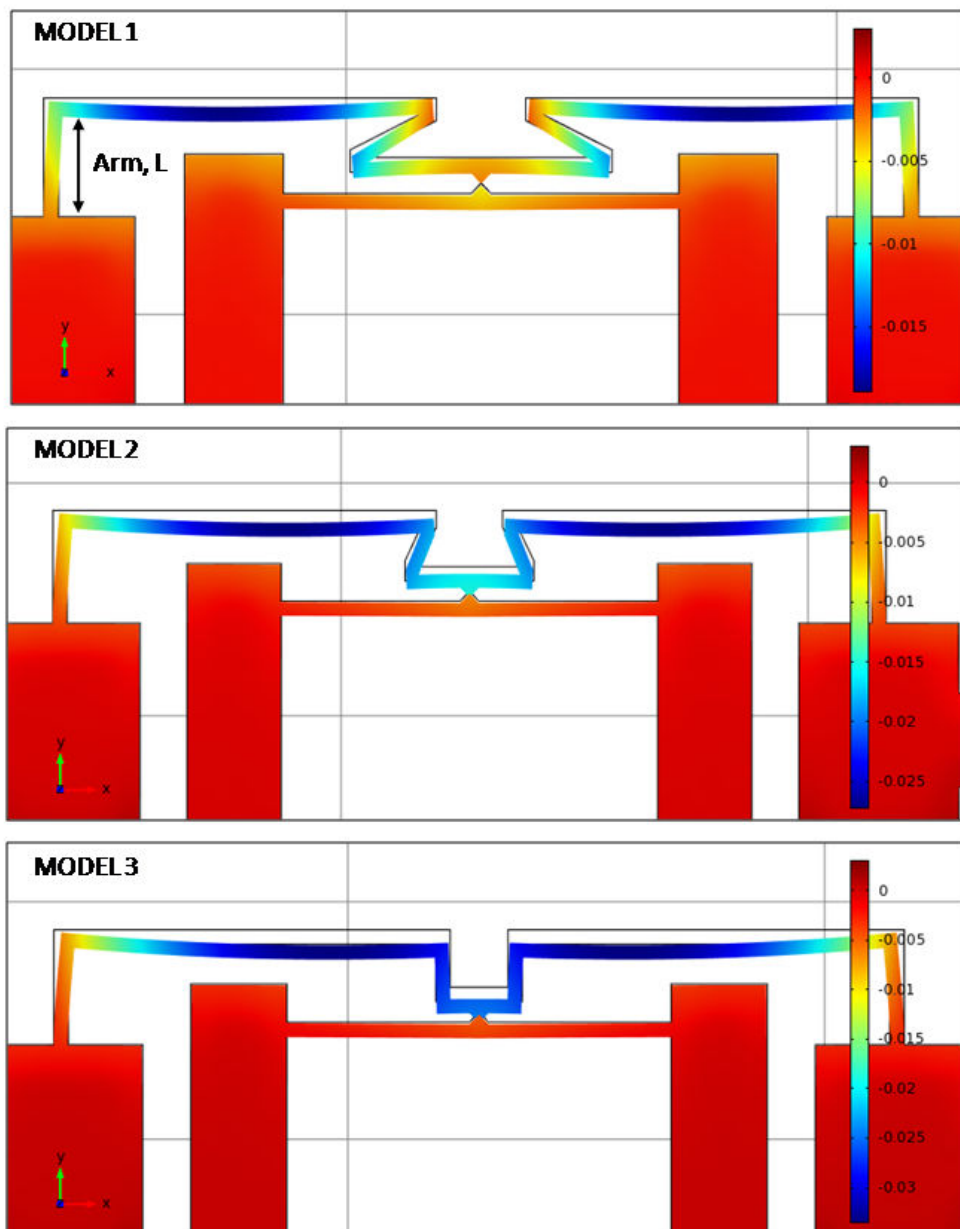


Figure 6.7: The FEA simulations of the new models are given. The color-code represents the displacement in the y-direction in μm and the surface deformation is the total displacement of the material ($\times 10$).

The simulation results show that, the widening of the gap can be compensated in all three models. Six different arm lengths between 1.7 μm and 3.0 μm are simulated for all models to investigate how the gap size changes with respect to the arm length. The calculation results show that for all models, the widening of the gap decreases as the arm length increases (Figure 6.8). According to the simulations, it is also possible to further shrink the gap size from its original value using longer arms. The change in the gap size varies from model to model for a given arm length but the general behavior resembles each other.

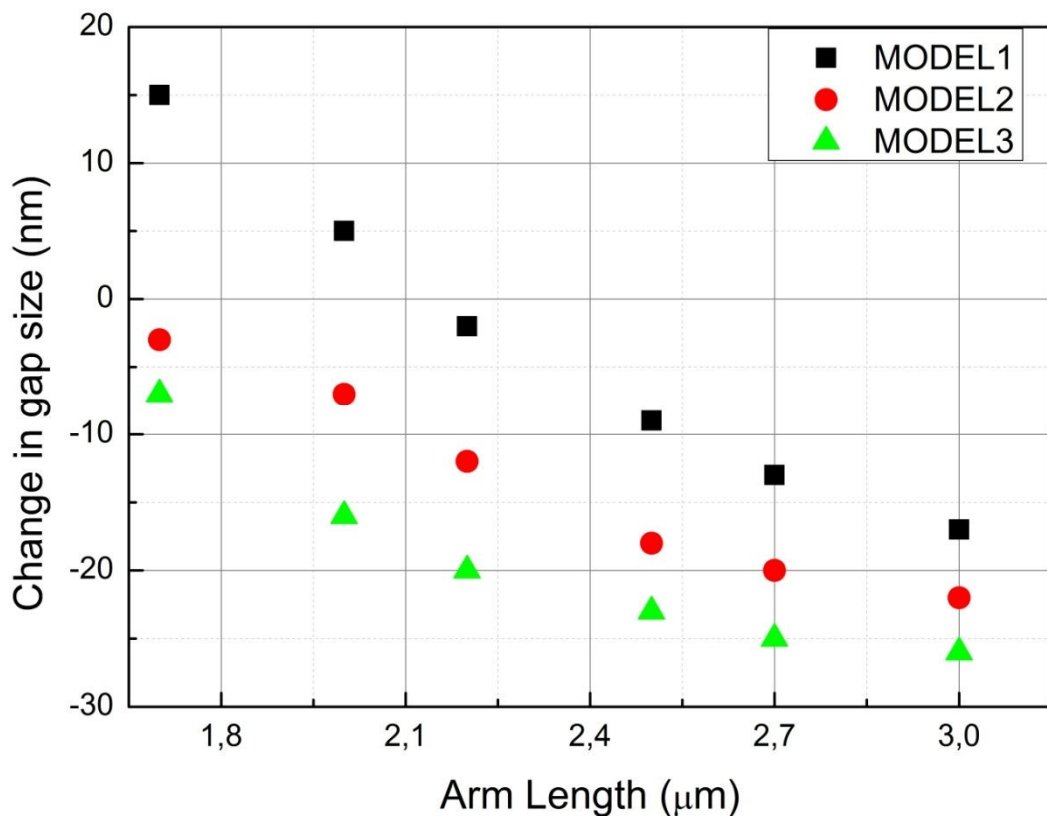


Figure 6.8: FEA results for the gap size change with respect to the length of the compensation arm for the structures shown in Figure 6.7 are given.

The designed models are fabricated using the process flow summarized in Part 6.3. Since there are no small windows in these structures, standard MIBK:IPA development is enough to develop successful lift-off results. The SEM images of fabricated devices after lift-off are shown in Figure 6.9. The arm lengths of the real devices are 100 nm shorter than the designed values. Therefore the simulations are repeated with the correct arm lengths during the comparison of the simulations and the experimental results.

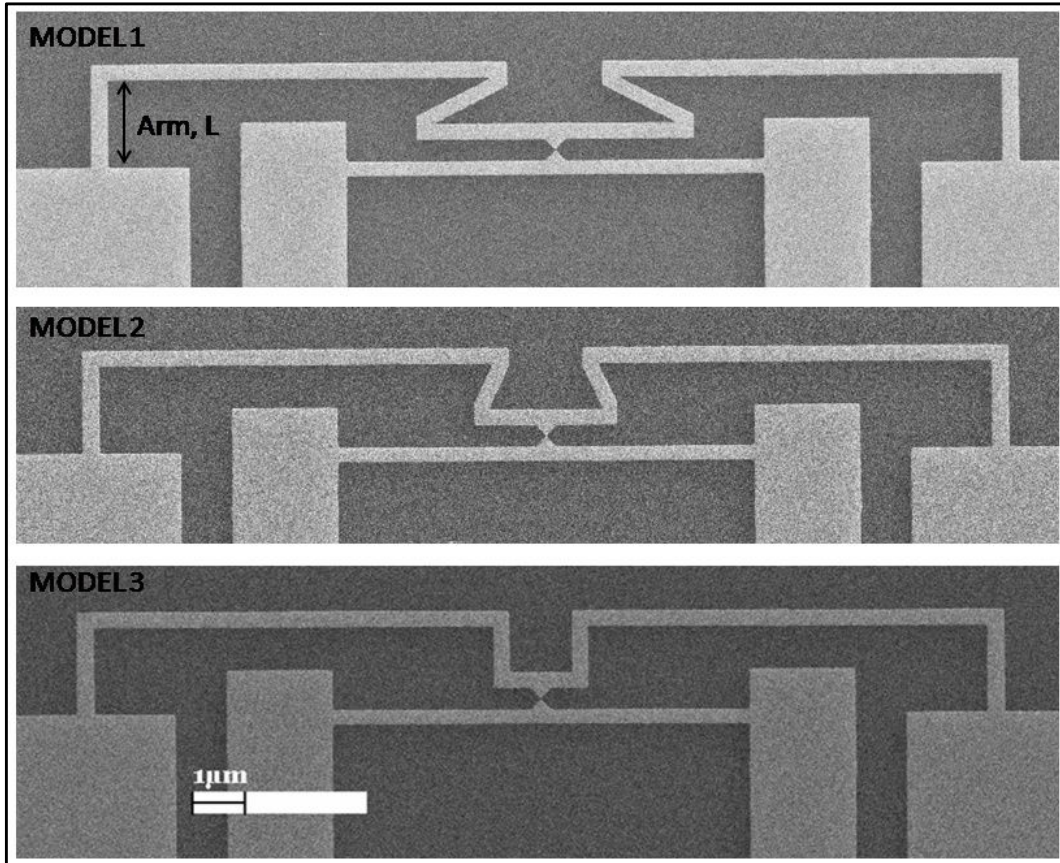


Figure 6.9: The SEM images of the fabricated three new structures are shown.

The initial gap sizes are measured after lift-off using ultra-high magnification SEM imaging. The distance between the metal tips is determined by placing the cursors to the very end of the tips. Then, the samples are etched in CHF_3/O_2 plasma using ICP-RIE. Finally, the structures are released by wet etching. The size of the gap after release is determined similarly using SEM and the difference between two measurements give the change in gap size, Δd . The metal tips that are originally in contact or the contaminated gaps are excluded since they cannot be measured correctly. Only the devices for which the initial and final gap sizes can exactly be determined are taken into account. The SEM images of one of the samples which show the initial and final gap sizes are given in Figure 6.10. The graph presents the calculated (SIM) and the real (EXP) gap width change with respect to arm length for all devices. In total, there are five, two and one data for Model 1, Model 2, and Model 3, respectively. The experimental data and the simulations agree with each other apart from an offset. As mentioned before, this offset is also present for the uncompensated structure.

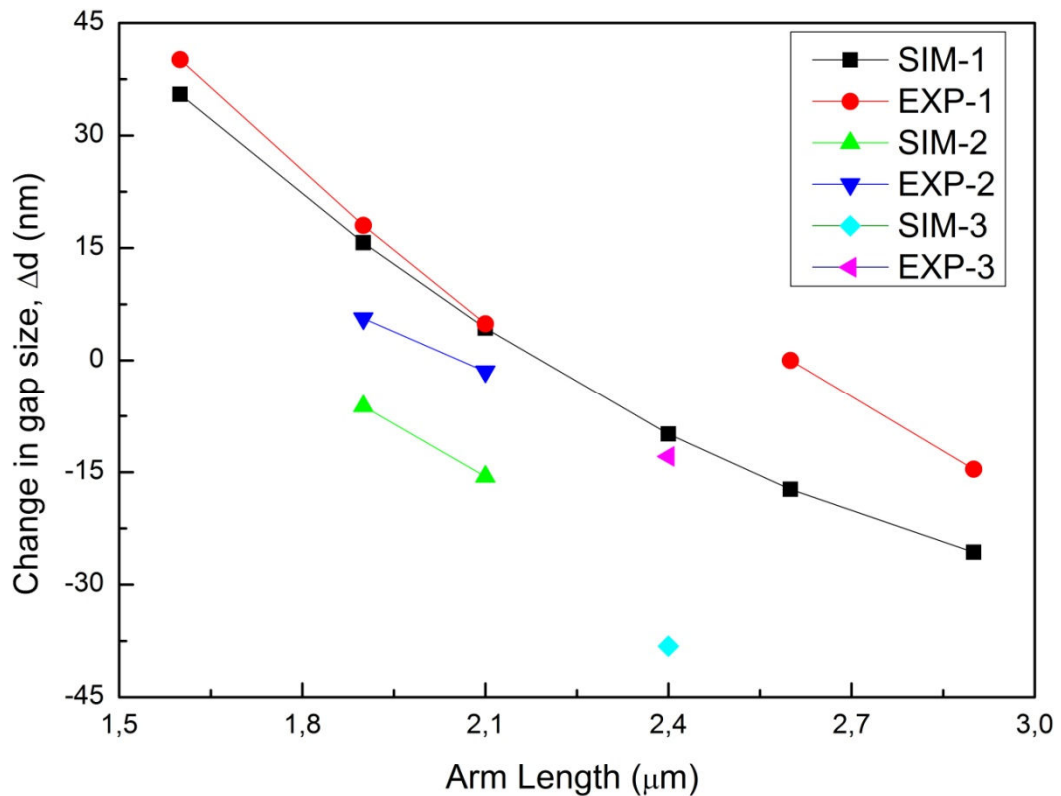
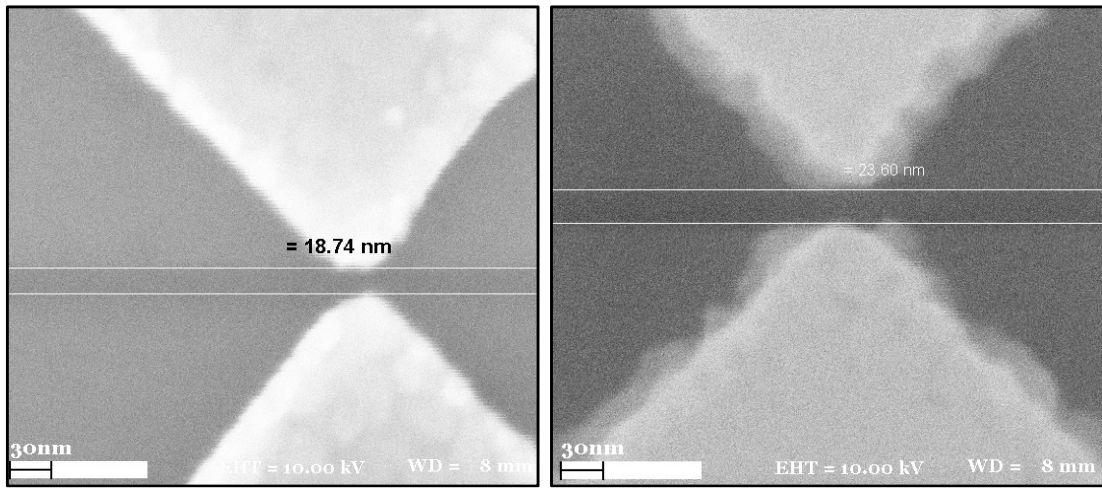


Figure 6.10: The SEM images of Model 1, $L=2.1 \mu\text{m}$ after lift-off (top-left) and after wet etch (top-right) are given. The graph compares the calculations (SIM) and the experimental data (EXP) for different models and arm lengths.

New samples are fabricated to increase the number of experimental data. Model 1 is preferred for the new samples since this structure has the highest yield in the previous experiments. Instead of measuring the initial gap width after lift-off, this time, it is measured after dry etch so that the shape distortions coming from physical etching cannot affect Δd calculations. This way, the difference between the initial and final gap width exactly reflects the shape deformation as a result of the intrinsic high tensile

stress only. The SEM images taken before and after wet etch for a device with $L = 2.9 \mu\text{m}$ are shown in Figure 6.11. The initial gap width of 79 nm remains almost the same after wet etch. The less bright shadowy pattern around the metal in before release is the oxide layer. This can be verified from the side-view image of the same gap which shows that the nitride is etched almost vertically but the oxide has a slightly positive profile. Since the oxide layer is removed after wet etch, initial gap width is measured from metal to metal.

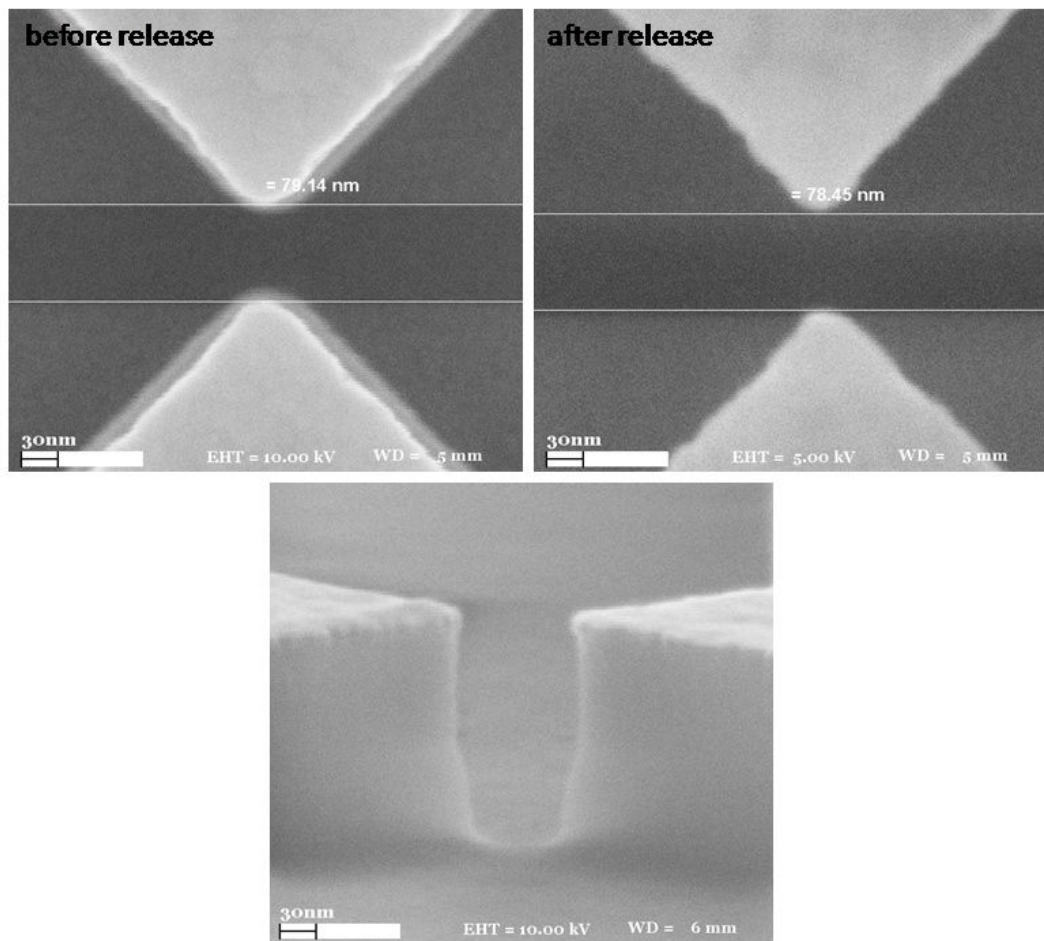


Figure 6.11: The SEM images of a device with $L = 2.9 \mu\text{m}$ before (top-left) and after (top-right) wet etch are given. The original gap width is preserved after release for this particular device. The side-view SEM image (bottom) shows that the bright shadows seen in SEM image before wet etch are oxide.

The graph in Figure 6.12 compares the experimental and simulated values of Δd for all the implemented L sizes. Overall the experimental results and the calculations are parallel to each other apart from an offset of 18 nm. The standard deviation of the experimental results from the best fit line with slope = 1 is 2.4 nm. Therefore the offset corresponds to a systematic shift in all the samples. The reasons for this shift may be due to some nonlinear effects ignored in the calculations, the compressive stress in the metal layer built due to evaporation, a systematic error in the gap measurements since before and after wet etching imaging conditions change. The contrast differences between images may lead to over or under estimation of the gap size. Possible errors in the tensile stress and Young's modulus are omitted since they would cause the best line slope to significantly deviate from 1. Apart from this offset, the experimental data agrees with the simulation and proves that with this design the final gap width can be controlled in a reasonable manner.

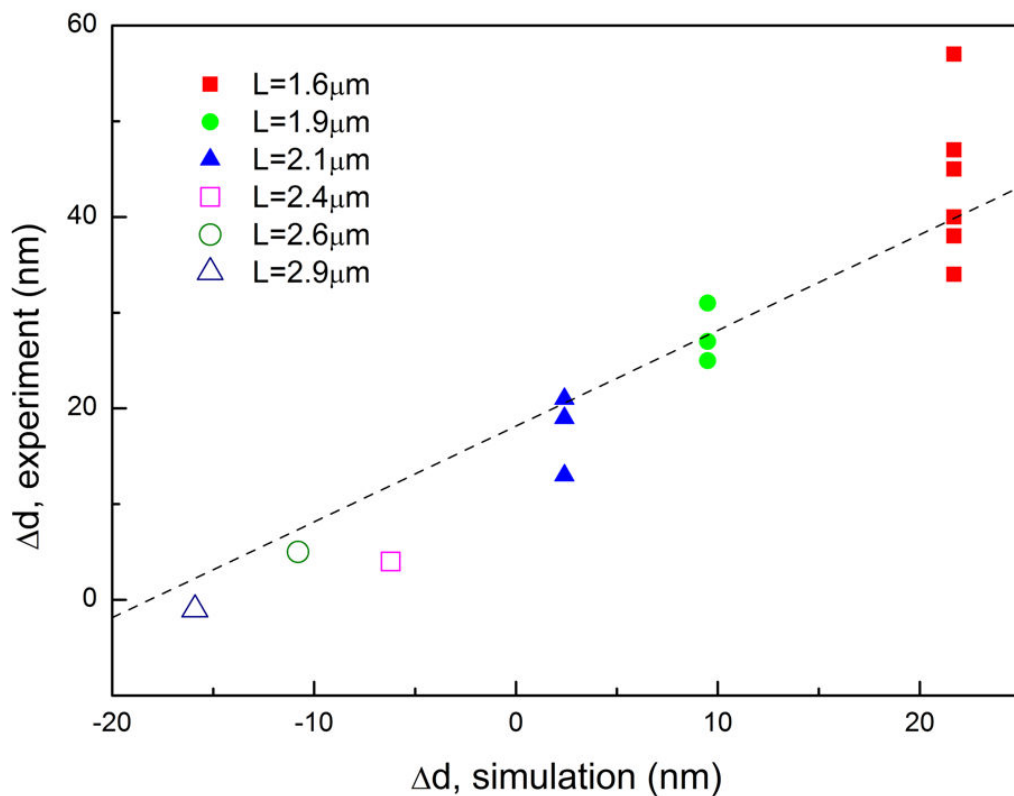


Figure 6.12: The experimental versus calculated gap width change, Δd for Model 1 is given. Symbols represent different compensation arm lengths, L . The dashed line shows the best fit with a slope of 1 with the standard error of 2.4 nm. Experimental results are -18 nm offset with respect to the simulation results.

The structure has many degrees of freedom and it is affected by various complex shape deformation mechanisms like bending, buckling and contracting. Therefore, it is not straightforward to formulate a quantitative analysis which can exactly explain the working principle of the developed model. Still, the action can be comprehended intuitively based on the fact that once the structure is released everything tends to contract. The contraction of the zigzag beam along the x direction by Δx , applies a force to the arms and bends them inwards by $\Delta x/2$. Δx increases as L increases. The displacement of the zig-zag beam can be classified into two cases depending on the magnitude of Δx :

1. Δx is large: The beam has small internal stress and small stress gradient with nearly zero deformation at the zig-zag angles, hence it acts similar to a straight beam which would displace in the $-y$ direction. Therefore the tip also displaces in the $-y$ direction (Figure 6.13(a)).
2. Δx is small: There is high internal stress left in the zig-zag beam. Due to stress its center of mass displaces towards the middle of its fixed ends. The tip moves in the $+y$ direction (Figure 6.13(c)).

For an intermediate L, the tip would not displace after release (Figure 6.13(b)). The zig-zag angle does not affect the final results significantly. As previously mentioned, wide angle (Model 2) or vertical (Model 3) elbows have been implemented successfully and the same qualitative behavior has been observed for all models.

The the gap size change, Δd with respect to the arm length, L is given in Figure 6.13 (d) for six different arm lengths using the simulation results of Model 1. By varying L from 1.6 to 2.9 μm , the Δd changes from +22 to -26 nm. This graph shows that one can tune the gap size from its lithographically defined size in any direction by changing a single fabrication parameter L.

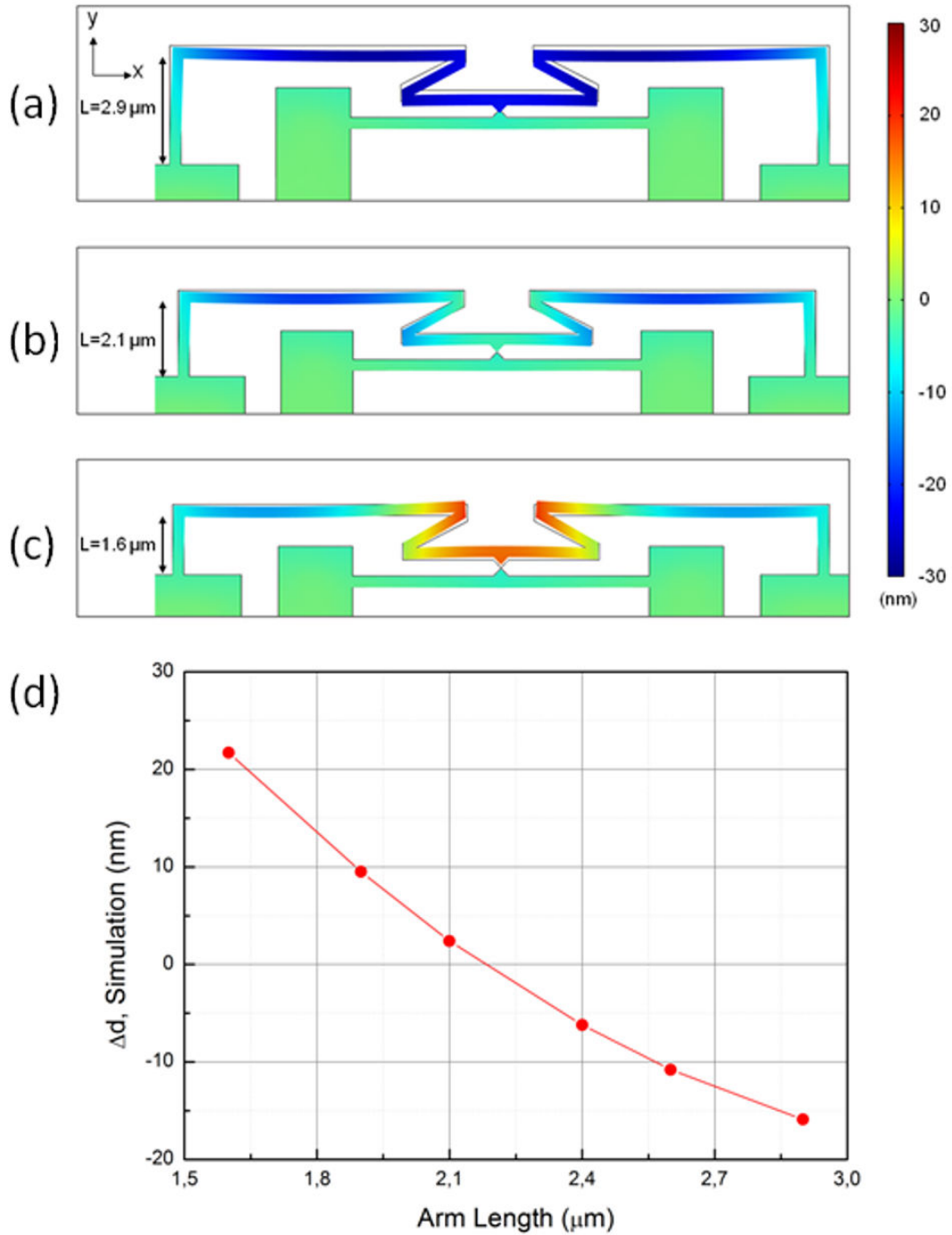


Figure 6.13: FEA results of Model 1 are given for arm lengths of a) $L = 1.6$, b) $L = 2.1$ and c) $L = 2.9 \mu\text{m}$. The color scale shows the displacement along the y-direction in nanometers. d) The graph shows the FEA results for the gap size change, Δd with respect to the arm length, L for the same structure.

6.5 Conclusion

The built-in stress in thin films leads to serious shape deformations in suspended structures once they are released from the layers underneath. The relative positions of two suspended structures can change significantly as a result of these shape deformations. For instance, the lithographically defined distance between two metal tips placed on two different suspended beams increases dramatically after release. In this work, we managed to develop a geometry that employs the built-in stress in a counteracting way to compensate for the unintentional widening of the gap. The new design can control the gap width between two suspended structures which would otherwise be widened due to the high tensile stress of the thin film. The method provides tuning of the gap between two beams via easily controllable single fabrication parameter, the length of the compensation arms, L . The technique is simulated by finite element analysis and experimentally implemented. The experimental results support the tuning capability with a statistical deviation of 2.4 nm. Although there is a systematic shift of 18 nm of the experimental results from the simulations is not completely resolved, the overall tuning capability is valid. With this technique, nanogaps beyond the lithography limits can be realized.

CHAPTER 7

CONCLUSION AND FUTURE WORK

There are primarily two outcomes of this thesis: a well-controlled, high-yield fabrication method is developed for the realization of tunnel junctions/nanogaps and a new technique is proposed and implemented for the utilization of high tensile stress to control the gap width between two silicon nitride suspended structures. Three tunnel junctions have successfully been fabricated using in-situ controlled thermal evaporation. Initially wide gaps defined by EBL (20-40 nm) are shrunk down to a nanometer size by filling the gap with thermally evaporated gold atoms. The size of the gap can be predetermined and controlled within 1 Å resolution. The fabricated tunnel junctions are characterized using I-V measurements and theoretical Simmons' model. The tunnel junctions are stable and have life-time of over weeks. The main problem we faced during the fabrication of nanogaps was “the gap widening”. The lithographically defined gaps (as small as 10 nm) become ten times wider when the nitride structures are suspended as a result of the built-in high tensile stress. The experiments showed that it is not possible to fabricate nanogaps from such wide gaps using the method we developed. Eventually, we developed a new technique which can compensate the gap widening by implementing a geometry which utilizes the built-in stress of the nitride structures. The experimental results are compared with finite element analysis and a tuning capability with a statistical deviation of 2.4 nm is demonstrated. Beyond the compensation, this method can be used to obtain gap widths beyond the lithographic resolution. In addition to these two important outcomes, the nanofabrication process recipes and flows are presented in detail for each device.

The future research suggestions in the light of the outcomes of this thesis can be summarized as following:

1. The number of tunnel junctions fabricated by controlled thermal evaporation can be increased using the compensation geometry. The factors that affect the characteristics of tunnel junctions such as gap size and effective work function can be better understood with new experiments. For instance, the dependence of the effective work function on environment conditions like pressure and temperature can be tested. The fabrication can be performed using different metals to observe the role of the material chemistry on the tunnel junction characteristic. Last but not least, the origin of the fluctuations and discrete steps in the tunneling current can be investigated.
2. The developed compensation and fabrication techniques can be used for the fabrication of a tunnel junction displacement detector coupled to a nanomechanical resonator. The mechanical properties of the nanoresonator such as resonance frequency and quality factor can be measured at cryogenic temperatures using the reflectometry technique discussed in the main body. The careful measurement of noise properties and sensitivity limit of a tunnel junction displacement detector would have an important impact in both basic and applied science.

BIBLIOGRAPHY

- [1] M. Roukes. “Observing and the observed”, *Nature* **443** (2006), 154-155.
- [2] A. A. Clerk, M. H. Devoret, S. M. Girvin, F. Marquardt, and R. J. Schoelkopf. “Introduction to quantum noise, measurement, and amplification”, *Reviews of Modern Physics* **82** (2010), 1155-1208.
- [3] M. Poot and H. S. J. van der Zant. “Mechanical systems in the quantum regime”, *Physics Reports* **511** (2012), 273-335.
- [4] A. Choe. “Researchers Race to Put the Quantum Into Mechanics”, *Science* **299** (2003), 36-37.
- [5] A. A. Clerk. “Viewpoint: Seeing the “Quantum” in Quantum Zero-Point Fluctuations”, *Physics* **5** (2012), 8.
- [6] C. M. Caves, K. S. Thorne, R. W. P. Drever, V. D. Sandberg, and M. Zimmermann. “On the measurement of a weak classical force coupled to a quantum-mechanical oscillator. I. Issues of principle*”, *Reviews of Modern Physics* **52** (1980), 341-392.
- [7] V. B. Braginsky and F. Y. Khalili. “Quantum nondemolition measurements: the route from toys to tools”, *Reviews of Modern Physics* **68** (1996), 1-11.
- [8] M. B. Hastings, I. Martin, and D. Mozyrsky. “Quantum dynamics in nonequilibrium strongly correlated environments”, *Physical Review B* **68** (2003), 035101 1-5.
- [9] C. M. Caves. “Quantum limits on noise in linear amplifiers”, *Physical Review D Particles and Fields* **26** (1982), 1817-1839.
- [10] A. A. Clerk. “Quantum-limited position detection and amplification: A linear response perspective”, *Physical Review B* **70** (2004), 245306 1-9.
- [11] K. L. Ekinici. “Electromechanical Transducers at the Nanoscale: Actuation and Sensing of Motion in Nanoelectromechanical Systems (NEMS)”, *Small* **1** (2005), 786-797.
- [12] K. D. Sattler, *Handbook of Nanophysics*. Boca Raton: CRC Press, 2011.
- [13] K.L. Ekinici and M. L. Roukes. “Nanoelectromechanical systems”, *Review of Scientific Instruments* **76** (2005), 061101 1-12.
- [14] R. J. Schoelkopf, P. Wahlgren, A. A. Kozhevnikov, P. Delsing, and D. E. Prober. “The Radio-Frequency Single-Electron Transistor (RF-SET): A Fast and Ultrasensitive Electrometer”, *Science* **280** (1998), 1238-1242.

- [15] A. N. Cleland, J. S. Aldridge, D. C. Driscoll, and A. C. Gossard. “Nanomechanical displacement sensing using a quantum point contact”, *Applied Physics Letters* **81** (2002), 1699-1701.
- [16] R. G. Knobel and A. N. Cleland. “Nanometer-scale displacement sensing using a single electron transistor”, *Nature* **424** (2003), 291-293.
- [17] M. D. LaHaye, O. Buu, B. Camarota, and K. C. Schwab. “Approaching the Quantum Limit of a Nanomechanical Resonator”, *Science* **304** (2004), 74-77.
- [18] N. E. Flowers-Jacobs, D. R. Schmidt, and K.W. Lehnert. “Intrinsic Noise Properties of Atomic Point Contact Displacement Detectors”, *Physical Review Letters* **98** (2007), 096804 1-4.
- [19] J. D. Teufel, T. Donner, M. A. Castellanos-Beltran, J. W. Harlow, and K.W. Lehnert. “Nanomechanical motion measured with an imprecision below that at the standard quantum limit”, *Nature Nanotechnology* **4** (2009), 820-823.
- [20] A. D. O’Connell, M. Hofheinz, M. Ansmann, R. C. Bialczak, M. Lenander, E. Lucero, M. Neeley, D. Sank, H. Wang, M. Weides, J. Wenner, J. M. Martinis, and A. N. Cleland. “Quantum ground state and single-phonon control of a mechanical resonator”, *Nature* **464** (2010), 697-703.
- [21] A. H. Safavi-Naeini, J. Chan, J. T. Hill, T. P. M. Alegre, A. Krause, and O. Painter. “Observation of Quantum Motion of a Nanomechanical Resonator”, *Physical Review Letters* **108** (2012), 033602 1-5.
- [22] G. Binnig and H. Rohrer. “Scanning Tunneling Microscopy”, *Surface Science* **126** (1983), 236-244.
- [23] M. Nixsch and G. Binnig. “Proposal for a novel gravitational-wave sensor”, *Journal of Vacuum Science and Technology A* **6** (1987), 470-471.
- [24] F. Bordoni, M. Karim, M. F. Bocko, and T. Mengxi. “Proposed room-temperature detector for gravitational radiation from galactic sources”, *Physical Review D* **42** (1990), 2952-2955.
- [25] M. F. Bocko, K. A. Stephenson, and R. H. Koch. “Vacuum Tunneling Probe: A Nonreciprocal, Reduced-Back-Action Transducer”, *Physical Review Letters* **61** (1988), 726-729.
- [26] K. A. Stephenson, M. F. Bocko, and R. H. Koch. “Reduced-noise nonreciprocal transducer based upon vacuum tunneling”, *Physical Review A* **40** (1989), 6615-6625.
- [27] M. F. Bocko. “The scanning tunneling microscope as a high-gain, low-noise displacement sensor”, *Review of Scientific Instruments* **61** (1990), 3763-3768.

- [28] B. Yurke and G. P. Kochanski. “Momentum noise in vacuum tunneling transducers”, *Physical Review B* **41** (1990), 8184-8194.
- [29] C. Presilla, R. Onofrio, and M. F. Bocko. “Uncertainty-principle noise in vacuum-tunneling transducers”, *Physical Review B* **45** (1992), 3735-3743.
- [30] R. Onofrio and C. Presilla. “Quantum Limit in Resonant Vacuum Tunneling Transducers”, *Europhysics Letters* **22** (1993), 333-339.
- [31] D. Mozyrsky and I. Martin. “Quantum-Classical Transition Induced by Electrical Measurement”, *Physical Review Letters* **89** (2002), 018301 1-4.
- [32] A. A. Clerk and S. M. Girvin. “Shot Noise of a Tunnel Junction Displacement Detector”, *Physical Review B* **70** (2004), 121303 1-4.
- [33] A. A. Clerk and A. D. Stone. “Noise and measurement efficiency of a partially coherent mesoscopic detector”, *Physical Review B* **69** (2004), 245303 1-14.
- [34] J. Wabnig, J. Rammer, and A. L. Shelankov “Noise spectrum of a tunnel junction coupled to a nanomechanical oscillator”, *Physical Review B* **75** (2007), 205319 1-13.
- [35] S. Walter and B. Trauzettel. “Momentum and position detection in nanoelectromechanical systems beyond the Born and Markov approximations”, *Physical Review B* **83** (2011), 155411 1-14.
- [36] C. B. Doiron, B. Trauzettel, and C. Bruder. “Measuring the Momentum of a Nanomechanical Oscillator through the Use of Two Tunnel Junctions”, *Physical Review Letters* **100** (2008), 027202 1-4.
- [37] S. D. Bennett and A. A. Clerk. “Full counting statistics and conditional evolution in a nanoelectromechanical system”, *Physical Review B* **78** (2008), 165328 1-6.
- [38] T. Li, W. Hu, and D. Zhu. “Nanogap Electrodes”, *Advanced Materials* **22** (2010), 286-300.
- [39] H. Park, A. K. L. Lim, A. P. Alivisatos, J. Park, and P. L. McEuen. “Fabrication of metallic electrodes with nanometer separation by electromigration”, *Applied Physics Letters* **75** (1999), 301-303.
- [40] M.A. Reed, C. Zhou, C.J. Muller, T.P. Burgin, and J.M. Tour, "Conductance of a molecular junction," *Science* **278** (1997), 252-254.
- [41] A. Günay-Demirkol and İ. İ. Kaya. “Note: Controlled fabrication of suspended metallic vacuum tunneling gaps”, *Review of Scientific Instruments* **83** (2012), 106108 1-3.

- [42] A. Günay-Demirkol and İ. İ. Kaya. “Tuning of nanogap size in high tensile stress silicon nitride thin films”, *Review of Scientific Instruments* **83** (2012), 055003 1-5.
- [43] Q. P. Unterreithmeier, T. Faust, and J. P. Kotthaus. “Damping of Nanomechanical Resonators”, *Physical Review Letters* **105** (2010), 027205 1-4.
- [44] L. Sekaric, D. W. Carr, S. Evoy, J. M. Parpia, and H. G. Craighead. “Nanomechanical resonant structures in silicon nitride: fabrication, operation and dissipation issues”, *Sensors and Actuators A* **101** (2002), 215-219.
- [45] S. S. Verbridge, J. M. Parpia, R. B. Reichenbach, L. M. Bellan, and H. G. Craighead. “High quality factor resonance at room temperature with nanostrings under high tensile stress”, *Journal of Applied Physics* **99** (2006), 124304 1-8.
- [46] S. S. Verbridge, H. G. Craighead, and J. M. Parpia. “A megahertz nanomechanical resonator with room temperature quality factor over a million”, *Applied Physics Letters* **92** (2008), 013112 1-3.
- [47] J. G. Simmons. “Generalized Formula for the Electric Tunnel Effect between Similar Electrodes Separated by a Thin Insulating Film”, *Journal of Applied Physics* **34** (1963), 1793-1803.
- [48] C. Kittel and H. Kroemer, *Thermal Physics*. 2nd ed. New York: W. H. Freeman and Company, 1980.
- [49] A. N. Cleland, *Foundations of Nanomechanics*. Berlin: Springer, 2003.
- [50] V. B. Braginsky and F. Y. Khalili, edited by K. S. Thorne, *Quantum Measurement*. Cambridge: Cambridge University Press, 1992.
- [51] X. M. H. Huang, C. A. Zorman, M. Mehregany, and M. L. Roukes. “Nanodevice Motion at Microwave Frequencies”, *Nature* **421** (2003), 496.
- [52] W. Heisenberg. “Ueber den anschaulichen Inhalt der quantentheoretischen Kinematik und Mechanik”, *Zeitschrift für Physik* **43** (1927), 172-198.
- [53] J. J. Sakurai, *Modern Quantum Mechanics*. Revised ed. New York: Addison-Wesley, 1994.
- [54] Y. T. Yang, C. Callegari, X. L. Feng, K. L. Ekinci, and M. L. Roukes. “Zeptogram-Scale Nanomechanical Mass Sensing”, *Nano Letters* **6** (2006), 583 -586
- [55] R. Knobel and A. N. Cleland. “Piezoelectric displacement sensing with a single-electron transistor”, *Applied Physics Letters* **81** (2002), 2258-2260.

- [56] L. L. Chu, Y. B. Gianchandani, and L. Que. “Measurements of Material Properties Using Differential Capacitive Strain Sensors”, *Journal of Microelectromechanical Systems* **11** (202), 489–498.
- [57] M. Li, X. Tang, and M. L. Roukes. “Ultra-sensitive NEMS-based cantilevers for sensing, scanned probe and very high-frequency applications”, *Nature Nanotechnology* **2** (2007), 114-120.
- [58] S. Dohn, O. Hansen, and A. Boisen. “Cantilever based mass sensor with hard contact readout”, *Applied Physics Letters* **88** (2006), 264104 1-3.
- [59] S. Zang, L. Lou, and C. Lee. “Piezoresistive silicon nanowire based nanoelectromechanical system cantilever air flow sensor”, *Applied Physics Letters* **100** (2012), 023111 1-3.
- [60] D. R. Koenig, E. M. Weig, and J. P. Kotthaus. “Ultrasonically driven nanomechanical single-electron shuttle”, *Nature Nanotechnology* **3** (2008), 482-485.
- [61] S. M. Carr and M. N. Wybourne. “Elastic instability of nanomechanical beams”, *Applied Physics Letters* **82** (2003), 709-711.
- [62] A. N. Cleland and M. L. Roukes. “Fabrication of high frequency nanometer scale mechanical resonators from bulk Si crystals”, *Applied Physics Letters* **69** (1996), 2653-2655.
- [63] A. N. Cleland, M. Pophristic and I. Ferguson. “Single-crystal aluminum nitride nanomechanical resonators”, *Applied Physics Letters* **79** (2001), 2070-2072.
- [64] S. M. Spearing. “Materials issues in microelectromechanical systems (MEMS)”, *Acta Materialia* **48** (2000), 179-196.
- [65] Q. P. Unterreithmeier, E. M. Weig, and J. P. Kotthaus. “Universal transduction scheme for nanomechanical systems based on dielectric forces”, *Nature* **458** (2009), 1001-1004.
- [66] S. S. Verbridge, R. Ilic, H. G. Craighead, and J. M. Parpia. “Size and frequency dependent gas damping of nanomechanical resonators”, *Applied Physics Letters* **93** (2008), 013101 1-3.
- [67] L. Sekaric, M. Zalalutdinov, R. B. Bhiladvala, A. T. Zehnder, J. M. Parpia, and H. G. Craighead. “Operation of nanomechanical resonant structures in air”, *Applied Physics Letter* **81** (2002), 2641-2643.
- [68] Y. T. Yang, K. L. Ekinci, X. M. H. Huang, L. M. Schiavone, M. L. Roukes, C. A. Zorman, and M. Mehregany. “Monocrystalline silicon carbide nanoelectromechanical systems”, *Applied Physics Letter* **78** (2001), 162-164.

- [69] L. Sekaric, J. M. Parpia, H. G. Craighead, T. Feygelson, B. H. Houston and J. E. Butler. “Nanomechanical resonant structures in nanocrystalline diamond”, *Applied Physics Letter* **81** (2002), 4455-4457.
- [70] R. B. Karabalin, M. H. Matheny, X. L. Feng, E. Defay, G. L. Rhun, C. Marcoux, S. Hentz, P. Andreucci, and M. L. Roukes. “Piezoelectric nanoelectromechanical resonators based on aluminum nitride thin films”, *Applied Physics Letter* **95** (2009), 103111 1-3.
- [71] Y. A. Pashkin, T. F. Li, J. P. Pekola, O. Astafiev, D. A. Knyazev, F. Hoehne, H. Im, Y. Nakamura, and J. S. Tsai. “Detection of mechanical resonance of a single-electron transistor by direct current”, *Applied Physics Letter* **96** (2010), 263513 1-3.
- [72] M. P. Blencowe. “Nanoelectromechanical Systems”, *Contemporary Physics* **46** (2005), 249-264.
- [73] M. H. Devoret and R. J. Schoelkopf. “Amplifying quantum signals with the single-electron transistor”, *Nature* **406** (2000), 1039-1046.
- [74] D. Karabacak, T. Kouh, and K. L. Ekinci. “Analysis of optical interferometric displacement detection in nanoelectromechanical systems”, *Journal of Applied Physics* **98** (2005), 124309 1-9.
- [75] T. Kouh, D. Karabacak, D. H. Kim, and K. L. Ekinci. “Diffraction effects in optical interferometric displacement detection in nanoelectromechanical systems”, *Applied Physics Letters* **86** (2005), 013106 1-3.
- [76] M. Belov, N. J. Quidron, S. Sharma, W. K. Hiebert, T. I. Kamins, and S. Evoy. “Mechanical resonance of clamped silicon nanowires measured by optical interferometry”, *Journal of Applied Physics* **103** (2008), 074304 1-7.
- [77] U. Kemiktarak, T. Ndukum, K. C. Schwab, and K. L. Ekinci. “Radio-frequency scanning tunnelling microscopy”, *Nature* **450** (2007), 85-89.
- [78] D. Mozyrsky, I. Martin, and M. B. Hastings. “Quantum-Limited Sensitivity of Single-Electron-Transistor-Based Displacement Detectors”, *Physical Review Letters* **92** (2004), 018303 1-4.
- [79] D. M. Karabacak, K. L. Ekinci, C. How Gan, G. J. Gbur, M. S. Unlu, S. B. Ippolito, B. B. Goldberg, and P. S. Carney. “Diffraction of evanescent waves and nanomechanical displacement detection”, *Optics Letters* **32** (2007), 1881-1883.
- [80] Y. Sun, H. Mortensen, S. Schar, A. S. Lucier, Y. Miyahara, and P. Grütter. “From tunneling to point contact: Correlation between forces and current”, *Physical Review B* **71** (2005), 193407 1-4.
- [81] R. Eisberg and R. Resnick. *Quantum Physics of Atoms, Molecules, Solids, Nuclei, and Particles*. 2nd ed., New York : Wiley, 1985.

- [82] R. A. Serway, C. J. Moses, and C. A. Moyer. *Modern Physics*. 3rd ed., Belmont : Thomson, 2005.
- [83] J.V. Lauritsen, and F. Besenbacher. “Model Catalyst Surfaces Investigated by Scanning Tunneling Microscopy”, *Advances in Catalysis* **50** (2006), 97-147.
- [84] H. Park, J. Park, A. K. L. Lim, E. H. Anderson, A. P. Alivisatos, and P. L. McEuen. “Nanomechanical oscillations in a single-C60 transistor”, *Nature* **407** (2000), 57-60.
- [85] L. F. Sun, S. N. Chin, E. Marx, K. S. Curtis, N. C. Greenham, and C. J. B. Ford. “Shadow-evaporated nanometre-sized gaps and their use in electrical studies of nanocrystals”, *Nanotechnology* **16** (2005), 631-634.
- [86] M. Tsutsui, M. Taniguchi, K. Yokota, and T. Kawai. “Identifying single nucleotides by tunnelling current”, *Nature Nanotechnology* **5** (2010), 286-290.
- [87] S. M. Iqbal, G. Balasundarama, S. Ghosh, D. E. Bergstromb, and R. Bashirc. “Direct current electrical characterization of ds-DNA in nanogap junctions”, *Applied Physics Letters* **86** (2005), 153901 1-3.
- [88] M. A. Reed, J. Chen, A. M. Rawlett, D. W. Price, and J. M. Tour. “Molecular random access memory cell”, *Applied Physics Letters* **78** (2001), 3735-3737.
- [89] M. Elbing, R. Ochs, M. Koentopp, M. Fischer, C. von Hanisch, F. Weigend, F. Evers, H. B. Weber, and M. Mayor. “A single-molecule diode”, *PNAS* **102** (2005), 815-8820.
- [90] S. Kubatkin, A. Danilov, M. Hjort, J. Cornil, J. L. Bredas, N. Stuhr-Hansen, P. Hedegard, and T. Bjornholm. “Single-electron transistor of a single organic molecule with access to several redox states”, *Nature* **425** (2003), 698-701.
- [91] H. B. Heersche, G. Lientschnig, K. O’Neill, H. S. J. van der Zant, and H. W. Zandbergen. “In situ imaging of electromigration-induced nanogap formation by transmission electron microscopy”, *Applied Physics Letters* **91** (2007), 072107 1-3.
- [92] C. Xiang, J. Y. Kim, and R. M. Penner. “Reconnectable Sub-5 nm Nanogaps in Ultralong Gold Nanowires”, *Nano Letters* **9** (2009), 2133-2138.
- [93] A. Umeno and K. Hirakawa. “Spectroscopic analysis of electromigration at gold nanojunctions”, *Physica E* **42** (2010), 2826-2829.,

- [94] H. Suga, M. Horikawa, S. Odaka, H. Miyazaki, K. Tsukagoshi, T. Shimizu, and Y. Naitoh. "Influence of electrode size on resistance switching effect in nanogap junctions", *Applied Physics Letters* **97** (2010), 073118 1-3.
- [95] G. Esen and M. S. Fuhrer. "Temperature control of electromigration to form gold nanogap junctions", *Applied Physics Letters* **87** (2005), 263101 1-3.
- [96] Z. M. Wu, M. Steinacher, R. Huber, M. Calame, S. J. van der Molen, and C. Schönenberger. "Feedback controlled electromigration in four-terminal nanojunctions", *Applied Physics Letters* **91** (2007), 053118 1-3.
- [97] D. R. Strachan, D. E. Smith, D. E. Johnston, T.-H. Park, M. J. Therien, D. A. Bonnell, and A. T. Johnson. "Controlled fabrication of nanogaps in ambient environment for molecular electronics", *Applied Physics Letters* **86** (2005), 043109 1-3.
- [98] D. R. Strachan, D. E. Smith, M. D. Fischbein, D. E. Johnston, B. S. Guiton, M. Drndic, D. A. Bonnell, and A. T. Johnson. "Clean Electromigrated Nanogaps Imaged by Transmission Electron Microscopy", *Nano Letters* **6** (2006), 441-444.
- [99] S. Girod, J. L. Bubendorff, F. Montaigne, L. Simon, D. Lacour and M. Hehn. "Real time atomic force microscopy imaging during nanogap formation by electromigration", *Nanotechnology* **23** (2012), 365302 1-4.
- [100] J. M. van Ruitenbeek, A. Alvarez, I. Pineyro, C. Grahmann, P. Joyez, M. H. Devoret, D. Esteve, and C. Urbina. "Adjustable nanofabricated atomic size contacts", *Review of Scientific Instruments* **67** (1996), 108-111.
- [101] M. Tsutsui, T. Ohshiro, K. Matsubara, M. Furuhashi, M. Taniguchi, and T. Kawai. "Atomically controlled fabrications of subnanometer scale electrode gaps", *Journal of Applied Physics* **108** (2010), 064312 1-4.
- [102] J. Tian, Y. Yang, B. Liu, B. Schollhorn, D. Wu, E. Maisonhaute, A. S. Muns, Y. Chen, C. Amatore, N. Tao, and Z. Tian. "The fabrication and characterization of adjustable nanogaps between gold electrodes on chip for electrical measurement of single molecules", *Nanotechnology* **21** (2010), 274012 1-6.
- [103] M. Tsutsui, M. Taniguchi, and T. Kawai. "Fabrication of 0.5 nm electrode gaps using self-breaking technique", *Applied Physics Letters* **93** (2008), 163115 1-3.
- [104] I. Diez-Perez, J. Hihath, Y. Lee, L. Yu, L. Adamska, M. A. Kozhushner, I. I. Oleynik, and N. Tao. "Rectification and stability of a single molecular diode with controlled orientation", *Nature Chemistry* **1** (2009), 635-641.

- [105] A. Ilyas, W. Asghar, P. B. Allen, H. Duhon, A. D. Ellington, and S. M. Iqbal. “Electrical detection of cancer biomarker using aptamers with nanogap break-junctions”, *Nanotechnology* **23** (2012), 275502 1-8.
- [106] A. R. Champagne, A. N. Pasupathy, and D. C. Ralph. “Mechanically Adjustable and Electrically Gated Single-Molecule Transistors”, *Nano Letters* **5** (2005), 305-308.
- [107] A. F. Morpurgo, C. M. Marcusa, and D. B. Robinson. “Controlled fabrication of metallic electrodes with atomic separation”, *Applied Physics Letters* **74** (1999), 2084-2086.
- [108] M. R. Calvo, A. I. Mares, V. Climent, J. M. van Ruitenbeek, and C. Untiedt. “Formation of atomic-sized contacts controlled by electrochemical methods”, *Physica Status Solidi* **204** (2007), 1677-1685.
- [109] C. Z. Li, H. X. He, and N. J. Tao. “Quantized tunneling current in the metallic nanogaps formed by electrodeposition and etching”, *Applied Physics Letters* **77** (2000), 3995-3997.
- [110] X. L. Li, S. Z. Hua, H. D. Chopra, and N. J. Tao. “Formation of atomic point contacts and molecular junctions with a combined mechanical break junction and electrodeposition method”, *Micro & Nano Letters* **1** (2006), 83-88.
- [111] Y. V. Kervennic, H. S. J. Van der Zant, A. F. Morpurgo, L. Gurevich, and L. P. Kouwenhoven. “Nanometer-spaced electrodes with calibrated separation”, *Applied Physics Letters* **80** (2002), 321-323.
- [112] A. Bezryadin and C. Dekker. “Nanofabrication of electrodes with sub-5 nm spacing for transport experiments on single molecules and metal clusters”, *Journal of Vacuum Science and Technology B* **15** (1997), 793-799.
- [113] L. D. L. S. Valladares, L. L. Felix, A. B. Dominguez, T. Mitrelias, F. Sfigakis, S. I. Khondaker, C. H. W. Barnes, and Y. Majima. “Controlled electroplating and electromigration in nickel electrodes for nanogap formation”, *Nanotechnology* **21** (2010), 445304 1-8.
- [114] Y. Kashimura, H. Nakashima, K. Furukawa, and K. Torimitsu. “Fabrication of nano-gap electrodes using electroplating technique”, *Thin Solid Films* **438-439** (2003), 317-321.
- [115] T. Nagase, K. Gamo, T. Kubota, and S. Mashiko. “Direct fabrication of nano-gap electrodes by focused ion beam etching”, *Thin Solid Films* **499** (2006), 279-284.

- [116] K. Shigeto, M. Kawamura, A.Y. Kasumov, K. Tsukagoshi, K. Kono, Y. Aoyagi. “Reproducible formation of nanoscale-gap electrodes for single-molecule measurements by combination of FIB deposition and tunneling current detection”, *Microelectronic Engineering* **83** (2006), 1471-1473.
- [117] M. D. Fischbein and M. Drndic. “Nanogaps by direct lithography for high-resolution imaging and electronic characterization of nanostructures”, *Applied Physics Letters* **88** (2006), 063116 1-3.
- [118] R. Gupta and B. G. Willis. “Nanometer spaced electrodes using selective area atomic layer deposition”, *Applied Physics Letters* **90** (2007), 253102 1-3.
- [119] R. Gupta and B. G. Willis. “Parallel fabrication of monolithic nanoscopic tunnel junctions for molecular devices”, *Journal of Vacuum Science and Technology B* **28** (2010) 538-544.
- [120] P. Steinmann and J. M. R. Weaver. “Fabrication of sub-5 nm gaps between metallic electrodes using conventional lithographic techniques”, *Journal of Vacuum Science and Technology B* **22** (2004) 3178-3181.
- [121] P. S. Ho and T. Kwok. “Electromigration in metals”, *Journal Reports on Progress in Physics* **52** (1989) 301-348.
- [122] J. Moreland and J. W. Ekin. “Electron tunneling experiments using Nb-Sn “break” junctions”, *Journal of Applied Physics* **58** (1985) 3888-3895.
- [123] M. F. Bocko and R. Onofrio. “On the measurement of a weak classical force coupled to a harmonic oscillator: experimental progress”, *Reviews of Modern Physics* **68** (1996) 755-799.
- [124] N. F. Schwabe, A. N. Cleland, M. C. Cross and M. L. Roukes. “Perturbation of tunneling processes by mechanical degrees of freedom in mesoscopic junctions”, *Physical Review B* **52** (1995) 12911-12920.
- [125] B. Cord, J. Lutkenhaus, and K. K. Berggren. “Optimal temperature for development of poly(methylmethacrylate)”, *Journal of Vacuum Science and Technology B* **25** (2007) 2013-2016.
- [126] S. Yasin, D. G. Hasko, and H. Ahmed. “Fabrication of <5 nm width lines in poly(methylmethacrylate) resist using a water:isopropyl alcohol developer and ultrasonically-assisted development”, *Applied Physics Letters* **78** (2001) 2760-2762.
- [127] A. Olzierski and I. Raptis. “Development and molecular-weight issues on the lithographic performance of poly (methyl methacrylate)”, *Microelectronic Engineering* **73-74** (2004) 244-251.

- [128] S. Yasin, M. N. Khalid, and D. G. Hasko. “Reduction in Roughness of Resist Features in PMMA due to the Absence of a Rinse”, *Japanese Journal of Applied Physics* **43** (2004) 6984-6987.
- [129] D. S. Macintyre, O. Ignatova, S. Thoms, and I. G. Thayne. “Resist residues and transistor gate fabrication”, *Journal of Vacuum Science and Technology B* **27** (2009) 2597-2601.
- [130] N. Possemea, T. Chevolleau, R. Bouyssou, T. David, V. Arnal, J. P. Barnes, C. Verove, and O. Joubert. “Residue growth on metallic-hard mask after dielectric etching in fluorocarbon-based plasmas. I. Mechanisms”, *Journal of Vacuum Science and Technology B* **28** (2010) 809-816.
- [131] N. Possemea, R. Bouyssou, T. Chevolleau, T. David, V. Arnal, M. Damon, P. Brun, C. Verove, and O. Joubert. “Residue growth on metallic hard mask after dielectric etching in fluorocarbon based plasmas. II. Solutions”, *Journal of Vacuum Science and Technology B* **29** (2011) 011018 1-10.
- [132] P. Steinmann and J. M. R. Weaver. “Nanometer-scale gaps between metallic electrodes fabricated using a statistical alignment technique”, *Applied Physics Letters* **86** (2005) 063104 1-3.
- [133] J. R. Hahn, Y. A. Hong, and H. Kang. “Electron tunneling across an interfacial water layer inside an STM junction: tunneling distance, barrier height and water polarization effect”, *Applied Physics A Materials Science and Processing* **66** (1998) 467-472.
- [134] C. W. Miller, Z. Li, J. Akerman, and I. K. Schuller. “Impact of interfacial roughness on tunneling conductance and extracted barrier parameters”, *Applied Physics Letters* **90** (2007) 043513 1-3.
- [135] C. W. Miller and D. D. Belyea. “The impact of barrier height distributions in tunnel junctions”, *Journal of Applied Physics* **105** (2009) 094505 1-5.
- [136] W. Haiss, S. Martin, E. Leary, H. van Zalinge, S. J. Higgins, L. Bouffier, and R. J. Nichols. “Impact of Junction Formation Method and Surface Roughness on Single Molecule Conductance”, *Journal of Physical Chemistry C* **113** (2009) 5823-5833.
- [137] A. Mangin, A. Anthore, M. L. D. Rocca, E. Boulat, and P. Lafarge. “Reduced work functions in gold electromigrated nanogaps”, *Physical Review B* **80** (2009) 235432 1-5.
- [138] N. Tas, T. Sonnenberg, H. Jansen, R. Legtenberg, and M. Elwenspoek, “Stiction in surface micromachining”, *Journal of Micromechanics and Microengineering* **6** (1996) 385-397.

- [139] C. L. Tsai and A. K. Henning, "Surface Micromachined Turbines", Proceedings of the 9th International Conference on Solid State Sensors and Actuators, Chicago, Illinois, 1997, IEEE (Piscataway, NJ, 1997), pp. 829–832.
- [140] F. Iker, N. Andre, T. Pardoen, and J. P. Raskin. "Three-Dimensional Self-Assembled Sensors in Thin-Film SOI Technology", *Journal of Microelectromechanical Systems* **15** (2006) 1687-1697.
- [141] Y. Sarov, T. Ivanov, A. Frank, and I.W. Rangelow. "Controllable off-plane deflection of cantilevers for multiple scanning proximity probe arrays", *Applied Physics A* **92** (2008) 525-530.
- [142] D. F. Moore, M. I. lutwyche, and A. C. F. Hoole. "Fabrication of freestanding structures and proposed applications in tunneling sensors", *Journal of Vacuum Science and Technology B* **11** (1993) 2548-2551.
- [143] M. I. lutwyche, D. F. Moore. "Suspended structures made by electron beam lithography", *Journal of Micromechanics and Microengineering* **1** (1991) 237-246.
- [144] G. Klaasse, R. Puers, and H. A. C. Tilmans. "Stress release structures for actuator beams with a stress gradient", *Journal of Micromechanics and Microengineering* **17** (2007) 2093-2101.
- [145] D. Haronian and N. C. MacDonald. "Spring suspended corrugated membranes", *Journal of Micromechanics and Microengineering* **5** (1995) 289-296.